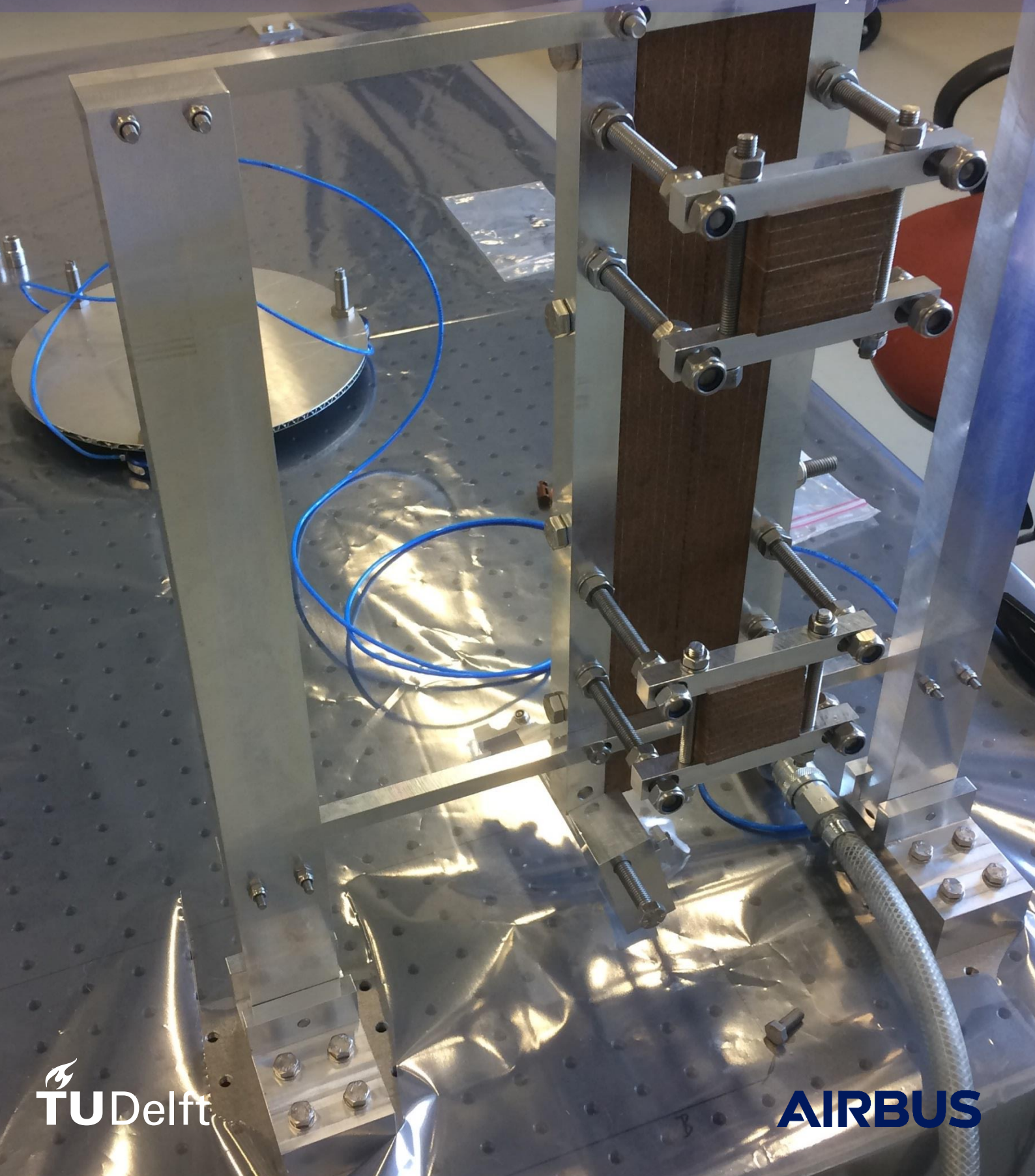


INFRA (Inflatable Radiator)

The development of an actively controllable, inflatable and deployable HiPeR radiator breadboard model

Boudewijn Schwieters



INFRA (Inflatable Radiator)

The development of an actively controllable, inflatable and deployable
HiPeR radiator breadboard model

by

Boudewijn Schwieters

In partial fulfillment of the requirements for the degree of

Master of Science
in Aerospace Engineering

at Delft University of Technology,
to be defended publicly on March 21, 2018

Thesis committee:	Ir. B.T.C. Zandbergen	TU Delft
	Dr. ir. W. van der Wal	TU Delft
<i>Supervisor</i>	Dr. ir. J.M. Kuiper	TU Delft
<i>Supervisor</i>	Ir. A.S. Maas	Airbus

The contents of this report are provided "in confidence" and are to be considered proprietary information to Airbus DS NL. Data and/or information included herein shall only be used for the assessment of this report/document. Disclosure to third parties of this report/document or any part thereof, or the use of any information contained therein for purposes other than provided for by this report/document, is not permitted, unless otherwise agreed with Airbus DS NL in writing.

This thesis is confidential and cannot be made public before March 21, 2021

Preface

This thesis is produced as part of an assignment by Airbus and regards the development of inflatable radiator technology. The radiator which is designed, manufactured and tested as part of an actively heated and pressurized single-phase fluid loop radiator system, demonstrates a favorable heat performance to mass ratio and is deployed and operated in a lab environment successfully. Micrometeorites are however identified as a major concern for the lifetime of the product. A design iteration is therefore required to mitigate these risks. Hopefully the work will not only support the establishment of INFRA as part of the Airbus HiPeR suite but will it also contribute to the development of the European space inflatables market in general.

I would like to take this chance to thank the people who have been of great help during the time of my graduation. First of all, I would like to thank Alexander Maas for his supervision throughout the project, which included many fruitful discussions, but who also helped me greatly with operating efficiently and thought me how to think like an engineer. Furthermore, I would like to say thanks to my office mates Niels van der Pas and David Orgaz Diaz for the good time and for their continued thermal support and dedication to brainstorm sessions. At Airbus in Leiden, many other people were very helpful during the procurement, manufacturing, testing and assembly of the breadboard model. I have received full support from all corners of the company which I found very striking and therefore I would also like to dedicate this thesis to all those people who could always make time for me. Outside of Airbus, I would like to thank the people from the NLR for being available for discussions and for being very pleasant to work with.

Finally, I would like to dedicate this thesis to my sweet girlfriend who has provided unlimited support during the incredibly busy and demanding times and last but not least to my mom, who has always pushed me and believed in me. High five mom!

Boudewijn Schwieters

Delft, March 2018

Abstract

This thesis describes the entire process from the definition of customer requirements to the verification and validation of requirements concerning a breadboard model of an Inflatable Radiator (INFRA). INFRA is designed to provide high thermal performance to mass ratio radiator to accommodate increasing payload heat dissipation demands of future Communication satellites. The goal of the project is to deliver proof of concept of an innovative radiator technology which is based on High Performance Radiator (HiPeR) and Micro Mechanical Pumped Loop (μ MPL) heritage. INFRA radiator system (RS) is developed in a collaboration project between by Airbus and the Dutch Aerospace Center (NLR), of which the Pump Assembly (PA) subsystem is developed by the NLR and the Foil Radiator Assembly (FRA) subsystem is developed by Airbus. The development of the FRA is covered in this report.

The topics which are covered in this report are first the literature review which is performed to provide a knowledge base concerning the radiator systems and its physical/mathematical handles. Part of these theories deal with thermal and structural equations but also breadboard tests and environmental hazards are considered.

Followed by the theory are the conceptual design and the system requirements, which focusses on the early development of the system and its characteristics, but also on the technical requirements as these represent the backbone of the technical design. These requirements represent feasible specifications to be able to achieve the system characteristics, which are developed from the wishes of the customers (which are Airbus and NLR).

Other important aspects of the system are the interface between the PA and the FR, but also the flow rate and the pressure of the operating fluid. The flow rate is chosen to be 1 l/min and the absolute pressure is set to be 2 bar . Dimensioning of the tubing is found to be most important to satisfy the requirements based on these aspects, as they also provide the stiffness of the FR. Therefore, a minimum radius of 3 mm is found for the tubing, such that the FR does not deflect further than allowed during operation. The tubing should also be flexible and thin walled to be able to inflate during deployment. Since there are several possibilities available such as using adhesive or welding the tube, these options are considered however are found to be unreliable for the application. Therefore, a closed wall tube is identified which has the most relevant material properties. Since the number of materials are very limited to use for the application due to degradation of the material strength as a result of radiation, but also due to the high temperatures which are tested and the pressures which are expected, it eventually is decided to use Polyimide for the tubing.

The foil is based on the developments of the HiPeR suite. The spacing of the tubing is based on a single loop as well as the maximum manufacturable FR width, the layout together with the thickness of the foil are capable of providing a sufficiently high radiator efficiency as the material is highly capable of transporting the heat in plane while maintaining its flexibility. The tubing is also equipped with connectors which are placed between the tubing at the corners of the loop as well as at the ends of the tubes where the interfaces with the PA are located.

For the deployment of the FR in space and during the laboratory test, a Hold Down and Release Mechanism (HDRM) is designed which is mounted on the Foil Radiator Fixation (FRF). The HDRM holds down the Foil Radiator Roll Support (FRRS) which is used to roll-up the FR before launch and deploy afterwards. The FRRS is 3D-printed using an Aluminum/Titanium alloy to save time and budget while providing the required mechanical properties. The HDRM also houses a pre-tensioning disk, a lever and a redundant COTS resistor as thermal knife to cut the Dyneema thread that connects the mentioned parts. By rotation of the disk the thread can be pre-tensioned to form a firm grip that cannot be overtaken by the static launch load. The thermal knives are held within Vespel cylinders which are pressed against the thread, that can sustain the temperature required to melt the thread. After cutting the thread a lever is opened by means of a torque spring and the FRRS is released after which the deployment is initiated. The FRRS holds the corner connectors in place by means of Vespel parts, which isolate the tubing thermally from the Aluminum FRRS structure.

The FRF is a clamp which compresses a stack of Norcoat Liege onto the base of the FR to transfer the deployment forces but also isolate the FR thermally during operation. The heat leakage to the structural parts is roughly 1% of the total heat transfer from the FR. The mechanical strength of the entire FR as well as metal items is calculated to be able to handle launch loads by using a first order conservative approach.

Micro Meteorites and Orbital Debris (MMOD) analysis shows that the system has a life expectancy of less than one year in GEO and can therefore not endure the environmental aspects as required for equipping a Communications satellite. The radiation survivability however is sufficient to sustain 15 years in orbit.

The deployment is predicted by means of first order calculations and breadboard tests. The deployment behavior is specified in the requirements with angular constraints and is only required to operate within the specified boundaries and it demonstrates the required performance. It would be recommendable to formulate a dynamic model using Adams to simulate this behavior in a more detailed fashion for the next step in the development of the product. Furthermore, it was chosen to create a spreadsheet thermal model of the FRA by means of ESATAN ThermXL which is also correlated with the thermal tests. The measured performance of the FR is $Q_{meas} \approx 60 \text{ W}$, however this does not seem to be correct due to temperature measurement influences, the model however predicts an output of $Q_{FR} = 97,5 \pm 7,5 \text{ W}$, which corresponds to $Q_{FR} = 250 \pm 10 \text{ W}$ in an ideal space environment.

The report concludes with a verification and a validation of the Requirements. Recommended however are to provide the design with an update since the tubing can use a different material which is more MMOD resistant. Furthermore, a design iteration could be performed considering the thermal performance of the tubing interface, taking another look at the shape of the tube such as an oval for improved convective heat transfer, or optimizing the tube spacing for higher radiator performance.

Contents

1	INTRODUCTION	1
1.1.	PROBLEM DEFINITION	1
1.2.	SCOPE	2
2	LITERATURE REVIEW	3
2.1.	RESEARCH DEFINITION	3
2.2.	INFRA	4
2.2.1.	<i>Business opportunities</i>	5
2.3.	STATE OF THE ART	6
2.4.	THERMAL THEORY	10
2.4.1.	<i>Thermal equilibrium</i>	10
2.4.2.	<i>Thermal radiation</i>	11
2.4.3.	<i>Radiative heat transfer</i>	13
2.4.4.	<i>Conductive heat transfer</i>	14
2.4.5.	<i>Convective heat transfer</i>	15
2.4.6.	<i>Natural convection</i>	17
2.4.7.	<i>Advective coupling</i>	18
2.4.8.	<i>Radiator efficiency</i>	18
2.5.	BREADBOARD TESTING	18
2.5.1.	<i>Dyneema creep test</i>	19
2.5.2.	<i>Inflatable breadboard based on a PET/PE tube</i>	20
2.5.3.	<i>Capstan equation</i>	22
2.5.4.	<i>Roll up equation</i>	23
2.5.5.	<i>Mechanical, handling and thermal testing of applicable materials</i>	23
2.6.	GEO ENVIRONMENT	24
2.6.1.	<i>MMOD</i>	24
2.6.2.	<i>Radiation</i>	25
2.7.	RESEARCH QUESTIONS ELABORATED	26
3	INFRA REQUIREMENTS	28
3.1.	STAKEHOLDER REQUIREMENTS	29
3.2.	SYSTEM REQUIREMENTS	29
3.2.1.	<i>Requirement specification</i>	31
3.3.	RESEARCH QUESTION ELABORATION AND CONCLUSION	32
4	DESIGN DESCRIPTION.....	34
4.1.	FOIL RADIATOR ASSEMBLY (FRA)	34
4.1.1.	<i>Foil Radiator (FR)</i>	35
4.1.2.	<i>FR roll support (FRRS)</i>	41
4.1.3.	<i>Foil radiator fixation (FRF)</i>	43
4.1.4.	<i>Hold Down and Release Mechanism (HDRM)</i>	43
4.1.5.	<i>Tooling</i>	45
4.2.	FR THERMAL MODEL	47
4.2.1.	<i>FR-laminate nodes</i>	47
4.2.2.	<i>FR-tubing nodes</i>	48
4.2.3.	<i>FRF nodes</i>	49
4.2.4.	<i>FRRS</i>	49
4.2.5.	<i>Simulation</i>	50
4.3.	STRUCTURAL ANALYSIS	53
4.3.1.	<i>System mass and scaling</i>	53
4.3.2.	<i>FR</i>	54
4.3.3.	<i>FRF</i>	55
4.3.4.	<i>FRRS</i>	55

4.3.5.	<i>HDRM</i>	56
4.4.	MMOD RISK ANALYSIS.....	57
4.4.1.	<i>Impact research on Kapton and energy method</i>	57
4.4.2.	<i>Ballistic limit equation</i>	59
4.4.3.	<i>Comparison with energy method</i>	60
4.4.4.	<i>Meteoroid spatial density</i>	60
4.4.5.	<i>Collision probability</i>	61
4.4.6.	<i>Conclusion</i>	63
4.5.	RESEARCH QUESTION ELABORATION AND CONCLUSION.....	64
5	TEST SETUP AND RESULTS	66
5.1.	DEPLOYMENT TEST.....	67
5.1.1.	<i>Test setup</i>	67
5.1.2.	<i>Results</i>	68
5.1.3.	<i>HDRM electrical release test</i>	69
5.2.	BENDING TEST.....	71
5.2.1.	<i>Bending deflection results</i>	71
5.2.2.	<i>Maximum deflection results</i>	72
5.3.	THERMAL BALANCE TEST.....	73
5.3.1.	<i>Test setup</i>	73
5.3.2.	<i>Test results FR</i>	74
5.3.3.	<i>Test results RS</i>	78
5.3.4.	<i>Sensitivity analysis thermal model</i>	83
5.4.	RESEARCH QUESTION ELABORATION AND CONCLUSION.....	83
6	VERIFICATION AND VALIDATION	84
6.1.	REQUIREMENTS VERIFICATION.....	84
6.2.	REQUIREMENTS VALIDATION.....	84
6.3.	RESEARCH QUESTIONS ELABORATED.....	86
7	CONCLUSION	87
8	RECOMMENDATIONS	89
	BIBLIOGRAPHY	90
	APPENDIX A: INFLATED TUBE BENDING TEST RESULTS	93
	APPENDIX B: STRAWMAN CONCEPTS	94
	APPENDIX C: DEPLOYMENT CONCEPTS	95
	APPENDIX D: DESIGN OPTIONS	96
	APPENDIX E: THERMAL MODEL NODES	97
	APPENDIX F: DRAMA RESULTS	100
	APPENDIX G: TEST PLANNING	103
	APPENDIX H: FR THERMAL TEST DATA	105
	APPENDIX I: SENSITIVITY ANALYSIS, UNCERTAINTY PARAMETERS	106

List of figures

FIGURE 1: RESEARCH FRAMEWORK	3
FIGURE 2: INFLATABLE RADIATOR CONCEPT; STOWED AND DEPLOYED [1].....	5
FIGURE 3: INFRA, A COMBINATION OF THE PUMP ASSEMBLY AND THE FOIL RADIATOR [1].....	5
FIGURE 4: BODY MOUNTED PASSIVE RADIATOR [3].....	6
FIGURE 5: S/C WALL RADIATOR HEAT EXCHANGE BETWEEN PAYLOAD AND EXTERIOR SURFACE [4].....	7
FIGURE 6: DOUBLERS VS HEAT PIPES AND HEAT REJECTION BY A BLACK BODY RADIATOR [4].....	7
FIGURE 7: DEPLOYABLE AND ACTIVE RADIATOR ON THE ISS [4].....	8
FIGURE 8: ORIGAMI SOLAR PANEL [6].....	8
FIGURE 9: DEPLOYABLE SOLAR PANEL ISS [8].....	8
FIGURE 10: ROSA CAPTURED BY NASA AS IT IS BEING DEPLOYED AT THE END OF THE CANADARM2 [11].....	9
FIGURE 11: HIPER [13].....	9
FIGURE 12: HIPER LAMINATE	10
FIGURE 13: CONVENTIONAL AND A HIPER RADIATOR	10
FIGURE 14: BLACK BODY RADIATION SPECTRUM [19].....	12
FIGURE 15: RADIANT ENERGY AS FUNCTION OF WAVELENGTH, FOR BODY AT ROOM TEMPERATURE.....	12
FIGURE 16: VIEW FACTOR GEOMETRICAL DEFINITION [16].....	13
FIGURE 17: LINEAR CONDUCTIVE HEAT TRANSFER BETWEEN T1 AND T2.....	14
FIGURE 18: CONDUCTIVE RESISTANCE IN SERIES [24].....	15
FIGURE 19: PARALLEL THERMAL RESISTANCE ADDITION [24].....	15
FIGURE 20: RADIAL CONDUCTION.....	15
FIGURE 21: DYNEEMA TEST THREAD	19
FIGURE 22: CREEP TEST OBSERVATIONS DURING VARIOUS DATES AND TIMES.....	19
FIGURE 23: GEOMETRIC COMPARISON OF NEEDLE INITIAL POSITION T1 (LEFT) AND AT T2 (RIGHT)	20
FIGURE 24: INFLATED PET/PE HEAT-WELDED TUBE	20
FIGURE 25: BENDING TEST SETUP.....	20
FIGURE 26: FR BREADBOARD MODEL MADE FROM PET/PE AND PRESSURIZED WITH AIR AT ONE BAR PRESSURE GAUGE	21
FIGURE 27: SIMPLIFIED DEPLOYMENT TESTS: ROLL-OFF ON A FLAT SURFACE (LEFT), SIDEWAYS INFLATION OF SINGLE TUBE (RIGHT)	22
FIGURE 28: THE REDUCTION OF TENSILE FORCE WITHIN THE FR AS A RESULT OF FRICTION FORCES WHILE WOUNDED AROUND THE FRRS	23
FIGURE 29: BENDING TEST ITEM.....	23
FIGURE 30: LEO PARTICLES [38].....	24
FIGURE 31: CONCENTRATION OF RADIATION PARTICLES AND GASEOUS SPECIES AS FUNCTION OF ALTITUDE [38] ...	25
FIGURE 32: 15 YEAR DOSE IN GEO-EQUIVALENT PARTICLE ENVIRONMENT [42].....	26
FIGURE 33: INFRA V-MODEL.....	28
FIGURE 34: TORQUE MANEUVER CAUSES BENDING MOMENT ON THE BASE OF THE FR.....	32
FIGURE 35: FRA SUBSYSTEMS	34
FIGURE 36: FRA FINAL BREADBOARD DESIGN.....	34
FIGURE 37: FOIL RADIATOR MAIN CONCEPTS.....	35
FIGURE 38: BREADBOARDED "PARTY WHISTLE" CONCEPTS.....	36
FIGURE 39: FR TUBING DESIGN OPTIONS.....	36
FIGURE 40: TUBING INTERFACE CONCEPTS	38
FIGURE 41: TUBING-LAMINATE INTERFACES.....	38
FIGURE 42: SHARP ANGLE MAY CAUSE DELAMINATION WITHIN THE LAMINATE (LEFT) FLATTENING TUBE DOES NOT AFFECT WITH OF UNDERLYING LAMINATE (RIGHT).....	39
FIGURE 43: LAY-UP INTERFACE 1 & 2	39
FIGURE 44: FR TUBE SPACING CONCEPTS.....	39
FIGURE 45: HEAT SEALED PET/PE TUBING AS INTERFACE BETWEEN VARIOUS SIZED TUBING	40
FIGURE 46: CORNER CONNECTORS AND FR/PA INTERFACES	40
FIGURE 47: CONNECTOR CONCEPTS.....	40
FIGURE 48: CONNECTOR CONCEPT 3 BREADBOARD TEST	41
FIGURE 49: CORNER CONNECTOR	41
FIGURE 50: FRRS (LEFT), STOWING OF THE FRRS IN THE HDRM (RIGHT)	42
FIGURE 51: FRRS TO FR INTERFACE: FOIL TENSION LEGS AND STRIPS	42
FIGURE 52: ROLLER: 3D CAD DESIGN, TO 3D PRINTED PROTOTYPE, TO 3D PRINTED BREADBOARD MODEL.....	42
FIGURE 53: FRRS BAR.....	43
FIGURE 54: FOIL RADIATOR FIXATION 3D DESIGN TO BREADBOARD MODEL AND MOUNTING OF HDRM ONTO FRF	43

FIGURE 55: HDRM CONCEPTUAL DESIGN	44
FIGURE 56: THERMAL KNIFE SPRING SOCKETS	44
FIGURE 57: HDRM BREADBOARD MODEL	45
FIGURE 58: RADIATOR ROLL-UP TOOLING	45
FIGURE 59: PRE-TENSIONING SUPPORTS	46
FIGURE 60: HOVER DISK DEPLOYMENT PLATFORM AND DEPLOYMENT SUPPORT STRUCTURE	46
FIGURE 61: FR THERMAL MODEL RADIATOR NODES	47
FIGURE 62: OUT OF PLANE TUBE NODE LOCATIONS	48
FIGURE 63: FRF NODES	49
FIGURE 64: FRRS NODES	50
FIGURE 65: CONDUCTIVE COUPLING FROM CORNER CONNECTOR TO CENTER OF ROLLER.....	50
FIGURE 66: IR HEAT OUTPUT OF THE FR FOR VARYING ENVIRONMENTAL TEMPERATURES	52
FIGURE 67: COMPARISON OF 3D MAIN MODEL WITH TWO DIFFERENT 2D MODELS IN VACUUM (T = -80 °C).....	52
FIGURE 68: COMPARISON OF 3D MAIN MODEL WITH TWO DIFFERENT 2D MODELS IN SPACE ENVIRONMENT (T = - 270 °C)	52
FIGURE 69: FRA SYSTEM MASS (LEFT) AND AREA TO MASS (RIGHT) CONTOURS WITH RESPECT TO SCALING OF FR LENGTH AND WIDTH.....	53
FIGURE 70: CRITICAL LOCATIONS ON THE ROLLER WITH RESPECT TO A RADially EXERTED COMPRESSIVE LAUNCH LOAD.....	56
FIGURE 71: TUBE INTERFACE	57
FIGURE 72: LAYERS WHICH ARE PENETRATED	57
FIGURE 73: VELOCITY REQUIRED TO PUNCTURE KAPTON FOR VARIOUS DENSITIES AND THE RELATED SHEAR FORCE	59
FIGURE 74: COMPARISON OF ENERGY METHOD WITH BALLISTIC LIMIT EQUATION FOR VARIOUS DENSITIES.....	60
FIGURE 75: VELOCITY PROFILE OF THE METEOROID FLUX DISTRIBUTION $\Delta F/\Delta V$ FOR SPHERICAL TARGETS ON TYPICAL EARTH ORBITS [39].....	61
FIGURE 76: PREDICTED CUMULATIVE METEOROID FLUX IN A HELIOCENTRIC SYSTEM AT 1 AU, DUE TO METEOROIDS OF MASSES LARGER THAN m_{min} [39].....	61
FIGURE 77: ROLLING UP THE FR (LEFT), DEPLOYMENT TEST SETUP (RIGHT)	67
FIGURE 78: RS DEPLOYMENT TEST SETUP	69
FIGURE 79: DYNEEMA THREAD THERMAL KNIFE CUTTING TESTS.....	70
FIGURE 80: HDRM TEST	70
FIGURE 81: BENDING TEST: POINT LOAD (LEFT), DEFLECTION MEASUREMENT (RIGHT).....	71
FIGURE 82: FR IS DEFLECTED ($\Delta = 0,5$ M) BY MEANS OF AN UNSTER	72
FIGURE 83: FR STANDING SETUP (LEFT), THERMAL BATH OR "PA DUMMY" (RIGHT).....	73
FIGURE 84: FR THERMOCOUPLES NUMBER AND LOCATION	74
FIGURE 85: HEAT OUTPUT FR IN UPRIGHT (LEFT) AND LYING POSITION (RIGHT), DETERMINED FROM EQ. (2.33).....	74
FIGURE 86: ESTIMATED AND MEASURED ENVIRONMENTAL TEMPERATURES DURING THE FR TESTS	75
FIGURE 87: FR IR IMAGE DURING THERMAL TEST (LEFT) THERMOCOUPLE LOCATIONS (RIGHT)	76
FIGURE 88: SIMPLIFIED THERMAL NETWORK OF A SINGLE FR FIN CROSS SECTION	76
FIGURE 89: FR HEAT DISSIPATION DURING RS TEST FOR VARIOUS MASS FLOWS	79
FIGURE 90: FR MEASURED IN- AND OUTLET TEMPERATURES	79
FIGURE 91: EXPECTED FR SURFACE HEAT DISSIPATION VS. MEASURED FLUID HEAT DISSIPATION	80
FIGURE 92: ISOLATED NODE 1, 2, 3.....	80
FIGURE 93: FR AREA, ABOVE OPTICAL TABLE AREA.....	82
FIGURE 94: DEPLOYMENT SUPPORT OPTIONS	95
FIGURE 95: CONNECTOR DESIGN UPDATE: ASSEMBLED (TOP) AND PARTS (BOTTOM)	96
FIGURE 96: ROLL SUPPORT TYPES: TUBE ROLLER (LEFT) AND FOIL ROLLER (RIGHT)	96
FIGURE 97: FOIL ATTACHMENT CONCEPTS.....	96
FIGURE 98: ADDITIONAL NODES.....	97

List of tables

TABLE 1: RESEARCH QUESTIONS	4
TABLE 2: TYPICAL BEGINNING OF LIFE (BOL) OPTICAL PROPERTIES OF DIFFERENT MATERIALS [20].....	13
TABLE 3: SOME CONVECTIVE HEAT TRANSFER COEFFICIENTS [17]	16
TABLE 4: HEAT TRANSFER COEFFICIENT FOR VARIOUS FLOW RATES.....	17
TABLE 5: NATURAL CONVECTION HEAT TRANSFER COEFFICIENTS FOR DIFFERENTLY ORIENTED SURFACES.....	18
TABLE 6: TIME BETWEEN COLLISIONS WITH PARTICLE SIZES ON A 1 m ² SPHERICAL SURFACE MODELED BY MASTER- 2001 [37]	25
TABLE 7: KEY- CUSTOMER REQUIREMENTS	29
TABLE 8: REQUIREMENT VERIFICATION METHODS.....	29
TABLE 9: SYSTEM REQUIREMENTS	30
TABLE 10: TRADE OFF TUBE CONCEPT.....	35
TABLE 11: THIN WALLED COTS MATERIAL SELECTION.....	37
TABLE 12: INTERFACE TRADE OFF.....	38
TABLE 13: FRA TOOLING.....	45
TABLE 14: ENVIRONMENT SETTINGS.....	50
TABLE 15: HEAT BALANCE IN THE FR	51
TABLE 16: FIRST ORDER ESTIMATED HEAT OUTPUT FR	51
TABLE 17: FRA ESTIMATED SYSTEM MASS.....	53
TABLE 18: FR STRUCTURAL ANALYSIS TO VERIFY SYSTEM REQUIREMENTS	54
TABLE 19: FR BENDING MOMENTS DURING OPERATIONAL LOAD	54
TABLE 20: FRRS STRUCTURAL ANALYSIS TO VERIFY SYSTEM REQUIREMENTS.....	56
TABLE 21: EIGEN FREQUENCIES FRRS	56
TABLE 22: FRRS STRUCTURAL ANALYSIS TO VERIFY SYSTEM REQUIREMENTS.....	57
TABLE 23: COMPARED IMPACT RESULTS FROM [47].....	58
TABLE 24:BALLISTIC EQUATION CALIBRATED CONSTANTS OF A SINGLE WALL BALLISTIC LIMIT EQUATION [39]	59
TABLE 25: PROBABILITY OF A COLLISION WITH A MASS THAT MAY PUNCTURE THE FR RELATED TO EXPOSURE TIME	62
TABLE 26: STAINLESS STEEL TYPE 304 MATERIAL PROPERTIES [48].....	62
TABLE 27: PROBABILITY OF COLLISION BETWEEN MMOD AND RANDOMLY TUMBLING PLATE OR A SPHERE WITH <i>A_{cross}</i> = 0,05 m ² IN GEO ANALYZED BY DRAMA AND THE DATE SETTINGS OF THE MODEL.....	63
TABLE 28:PROBABILITY OF A COLLISION OF MMOD WITH MASS <i>m_{min}</i> , WITH THE FR TUBE RELATED TO EXPOSURE TIME.....	63
TABLE 29: SYSTEM REQUIREMENTS AND VERIFICATION METHODS	66
TABLE 30: FR TEST OBSERVATIONS AND DEPLOYMENT VERIFICATION.....	68
TABLE 31: RS TEST OBSERVATIONS AND DEPLOYMENT VERIFICATION.....	69
TABLE 32: HDRM THREAD CUTTING RESULTS	70
TABLE 33: BENDING DEFLECTIONS OF FR TIP FOR VARIOUS PRESSURES.....	71
TABLE 34: FIRST NATURAL FREQUENCIES FR+FRRS.....	72
TABLE 35: MAXIMUM DEFLECTION TEST	72
TABLE 36: STEADY STATE TEMPERATURES MEASURED IN THE FRF AND FRRS THERMOCOUPLES BEFORE THE TEST	75
TABLE 37: INITIAL AND FINAL TEMPERATURES OF THE FRF AND FRRS THERMOCOUPLES DURING TESTS WITH IDENTIFIED ENVIRONMENTAL TEMPERATURES	75
TABLE 38: NATURAL CONVECTION DISTRIBUTION OVER MEASURED CROSS SECTION	77
TABLE 39: NOMINAL SETTINGS WHICH ARE UNALTERED DURING THE CORRELATION HOWEVER WHICH IMPACT THE CROSS-SECTION TEMPERATURES	77
TABLE 40: NATURAL CONVECTION HEAT TRANSFER COEFFICIENT CORRELATED WITH TEST DATA.....	77
TABLE 41: ENVIRONMENTAL TEMPERATURES DURING TESTS	78
TABLE 42: RS TEST MEASURED PARAMETERS AND FR HEAT DISSIPATION.....	78
TABLE 43: HEAT TRANSFER RELATED TO TEMPERATURE DIFFERENCE IN THE INTERFACE	81
TABLE 44: CORRELATED TEMPERATURE DIFFERENCE BETWEEN N1 AND N3	81
TABLE 45: PREDICTED PERFORMANCE THERMAL MODEL.....	82
TABLE 46: VERIFICATION OVERVIEW OF THE FRA	84
TABLE 47: HEAT BALANCE IN THE FRRS	99
TABLE 48: FIRST ORDER ESTIMATED HEAT OUTPUT FRRS	99
TABLE 49: STEADY STATE TEMPERATURES IN FRRS NODES.....	99

Abbreviations

A	Analysis
ADSN	Airbus Defence and Space Netherlands B.V.
AE8 MAX	Electron fluxes for solar maximum conditions
AIT	Assembly Integration & Testing
AOCS	Attitude and Orbit Control System
AP8 MIN	Proton fluxes for solar minimum conditions
ATS-6	Applications Technology Satellite
BB	Breadboard
BOL	Beginning Of Life
COTS	Commercial Off The Shelf
DRAMA	Debris Risk Assessment and Mitigation Analysis
ESA	European Space Agency
ESH	Equivalent Solar Hours
FR	Foil Radiator
FRA	Foil Radiator Assembly
FRF	Foil Radiator Fixation
FRRS	Foil Radiator Roll Support
GEO	Geostationary Orbit
HDRM	Hold Down and Release Mechanism
HiPeR	High Performance Radiator
HOQ	House Of Quality
I	Inspection
i/f	Interface
INFRA	Inflatable Radiator
IR	Infra-Red
ISS	International Space Station
ITSAT	Inflatable Torus Solar Array Technology
LEO	Low Earth Orbit
LHP	Loop Heat pipe
MASTER	Meteoroid and Space Debris Terrestrial Environment Reference
μ-MPL	Micro- Mechanically Pumped Loop
MHRM	Multipurpose Hold down and Release Mechanism
MIDAS	MASTER(-based) Impact Flux and Damage Assessment
MLI	Multi-Layer Insulation
MMOD	Micrometeorites and Orbital Debris
MOP	Maximum Operating Pressure
NASA	National Aeronautics and Space Administration
NLR	The Dutch Aerospace Laboratory
OSR	Optical Solar Reflector
PA	Pump Assembly
PEEK	Poly Ether Ether Ketone
PE	Polyethylene
PET	Polyethylene terephthalate
PG	Pyrolytic Graphite
PGS	Pyrolytic Graphite Sheet
PI	Polyimide
PID	Proportional Integral Derivative
PUR	Poly Urethane
RoD	Review of Design
ROSA	Roll Out Solar Array
RS	Radiator System
S/C	Spacecraft
SE	Systems Engineering
SR	System Requirements
ST4	Space Technology 4
T	Testing
tc	Thermocouple
TRL	Technology Readiness Level
UC	Use Case
UCS	Use Case Scenario

US United States
UV Ultra Violet
V&V Verification and Validation

List of symbols

a_{ang}	Angular acceleration, rad/s^2	α	Absorptivity
a_{tan}	Tangential acceleration, m/s^2	β	Constant for determining ballistic equation
A	Area, m^2	γ	Correlation factor related to buckling modes
B	Width, m	$\Delta\gamma$	Axial compressive buckling stress coefficient
C	Conductive coupling, W/K	δ	Deflection, m
C_{or}	Geometry constant used for convection	ε	Emissivity
C_p	Specific heat capacity, $J/kg \cdot K$	ζ	Damping ratio
d	Depth, m	η	Efficiency
D	Diameter, m	θ	Deployment cone Angle, $^\circ$
Do	Absorbed radiation Dose, $Mrad$	κ	Conductivity, $W/m \cdot K$
E	Youngs modulus, GPa	λ	Wavelength, m
E_{ir}	Earth IR flux, W/m^2	μ_d	Dynamic viscosity, $Pa \cdot s$
f	Frequency, Hz	μ_{fric}	Friction coefficient
F	Force, N	ν	Poisson ratio
G_{adv}	Advective coupling, W/K	ρ	Density, kg/m^3
Gl	Linear coupling, W/K	σ	Stress, MPa
Gr	Grashof number	σ_{sb}	Stefan Boltzmann constant, MPa
GR	Radiative coupling, m^2	τ	Torque, Nm
Gy	Gray, m^2/s^2	ϕ	View factor surface angle, rad
h	Planck's constant	\emptyset	Bending angle, $^\circ$
h_c	Heat transfer coefficient, $W/m^2 \cdot K$		
h_e	Elevation head, m		
I	Moment of Inertia, $kg \cdot m^2$		
k	Stiffness, N/m		
k_{bol}	Boltzmann constant, J/K		
k_f	Conductivity fluid, $W/m \cdot K$		
K	Material constant		
L	Length, m		
m	Mass, kg		
\dot{m}	Mass flow, kg/s		
M	Moment, Nm		
n	Number off (#)		
n_{nat}	Exponential constant used for convection		
N	Particle Flux, $m^{-1}s^{-1}$		
Nu	Nusselt number		
P	Pressure, bar		
$P(x)$	Probability of an event 'x'		
Pr	Prandtl number		
Q	Heat dissipation, W		
Q_f	Volume flow, m^3/s		
r	Radius, m		
R	Radiative coupling, W/K		
R_0	Initial radius, m		
Ra	Rayleigh number		
Re	Reynolds number		
s_f	Safety factor		
S	Solar flux, W/m^2		
S_a	Albedo Flux, W/m^2		
t	Time, s		
th	Thickness, m		
T	Temperature, K		
U	Voltage		
v	Velocity, m/s		
V	Volume, m^3		
W	Distributed load, N/m		
x	Distance on x-axis, m		
y	Distance on y-axis, m		
z	Cooling/heating constant		

1 Introduction

The Inflatable Radiator (INFRA) is an innovative concept for a Next Gen radiator which was originally proposed to ESA's call for Bottom-up Space technologies at low TRL (2014) by a few cooperating companies under which Airbus and the NLR. The general idea was founded on the low storage volume of the large deployed surface area of a butterfly wing. By combining the High-Performance Radiator (HiPeR) technology patented by Airbus Defence and Space Netherlands BV. (ADSN, which shall hereafter be referred to as Airbus), as well as Micro- Mechanically Pumped Loop (μ -MPL) technology patented by the NLR, the basis for a high performance, active, inflatable radiator was constructed.

This report describes how this idea is further developed and which choices are made during the design of this product, while complying with the customer (NLR & Airbus) requirements. The Design is manufactured and also tested to also deliver a proof of concept regarding its basic functionality. The contents of the report are structured as follows:

- Introduction
- Literature review
- System Requirements
- Design Description
- Deployment and Thermal testing
- Verification and Validation
- Conclusion
- Recommendation

In this chapter the problem and the scope shall be formulated.

1.1. Problem definition

This research project is based on a case study concerning the development of an inflatable deployable radiator breadboard model. The research project is commissioned by Airbus under the name of Inflatable Radiator (INFRA). The project is performed in collaboration with the Dutch Aerospace Centre (NLR) who shall provide the Pump Assembly (PA) which shall be integrated with the Foil Radiator Assembly (FRA) to form the Radiator System (RS). The RS is designed to transport dissipated heat away from a communication Spacecraft (S/C), by means of conductive, convective and radiative heat transfer. The heat is collected at a direct interface with the payload, and pumped into the FR by means of a single-phase fluid which is controlled by the PA. The PA controls the flow rate as well as the pressure, which allows for a controlled deployment by means of inflation of the FR. The fluid transfers heat to the FR by means of convection and conduction, and which is eventually used to dissipate the heat into lab environment, by means of infrared (IR) radiation and natural convection. The RS is designed for space, therefore the performance in the lab must be translated to expected performance in Space.

The main challenges and research opportunities in this project are identified in the means of transporting heat throughout the system effectively and to make the system flexible and strong enough to be stowed during launch and being inflated afterwards. However, it should also be stiff enough after deployment to deal with maneuvering loads, while taking into account the hazards which are imposed by the operating environment. Hazards such as, radiation and Micrometeorites and Orbital Debris (MMOD). Underlying are the following challenges:

- Design of the inflatable shape that can be (thermally and structurally) controlled by using a single loop containing a single-phase fluid
- Selection of tubing which can be exposed to pressure stresses, radiation and MMOD and provide flexibility and heat transfer
- Design of the tubing interfaces within the FR while considering heat transfer and flexibility
- Scalability of the design
- Design of a FR that demonstrates a competitive heat load to mass ratio as well as a low storage volume
- Design of a Hold Down and Release Mechanism, that can hold down the FR during launch, deploy the FR during tests as well as in space
- Design of a method of fixating the FR to the S/C wall

- Design of tooling to support a simulated zero-G deployment test
- Verifying performance characteristics of a purely radiative product in a convective environment at room temperature by means of modelling and correlation

These sub-challenges are all addressed throughout this report. Identified solutions can and have been discussed with the clients during project meetings, to make sure that the customer requirements are always up to date. Due to the variety of the challenges, solutions are provided with sufficient detail to make a decision to continue the development process. Almost every subject can be analyzed with unlimited in-depth focus, however that would in this project distract from the main goal, which is to build a breadboard model which can be tested to deliver a proof of the INFRA concept. The key word is pragmatism.

1.2. Scope

INFRA shall make use of the product knowledge of HiPeR technology developed by Airbus and the μ -MPL developed by NLR. The PA however, is developed by the NLR and therefore the design shall not be included in this report. Furthermore, the following constraints are placed on the scope of the research work in coordination with the customers:

- Heat circulation within the RS shall be performed by means of a mechanically pumped single-phase fluid loop and the amount of heat entering the system shall be controllable by means of payload heat generation and fluid flow rate
- The PA shall be designed and build by the NLR
- INFRA is identified by Airbus and the NLR as a promising concept for communication satellites. Therefore, the operating environment in Space shall be based on a Geostationary orbit
- Hyper velocity impact testing is out of the scope of this research; however, estimations can be made regarding the risks related to MMOD
- The deployment is tested while simulating 0 G in a lab environment
- The radiator breadboard model shall be in the order of $1 m^2$ and design scalability is a requirement
- The FR laminate shall be based on HiPeR materials and production techniques
- Additional tests such as radiation or vibration are not included. Verification of these requirements is to be performed by means of analysis or review of design.

2 Literature review

The strategy to cover the research topic with sufficient in-depth is, to start by obtaining a broad knowledge basis regarding radiator design and identify and explore considerations which are identified during this process. This step is performed during the literature review, of which the most important content is covered in this chapter. The structure which is present in the development of the theoretical basis is provided in the next section and is identified as a research framework. While performing the thesis research activities, the knowledge basis provided to be most helpful in developing and researching parts of the radiator system.

2.1. Research definition

The objective of the INFRA project is to develop a breadboard model to further increase the TRL of the product and to demonstrate successful cooperation between the NLR and Airbus to enhance the relations and build a foundation for future Thermal/mechanical projects.

The objective of the Thesis research project will be, to find out how to develop and deliver a breadboard model of an inflatable radiator that fulfills the customer expectations, while keeping in mind the perspective on future developments. The emphasis shall be on delivering a functioning product which complies with the system requirements which are checked by and accepted by the clients.

The means of obtaining the research objective are described in this section. The framework is used to categorize the research questions which contribute pieces of knowledge to the main research question, which is:

“How to develop a state of the art radiator breadboard, which fulfills the customer requirements?”

The research framework can be seen in Figure 1. The research framework structures the phases of the project and also provides the research topics for the research work.

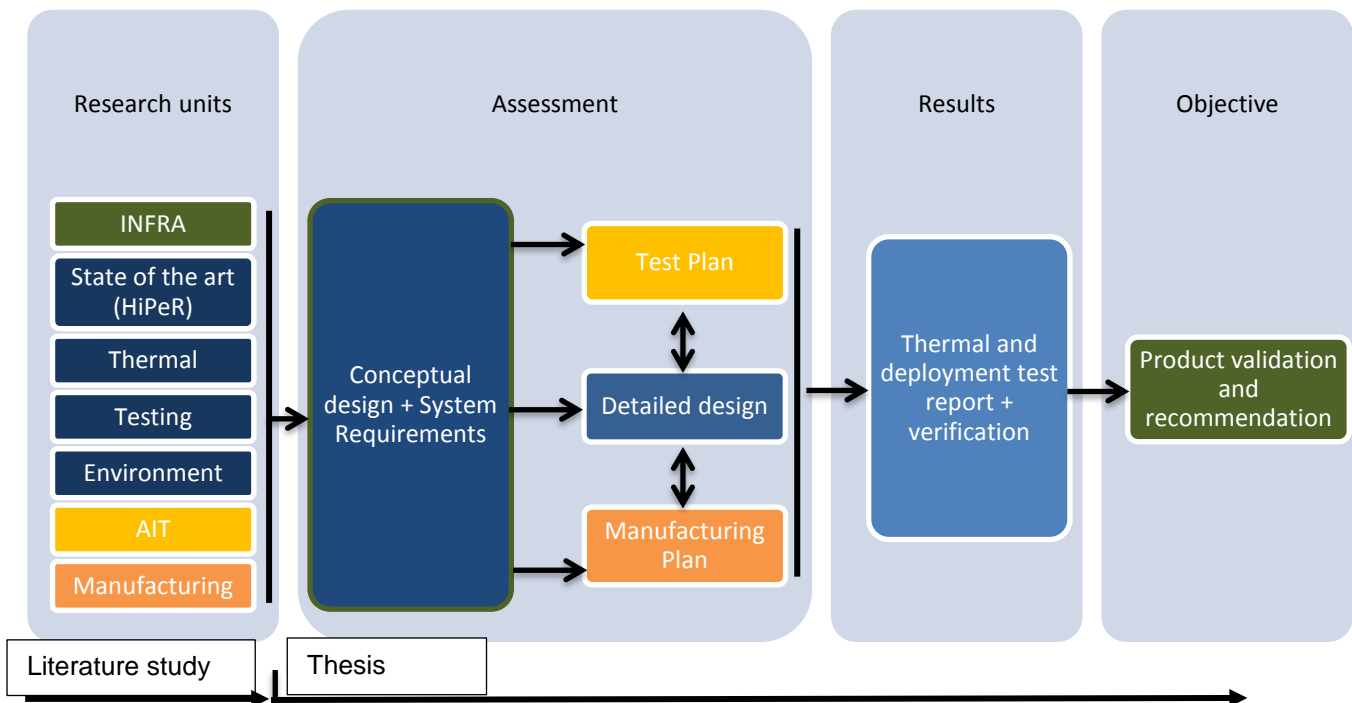


Figure 1: Research framework

Belonging to each research topic are several research questions which are answered in this report. The most important sub-questions are summarized in Table 1 and are answered at the end of the various chapters in the report.

Table 1: Research questions

Research Project phase	Chapter	Research question
Main research question	Introduction/ Conclusion	How to develop a low mass, deployable and inflatable radiator breadboard model, which is based on the state of the art technologies that were contributed by the INFRA project member companies, which would be regarded as a competitive design?
Literature review	INFRA	What is INFRA and how can this graduation research work contribute to the INFRA project?
	State of the art	How to utilize HiPeR within INFRA and what is the state of the art?
	Thermal theory	Which thermal theory is applicable to the design and verification of the FR?
	Breadboard testing	Which tests are required to obtain some working knowledge on the functionality of the FRA?
	GEO Environment	Which environments are to be considered for the design of the breadboard model and how will these environments impact the design choices?
Assessment	Stakeholder requirements	Who are the main stakeholders, what are their needs and requirements and how will these influence the system requirements?
	System requirements	What are proper system requirements for the INFRA breadboard model that reflect the customer requirements and in what manner can these be verified?
	Foil Radiator Assembly (FRA)	What is a feasible radiator design for INFRA that may potentially fulfill the main system requirements, and which tubing type and interface should be selected? Are there additional systems required to support the functionality of the FR?
	FR Thermal model	How can the FR be modeled such that its performance in the lab test as well as in Space can be predicted and which error can be accomplished? Is this error reasonable?
	Structural	Which parts of the design must be analyzed to verify the system requirements and which cases are critical under the identified load cases?
	MMOD risk analysis	How large is the risk that MMOD poses to INFRA and what is the life expectancy of the current design? How does this compare to a metal tube design?
Results	Deployment test	How to verify the deployment requirements by testing and does the test verify the deployment requirements?
	Deployment test Bending test	How to verify the bending requirements by testing and does the test verify the bending requirements?
	Thermal balance test	How to verify the thermal performance requirements by testing and does the test verify the thermal performance requirements?
	Requirements verification	Are the system requirements verified? What are the consequences of any failure to comply with the requirements?
	Requirements validation	Are the customer requirements validated? What are the consequences of any failure to comply with the requirements?
	Conclusion/ Recommendations	What are lessons learned from the project and what are any recommendations that can be produced for any part of the product?

Note that the chapters which answer multiple research questions, have a dedicated section in which these are answered.

2.2. INFRA

INFRA is the cooperative project between AIRBUS and the NLR. The proposed design is that of a radiator analogous to a butterfly wing. Whereby fluid provides the internal pressure to unfold the structure but also provides heat transport from the payload to the radiating surface. The INFRA concept as a whole is currently evaluated at TRL 2 and the target is to improve the status of the concept to TRL 4 by means of demonstrating and testing a breadboard model. A concept which is shown in the original proposal to ESA's call for low TRL technologies (2014) [1], in both stowed and deployed state can be seen in Figure 2. The TRL verification is however not included in this thesis.

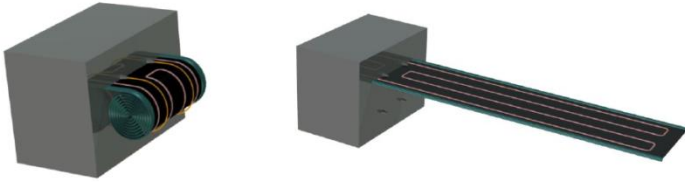


Figure 2: Inflatable radiator concept; stowed and deployed [1]

The concept exists out of two parts, the Pump Assembly (PA) and the Foil Radiator (FR). The Pump Assembly is developed by the NLR and the FR is the developed by Airbus. This graduation assignment only concerns the FR and the integration with the PA, but not the development of the PA. The combined system can be seen in Figure 3.

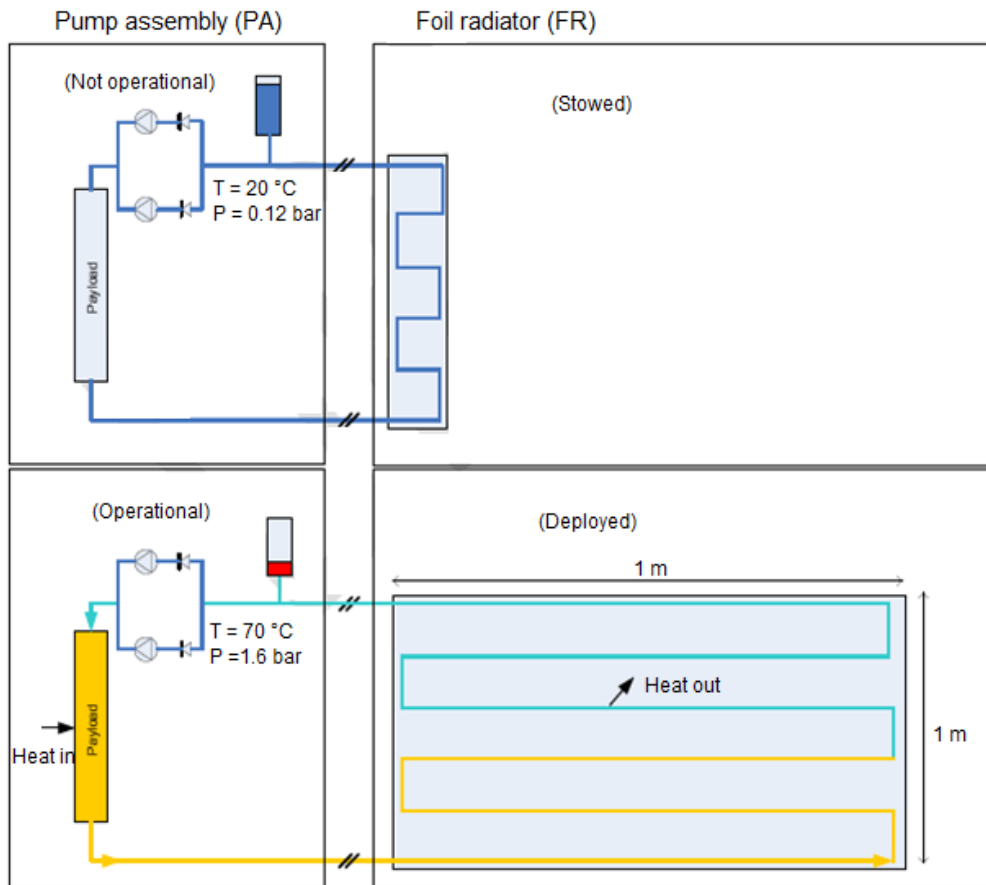


Figure 3: INFRA, a combination of the Pump Assembly and the Foil Radiator [1]

The proposed technologies are the HiPeR suite by Airbus, and the μ -MPL plus accumulator technologies by the NLR. However, for the functionality of the product, other technologies and improvisations may be required. The aim of this project, is to develop a high performance, deployable and inflatable radiator which has the potential to become a market changing product.

2.2.1. Business opportunities

According to the original proposal [1], the product is expected to provide a commercial benefit at system level and is therefore protected intellectually as such. INFRA is expected to provide opportunities on the communication satellite market because a trend is noticed of increasing payload power dissipation requirements, which could potentially be fulfilled by the small stowed volume high heat transfer radiator system. Typically, these S/C do not have sufficient area on the North/South walls to place radiator systems. Therefore, the communication sat business requires deployable radiator surfaces which can be stowed and deployed in close vicinity of the communication antennas and INFRA is aiming to offer a low mass, high performance solution. It is also expected that due to the increasing use of electrical propulsion the demand for low storage, high power radiator systems will increase.

Market segments which could benefit from the system according to [1] are:

- Telecommunication satellites and satellites using Ka- band often have small areas to place radiators
- By stimulating the use of electrical propulsion, propellant mass is heavily reduced and this launch mass may be replaced for example by an enhanced payload system
- MEO/GEO communications or navigations systems which have a variable solar aspect angle non-fixed radiator
- Manned missions require massive heat rejection systems, e.g. ISS generates 90 kW of power, which is a factor ten of a typical communications satellite. However, it is difficult to transport large panels to space, inflatables may offer a solution
- Small satellites can be provided a considerable payload carrying possibility by using an inflatable radiator to reject heat

Generally, the INFRA design is expected to provide disruptive technology specifically since it provides:

- A very compact stowed volume
- Radiator concept to be applicable to various missions
- European alternative to US stowing concepts (No US license required)
- Low mass (target <15 kg/kW), while state of the art deployable radiators offers ≥ 20 kg/kW
- Low cost as it has: reduced number of hold-down points, absence of mechanisms, simple manufacturing techniques (no bake-out of panels), simple non-destructive inspections.
- Less requirements for size optimization due to already small stowed volume

In the following section, the state of the art shall be discussed regarding this area of expertise.

2.3. State of the art

Radiators are thermal control systems which can be active or passive systems. Thermal control systems are discussed broadly in [2]. Examples of passive thermal control systems are coatings, Multi-Layer Insulation (MLI) blankets, latent heat an ablation surfaces and phase change materials. Often these are placed in contact with objects such as doublers, fillers, thermal straps or foam to produce either a highly conductive or an isolative thermal path. Active thermal control can be performed by means of fluid loops, which can be controlled as they may have variable conductance or a pump to regulate the heat flow. Thermal control can also be performed by electrical heaters which are equipped with a thermostat to set the temperature. Also, mechanically controlled panels or 'louvres' may be used to control the amount of heat entering or leaving the S/C. For example, Rosetta is equipped with louvres which open up to expose the radiators to cold space to dump heat, while they close while the temperature of the S/C is low. Furthermore, passive systems are simple to design, low mass and cost, and highly reliable. The downside however is that passive radiators do not offer high heat transport capabilities which active radiators do. The downside of active radiators is that they are complex to design, are higher in mass and costs, more difficult to test and less reliable since they are based on more complex systems [2].

The conventional types of passive radiators are body mounted plates, structural panels with or without heat pipes or deployable radiator types. The body mounted plates usually ensure local cooling for instruments. They may be connected to the instrument by a thermal strap to generate conductive heat flow, as can be seen in Figure 4. The straps can be covered in MLI to avoid heat from ending up in unwanted places [3]. The S/C wall may also function as a radiator.

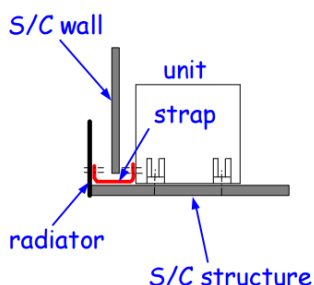


Figure 4: Body mounted passive radiator [3]

Passive radiators as seen in Figure 5 are often made from a carbon fiber or aluminum honeycomb laminate. The payload can be mounted to the rear of these panels or maybe connected by means of heat pipes.

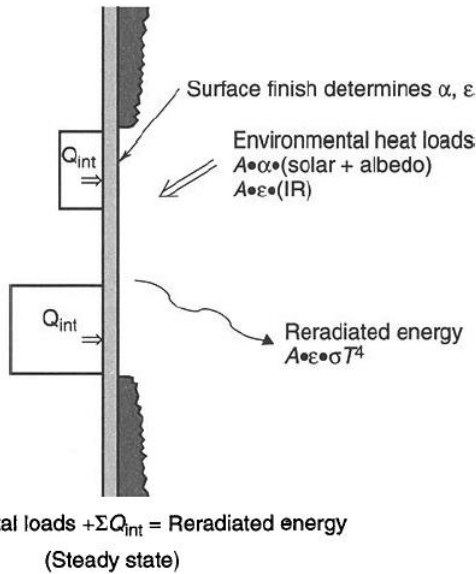


Figure 5: S/C wall radiator heat exchange between payload and exterior surface [4]

Thermal doublers or heat pipes can also be used to improve the in plane conductive heat transport in the faceplates of the panel. It can be noticed from Figure 6, that there is a certain range of panel temperatures where heat pipes can offer a relatively low mass solution to doublers.

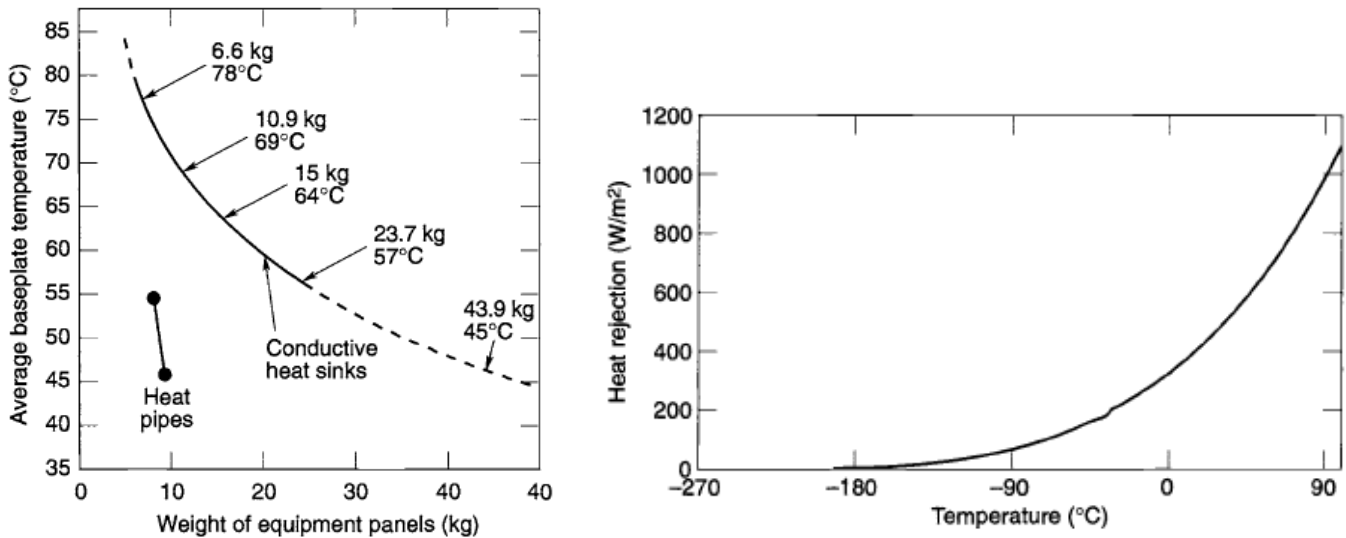


Figure 6: Doublers vs heat pipes and heat rejection by a black body radiator [4]

The sandwich panel core provides the out of plane conductive heat transport along with some radiative heat exchange between the faceplates [5]. The temperature as well as the optical coating of the radiator can be designed to dissipate the required heat. A perfect radiator, assuming it is only seeing Space, has an optical property called emissivity $\epsilon = 1$, which is also referred to in thermal engineering as 'black body'. This allows optimal IR radiative heat transfer to Space, depending on the temperature and size of the radiator as can be seen also be seen in Figure 6. Altogether this provides an effective method of transporting heat to the radiator surface. However, since the radiator is also used for structural purposes, this limits the maximum heat transfer due to the available surface area.

To compensate for this limitation, deployable radiators are mostly used. An example of a famous deployable radiator is the series which are developed by Lockheed Martin and Void systems and which is still used on the International Space Station (ISS) (Figure 7). This radiator is also active as it has a pumped ammonia fluid loop that transport 16 kW out to each radiator [4].

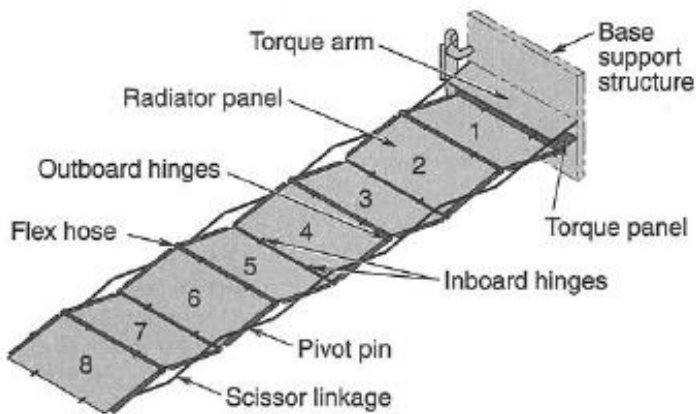


Figure 7: Deployable and active radiator on the ISS [4]

These systems are however based on complexly hinged panels which adds mass to the system which could have been spared or be used for payload or fuel or any other important use. These complex folding structures can also be made by using origami techniques which can be seen in Figure 8.



Figure 8: Origami solar panel [6]

Experiments with origami solar panels are described in [6],[7]. In case this technique would be used for the inflatable radiator, the deployment could occur by means of internal pressure in the structure.

Another example of a hinged low storage volume, high surface area system is the solar panel of the ISS which is seen in Figure 9. This method uses a centralized structure which is deployed from the main body and which extracts the solar panel which is hinged and tightly stacked like an accordion.

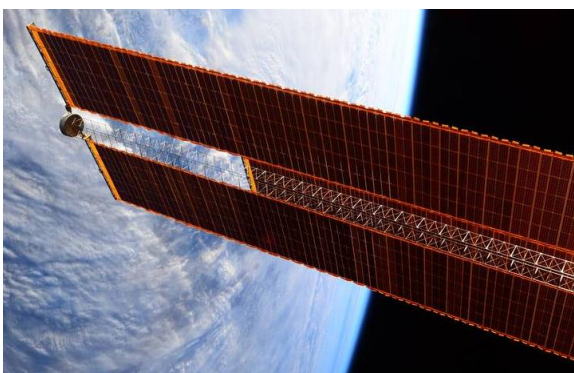


Figure 9: Deployable Solar panel ISS [8]

To save mass even further, inflatable rods are often used to provide the structural stiffness and deployment force to unroll or deploy the solar panel. These specific space structures are developed under the name of Gossamer Spacecraft. By means of inflation and rigidizing the beam afterwards, the pressure is not any longer required, which reduces the risks related to leaks after deployment by MMOD. Several “short term” applications which are considered with this technology are solar arrays, sunshields, rovers and high precision structures as radar and reflect antennas [9]. Several systems have also been developed using these techniques such as the Inflatable Torus Solar Array Technology (ITSAT), the Champollion (ST4) solar array and the Teledesic Inflatable Solar Array. Only recently there has been an experiment on the ISS with a Roll-Out Solar Array (ROSA), which can be seen in Figure 10. According to the NASA website, tests have been scheduled relating to the deployment and retraction capabilities but also tests related to shape changes with temperature and other strength and durability related aspects of the flexible solar array [10].

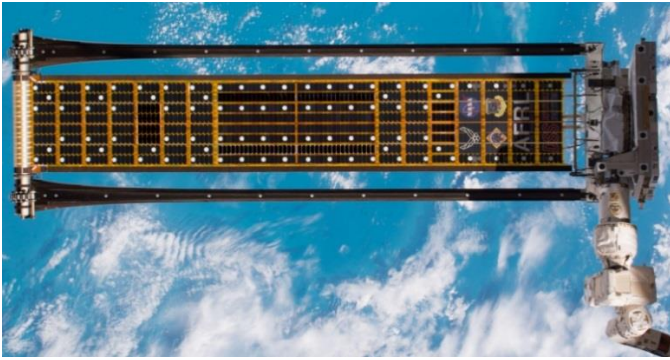


Figure 10: ROSA captured by NASA as it is being deployed at the end of the Canadarm2 [11]

These methods may be interesting, however for INFRA a different approach is envisaged which utilizes the fluid in the tube not only for providing the structural stiffness, but also for transporting heat into the system. This combines both functionalities such that no additional cylinder to hold and inject the gas which only inflates the beam or deployment mechanisms are required which become useless afterwards. The tubing which is required to transport the heat is also one of the main reasons why there have been developed so many flexible solar panels, but not yet flexible (active) radiators. Since a leak can easily disrupt a system which is dependent on pressure, which is a significant risk due to the probability of a collision with Micro Meteoroids and Orbital Debris (MMOD). Relating to this, two inflatable radiator concepts were investigated [12]. The concepts are: a rolling laminate with high tube spacing based on silvered Teflon fin material with a polyurethane, perfluoro elastomer or Teflon tube, and hard aluminum radiator tubes which are configured as helical spring and are connected with flexible Teflon coated silver wire mesh as fin. The deployment of the concepts is described as a 'party whistle' and a 'jack in the box'. The first baseline design characteristics are $A_{roll} = 250 \text{ ft}^2 = 23,2 \text{ m}^2$ with a mass of $m_{roll} = 96 \text{ lb} = 43,5 \text{ kg}$ ($\Rightarrow 1,8 \text{ kg/m}^2$). The life expectancy of this concept however is expected to be with a probability of $P = 0,9$, $t_{puncture \text{ roll}} = 2 \text{ days}$. A materials study improved the lifetime to 30 days. The second baseline design has $A_{spring} = 463 \text{ ft}^2 = 43,0 \text{ m}^2$ with a mass of $m_{spring} = 233 \text{ lb} = 105,7 \text{ kg}$ ($\Rightarrow 2,5 \text{ kg/m}^2$). The latter also has a lifetime of 30 days. This makes the system useful for sporadic heat dumps however not for permanent deployment such as planned with INFRA. The cause of this short life expectancy, despite of the thick polymer or metal tubes, seems to be the huge tubing and small spacing between the tubes ($2,5 < w_{tube \text{ pitch}} < 3,5 \text{ cm}$). Since the exposed tubing area is relatively large with respect to total the radiator area the risk of a penetration with one of the tubes, is also considerably large.

Recently Airbus has developed flexible radiator technology under the name of HiPeR. HiPeR replaces the conventional radiator panel which is placed on the exterior of the wall of the S/C. Due to high heat transfer requirements these radiator panels are often equipped with "heavy" isostatic standoffs and MLI between the panels for Isolation. HiPeR may be placed on top of the MLI blanket with lightweight standoffs similar to the MLI type standoffs. This is possible since HiPeR is a low mass laminate which is made from Kapton and the highly thermally conductive Pyrolytic Graphite, which can be seen in Figure 11.

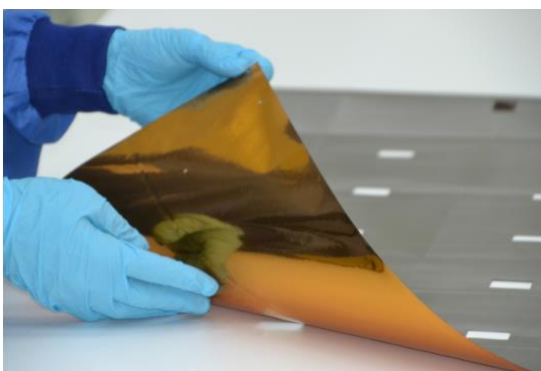


Figure 11: HiPeR [13]

Compared to conventional radiators, HiPeR demonstrates a high performance to mass ratio. Depending on the heat pipe spacing, the performance and the mass can be adjusted. Baseline HiPeR laminate is based on two layers of Pyrolytic Graphite Sheet (PGS), which are bonded to each other as can be seen in Figure 12.



Figure 12: HiPeR laminate

By means of a thermal model, HiPeR is compared with a conventional aluminum radiator to determine its performance and identify a realistic tube spacing. A situation is provided where a conventional radiator is equipped with conventional heat pipe and the HiPeR radiator is equipped with a saddle hat heat pipe. The situation is shown in Figure 13.

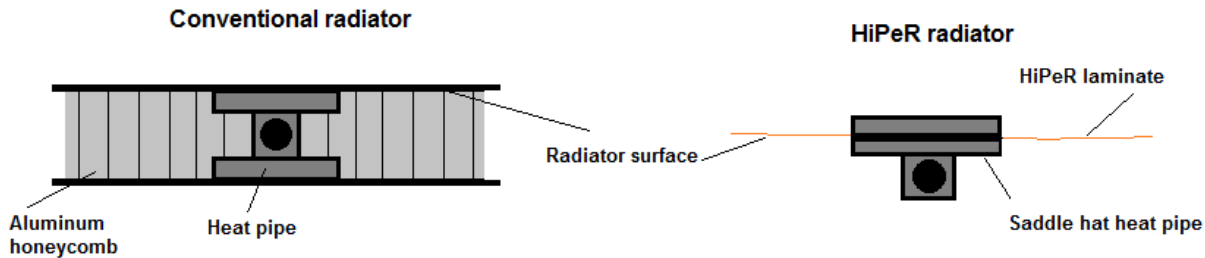


Figure 13: Conventional and a HiPeR radiator

It is assumed that both radiators have the same heat pipe contact area, an emissivity is assumed of $\epsilon = 0,8$ and that the contact conductance is infinite. The thickness of the aluminum sheets is set $t_w = 1mm$ each and fin length on both sides of the heat pipe $L_{fin} = 0,05 m$. The length of the heat pipe is $L_{hp} = 1 m$, and the heat pipes are maintained at a constant temperature $T = 296,15 K (= RT)$. The efficiencies, which are based on the ratio of actual over ideal heat dissipation are obtained: $\eta_{HiPeR} = 88\%$ for the HiPeR and $\eta_{alu} = 90\%$ for the conventional aluminum radiator when modelled in Space without additional heat sources. Comparing the mass of the conventional radiator which is made from commonly used aluminum 7075 T6, $m_{conv} = 1,2 kg$, and $m_{HiPeR} = 0,04 kg$ (excluding heat pipe mass for both cases). Both systems are able to radiate roughly $P_{diss} = 60 W$, which equals $600W/m^2$ for the given temperatures and efficiencies. That means that to obtain similar high efficiency's the aluminum radiator it theoretically 10 kg heavier than HiPeR per square meter in this specific scenario. Furthermore, this model also demonstrates that if the fin length is increased to $L_{fin} = 0,1 m$, the efficiency is still over $\eta_{HiPeR} > 83\%$, therefore INFRA may be designed with slightly higher than proposed fin spacing and still perform well. The saddle hat interface and a Loop Heat Pipes (LHP) however have been compared by an internal documented Airbus test [14], in which comparable high efficiencies are found for the saddle hat heat pipe, however lower efficiencies when equipped with a Loop Heat Pipe (LHP), between 75.6 and 55.8 %. This indicates a worse thermal interface, and in case tubing are used in the design, this order of magnitude in efficiencies should be taken into account.

We may however conclude that the HiPeR laminate provides the option to increase the tube spacing ($w_{tube\ pitch} \times 10$) while maintaining a high radiator efficiency and significantly decrease the exposed tubing surface area compared to the concepts which were mentioned before, to minimize the chance of being struck by MMOD.

2.4. Thermal theory

This chapter provides the basics of thermal theory, which is used to construct the thermal model of the radiator. In short, the applicable forms of heat transfer are discussed (conduction, convection forced/natural and radiation), but also how to determine the radiator fin efficiency.

2.4.1. Thermal equilibrium

A S/C which is in Orbit around Earth is exposed to several heat sources. External heat sources which are considered significant provide their energy to the S/C by means of radiation. In particular; Solar radiation, the Albedo which is reflected Solar radiation by Earth, and IR radiation originating from Earth [15]. For steady state analysis, it is assumed that the S/C has a high thermal inertia, that the S/C does not enter eclipse and the spacecraft is isothermal. The sum of the heat fluxes which are originating from those sources and are impinging on the S/C are shown in eq. (2.1) [16]. Included in the equation is solar flux (S), Solar albedo flux (S_a), thermal radiation flux originating from the Earth (E_{ir}) and heat which is dissipated by the S/C systems (Q_{int}). As a result of the law of conservation of energy, the heat which enters the S/C must also exit, which is performed by means of IR radiation.

$$\alpha A_s S + \alpha A_a S_a + \varepsilon A_{ir} E_{ir} + Q_{int} = \varepsilon A_{S/C} \sigma_{bm} T_{S/C}^4 \quad (2.1)$$

Where α = absorptivity of the surface, A_s is the area which is exposed to the Sun, ε is the IR emissivity of the surface, A_{ir} is the surface which is exposed to the IR radiation and E_{ir} is the IR radiative flux. A_{ext} is the S/C external area and σ is the Stefan-Boltzmann constant. $T_{S/C}$ is the steady state temperature of the external surfaces of the S/C. Convection and conduction however may occur within the S/C. Note the absorptivity of the S/C surface in IR frequency is equivalent to the emissivity according to Kirchhoff's law.

The steady state temperature of the S/C under these conditions can thus be found from eq. (2.2)

$$\left(\frac{\alpha A_s S + \alpha A_a S_a + \varepsilon A_{ir} E_{ir} + Q_{int}}{\varepsilon A_{S/C} \sigma_{bm}} \right)^{\frac{1}{4}} = T_{S/C} \quad (2.2)$$

The S/C can also be represented by a thermal mathematical model, in which isothermal nodes are used which represent the temperature of a region in which gradients are neglected. These nodes are defined by a temperature, thermal capacity, heat dissipation and thermal interfaces with other nodes. A combination of all heat exchange factors in a single isothermal node can be described by eq. (2.3) [16], which is used by software such as ESATAN ThermXL to determine the steady state or transient temperature for each node depending on the numerical scheme.

$$(mc_p)_i \frac{dT_i}{dt} = \alpha_i A_{s_i} S + \alpha_i A_{s_i} S_a + \varepsilon_i A_{ir_i} E_{ir} + Q_{int} - \sum_{j=1}^n R_{ij} \sigma_{bm} (T_i^4 - T_j^4) - \sum_{j=1}^n C_{ij} (T_i - T_j) \quad (2.3)$$

$R_{ij} = \varepsilon_i A_i B_{ij}$ and $C_{ij} = \frac{k_i A_i}{L_{ij}}$ are the conductive couplings and radiative couplings respectively, with Gebhart factor B_{ij} and thermal conductivity k_i and conductive path length L_{ij} , which are described in the following sections. For the design of the radiator, transient behavior is not analyzed and for the steady state analysis regarding the radiators thermal balance in space, the solar and infrared sources are also not taken into account. The emissivity of the environment and view factor towards it are in this study assumed to be $\varepsilon = 1$, $F_{FR-env} = 1$ and reflections between surfaces are identified to be small enough to be neglected in first order approximations and are used as uncertainties in the thermal model. Due to the presence of air in the lab environment, another term is added which accounts for natural convection. These assumptions transform the heat balance eq. (2.3) regarding the FR (in the lab)

$$Q_{int} = \varepsilon_i A_i \sigma (T_i^4 - T_{env}^4) + \sum_{j=1}^n C_{ij} (T_i - T_j) + h_{c_i} (T_i - T_{env}) \quad (2.4)$$

And eq. (2.5) can be used to obtain the average FR temperature T_{FR} , which uses the heat which is delivered internally by the fluid minus the losses Q_{losses} to components which are attached to the FR, and by taking into account a constant heat transfer coefficient due to natural convection h_{conv} .

$$Q_{int} - Q_{losses} = \varepsilon_{FR} A_{FR} \sigma_{bm} (T_{FR}^4 - T_{env}^4) + h_{conv} A_{FR} (T_{FR} - T_{env}) \quad (2.5)$$

2.4.2. Thermal radiation

Thermal radiation is electromagnetic energy that is expelled by bodies with an absolute temperature above 0 K [17]. A theoretical body that emits the maximum amount of heat for a given temperature is called a 'black body'. The emissivity (ε) of a body is explained as the fraction of energy that the body emits with respect to the amount which a 'black body' emits at a certain temperature as shown in (2.6). [18]

$$\varepsilon(T) = \frac{\int_0^{\infty} \varepsilon(\lambda) E_{\lambda} d\lambda}{\sigma_{bm} T^4} \quad (2.6)$$

Where ε and E are a function of wavelength, with T as temperature and σ as Stefan-Boltzmann constant. The energy of a black body which is radiated away as a function of wavelength (λ) and temperature (T) is described in eq. (2.7) by Planck which contains Planck's constant h , k_{bol} is the Boltzmann constant and c is the speed of light.

$$E_{\lambda,b} = \frac{2 \pi h c^2}{\lambda^5 [e^{\left(\frac{hc}{\lambda k_{bol} T}\right)} - 1]} \quad (2.7)$$

The energy is integrated with the emissivity over all wavelengths, to obtain the total energy radiated away by the body. The emissivity of a black body is by definition $\epsilon = 1$. This means that a black body absorbs and emits all wavelengths of radiation and does not reflect or transmit any energy according to the law of conservation of energy. [18]

Depending on the temperature, the wavelength of the maximum intensity is inversely varying. The surface temperature of the Sun is about 6000 K and behaves almost as a black body [19]. Wien's approximation, can be seen in Figure 14, which shows that the maximum spectral radiance is between 400-750 nm. Which is in the Ultra Violet (UV) and visible spectrum.

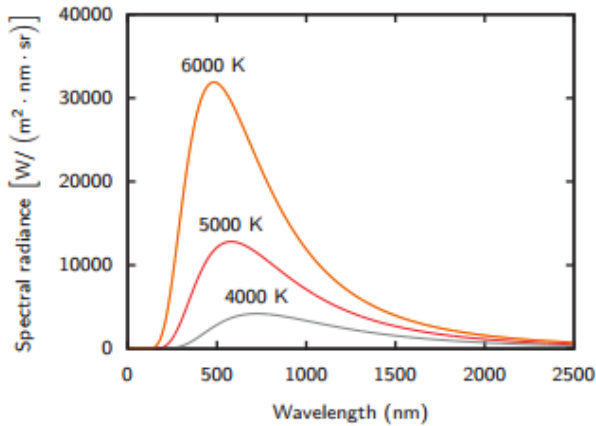


Figure 14: Black body radiation spectrum [19]

Furthermore, it can be seen in that the lower temperature body curves tend to peak at longer wavelengths. With this equation the wavelength can be compared at which the radiator emits most energy for example when it is at room temperature. A graph of this function for different wavelengths can be seen in Figure 15. It can be seen that a black body at room temperature emits most of its heat around the wavelength of 0.01 micron, which is 10 nm and is in the IR spectrum.

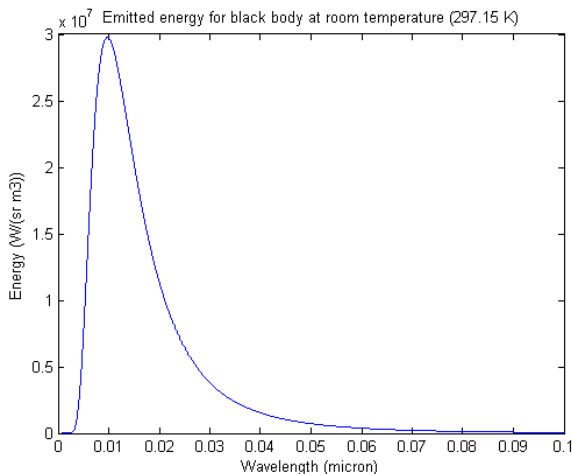


Figure 15: Radiant energy as function of wavelength, for body at room temperature

A real object is called a gray body that has $\epsilon < 1$. As a result, when radiation strikes the surface of a body, it may be partially absorbed (A), transmitted (T) or reflected (R). Since there must be conservation of energy these coefficients together are: $A + T + R = 1$. The radiative emission (ϵ) of a body according to Kirchhoff's law is equivalent to its absorptivity (A) for a given temperature and wavelength. Since the radiator is assumed an opaque surface with zero transmission, this leads to $A = 1 - R$. Therefore high reflection leads to low absorption and vice versa [18]. Optical solar reflectors (OSR's) make good use of this relation, since these are equipped with a combination of highly reflecting metals such as silver and highly emitting quartz.

The IR emissivity (and absorptivity) and the solar absorptivity of the FR is determined by the optical properties of Kapton. Materials may be selected that make use of this wavelength to absorb and emit heat. For example, white paint may be applied to the radiator which has the properties of a high emitter in the IR spectrum, and a low absorber in the solar spectrum. Some typical coatings can be seen in Table 2.

Table 2: Typical beginning of life (BOL) optical properties of different materials [20]

Material	Solar absorptance	IR emissivity
OSR, Silvered fused silica (Quartz)	0,07	0,80
3M black velvet paint	0,97	0,91
Z93 White paint	0,19	0,83
Silvered Teflon, 5 mil	0,08	0,81
Stainless steel	0,47	0,14

2.4.3. Radiative heat transfer

Radiative heat transfer between black bodies is based on view factors which are defined as the fraction of radiation leaving one surface that is intercepted by the other [16]. The view factor geometry can be seen in Figure 16.

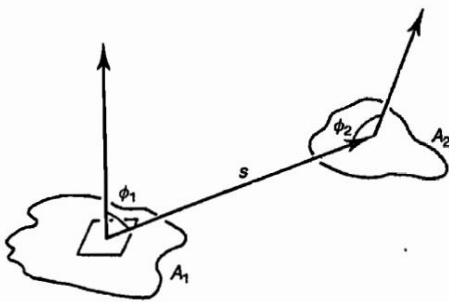


Figure 16: View factor geometrical definition [16]

The definition is generally described by eq. (2.8), which takes into account the geometry of multiple surfaces and the angles ϕ_i, ϕ_j between them. The sum of n view factors must be unity, $(\sum_{j=1}^n F_{ij} = 1)$ [16].

$$F_{ij}A_i = \int_{A_i} \int_{A_j} \frac{\cos \phi_i \cos \phi_j}{\pi s^2} dA_i dA_j \quad (2.8)$$

From the symmetry in the equation, a reciprocity relation is deduced [16]:

$$F_{ij}A_i = F_{ji}A_j \quad (2.9)$$

And as said before, the view factor is the heat being intercepted over the heat being emitted which is described by [21]:

$$F_{ij} = \frac{\text{Energy absorbed at } A_j \text{ originating as emission at } A_i}{\text{Total black body radiation emitted from } A_i \text{ at } T_i} = \frac{Q_{ij}}{A_i \sigma T_i^4} \quad (2.10)$$

The radiation between two surfaces can also be described using the Gebhart factor (B). This factor takes into account the reflections between surfaces which is applicable to grey bodies ($\varepsilon < 1; R > 0$). In [21] the definition of the Gebhart factor is derived:

$$B_{ij} = \frac{Q_{ij}}{\varepsilon_i A_i \sigma T_i^4} \quad (2.11)$$

By comparing eq. (2.11) with eq. (2.10) we may write:

$$A_i \varepsilon_i B_{ij} \sigma T_i^4 = A_i F_{ij} \sigma T_i^4 \quad (2.12)$$

From which the radiation exchange factor R_{ij} for black or grey bodies is identified:

$$R_{ij} = A_i \varepsilon_i B_{ij} = A_i F_{ij} \quad (2.13)$$

In which the sum of the Gebhart factors is also unity ($\sum_{j=1}^n R_{ij} = 1$). The heat exchange between the surfaces becomes:

$$Q_{ij} = A_i \varepsilon_i B_{ij} \sigma T_i^4 - A_j \varepsilon_j B_{ji} \sigma T_j^4 \quad (2.14)$$

And since the reciprocity relation is also found in the Gebhart factor ($A_i F_{ij} = A_j F_{ji} = \varepsilon_i A_i B_{ij} = \varepsilon_j A_j B_{ji}$), we obtain eq. (2.15) :

$$Q_{ij} = \varepsilon_i A_i B_{ij} \sigma (T_i^4 - T_j^4) \quad (2.15)$$

Furthermore, if surface A_j in an enclosure loses energy at a net rate of q_j . This can be written as shown in (2.16) [22]:

$$Q_j = \varepsilon_j A_j \sigma T_j^4 - \sum_{i=1}^n B_{ij} \varepsilon_i A_i \sigma T_i^4 \quad (2.16)$$

Which after some algebraic manipulation with the view factors, leads to the useful Gebhart factor equation, describing the fraction of radiation being emitted by i , and absorbed by j , including the radiation which is reflections by a number of surfaces (n_s) [22]:

$$B_{ij} = F_{ij} \varepsilon_j + \sum_{k=1}^{n_s} (1 - \varepsilon_k) F_{ik} B_{kj} \quad (2.17)$$

2.4.4. Conductive heat transfer

Thermal conductance is a very important form of heat transfer for the FR, since the heat which is delivered by the fluid, must be transported from the tube throughout the fins of the radiator. The heat which conducted is dependent on geometry and conductivity of the material. Since several conductive geometries are expected in the FR, this section elaborates on the effect of geometry and a combination of materials on heat transfer.

Linear conductive heat transfer can be found from eq. (2.18), where k represents the thermal conductivity, A the cross-sectional area and L the length of the thermal path and ΔT the temperature difference [16].

$$Q_{ij} = \frac{kA}{L_{ij}} \Delta T_{ij} \quad (2.18)$$

These factors are demonstrated in Figure 17.

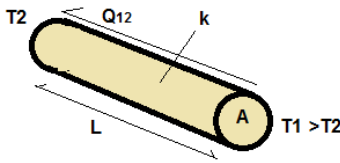


Figure 17: Linear conductive heat transfer between T_1 and T_2

This relation can be used to describe the conductive coupling (C) as [23]:

$$C_{ij} = \frac{kA}{L_{ij}} \quad (2.19)$$

Or from electrical network analogy the thermal resistance is found:

$$R_{ij} = \frac{L_{ij}}{kA} = \frac{1}{C_{ij}} \quad (2.20)$$

And by Kirchhoff's law, multiple resistances in series can be added to find the heat flow through a combination of materials as shown in (Figure 18).

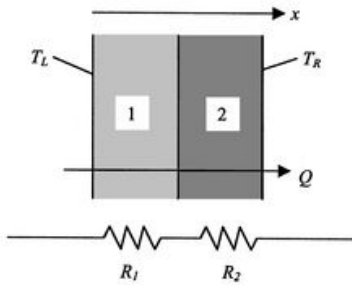


Figure 18: Conductive resistance in series [24]

$$R = R_1 + R_2 = \frac{1}{C_1} + \frac{1}{C_2} \quad (2.21)$$

And similarly, a parallel resistance can be added as demonstrated in Figure 19:

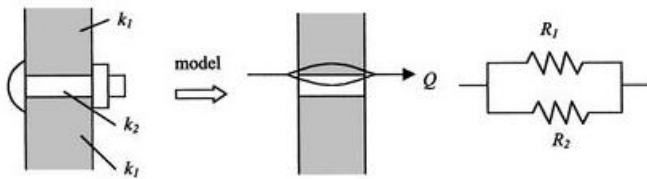


Figure 19: Parallel thermal resistance addition [24]

$$\frac{1}{R} = \frac{1}{R_1} + \frac{1}{R_2} = C_1 + C_2 \quad (2.22)$$

For a cylindrical shell, radial conduction is defined from eq. (2.23) and is shown in Figure 20. Note however that for thin walled tubing $\frac{r_2 - r_1}{r_1} \ll 1$, therefore the heat transfer can be often estimated in the same manner as a slab with thermal path distance [24]; $L_{12} = r_{12} = t_w$.

$$Q_{12} = -kA \frac{dT}{dr} = 2\pi k \frac{T_1 - T_2}{\ln(r_2/r_1)} \quad (2.23)$$

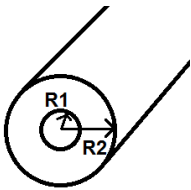


Figure 20: Radial conduction

2.4.5. Convective heat transfer

Convection is the form of heat transfer to which the FR is exposed within the tubing and on the radiator surface. However, the convection which is applicable to the tubing is concerned to forced convection and the convection of the radiator surface is considered to be natural convection.

Heat transfer by convection, can be described by the relation which can be found in any heat transfer literature:

$$Q = h_c A \Delta T \quad (2.24)$$

Some indicative values of heat transfer coefficient h_c can be found in Table 3.

Table 3: Some convective heat transfer coefficients [17]

Nature of flow	Fluid	$h_c \left[\frac{W}{m^2 K} \right]$
Surfaces in buildings	Air	1-5
Across tubes	Gas	10-60
	Liquid	60-600
In tubes	Gas	60-600
	Organic liquid	300-3000
	Water	600-6000
Natural convection	Gas	0.6-600
	Liquid	60-3000

It can be seen that the heat transfer coefficient varies greatly with the medium, state of the medium and the nature of the flow. The flow in the RS is fluidic and the fluid properties are based on Galden HT 55. The mass flow of the system can be adjusted to match the required heat transfer of the system to the environment. Since the medium is being mechanically motorized, the occurring convection is considered to be forced. The outside wall of the FR during the lab tests is considered to be cooled by natural convection.

Convective heat transfer occurs due to a difference between the free stream temperature T_∞ and the surface temperature T_w . The difference causes a thermal boundary layer, which conducts the heat between the wall and the free stream as given in [25] by eq. (2.25)

$$-k_f \left. \frac{\partial T}{\partial y} \right|_{y=0} = h_c (T_w - T_\infty) \quad (2.25)$$

In which k_f is conductivity of the fluid, y is the thermal boundary layer height measured perpendicular to the wall. Arranging this equation as given in [25], which includes the characteristic length of the of the body to which the wall refers.

$$\left. \frac{\partial \left(\frac{T_w - T}{T_w - T_\infty} \right)}{\partial (y/L)} \right|_{y/L=0} = \frac{h_c L}{k_f} = Nu_L \quad (2.26)$$

Which is the definition of the Nusselt number, which is a function of the thickness of the thermal boundary layer. [25]

2.4.5.1. Forced convection

Since the Nusselt number is a function of the boundary layer thickness, the average value is taken in the heat transfer which is performed by the FR. And since the characteristic length of a tube is equal to its inner diameter D_{tube} , we can write eq. (2.26) as

$$\overline{Nu_d} = \frac{\overline{h_c} D_{tube}}{k_f} \quad (2.27)$$

This is considered to be the Nusselt number for a tube flow. In flows, a distinction is made between laminar and turbulent, depending on the Reynolds number Re which is defined as eq. (2.28) [17].

$$Re = \frac{\rho_f v_\infty L}{\mu} \quad (2.28)$$

In which ρ_f defines the fluid density, v_∞ the free stream velocity and μ the dynamic viscosity. The Reynolds numbers in which always a stable laminar flow will occur is $Re \leq 2100$. and turbulent flow is considered always to be complete for $Re > 4 * 10^6$. This however is applicable to a flat plate and for a curved surface is expected that turbulence settles in much earlier. [25]

The Reynolds number of the FR tube is expected to be

$$Re_{tubeflow} = \frac{1650 * 0,26 * 0,00635}{7 * 10^{-4}} = 3,7 * 10^3 \quad (2.29)$$

For the lowest flow velocity expected to occur in the FR, the Reynolds number according to this equation is in the transitional domain, however since the fluid is provided by a mechanical pump, and the flow passes through a narrow connector which almost doubles the Reynolds number due to the increased velocity, the fluid is already expected to be turbulent upon entrance of the tube. [26] discusses that for engineering purposes, fully developed turbulent flow may be assumed considering $\frac{L}{D} > 60$, which is the case if a single fin tube is considered in the FR.

The general relation of the Prandtl number Pr is defined by eq. (2.30), in which C_p is the specific heat capacity of the fluid, which represents the ratio of momentum diffusivity over thermal diffusivity [17]

$$Pr = \frac{\mu_d C_p}{k} \quad (2.30)$$

[26] discusses several correlations for heat transfer in a turbulent flow of a smooth tube, and proposes the Dittus-Boelter correlation for its ease of use with smooth tubes, relating to flows with Prandtl numbers between $0,7 < Pr < 100$ and for tubes with $\frac{L}{D} > 60$:

$$Nu = 0.023 Re_d^{4/5} Pr^z \quad (2.31)$$

Where $z = 0.4$ (for heating) or $z = 0.3$ (cooling). The properties are also determined at the average bulk temperature of the fluid between the entrance and exit of the tube.

According to this approach, the following values in Table 4 are found for forced convective heat transfer in the FR, based on a density of $\rho_{fluid} = 1650 \text{ kg/m}^3$, diameter of $D = 0,00635 \text{ m}$, dynamic viscosity of $\mu_d = 7,3 * 10^{-4} \text{ Pa} \cdot \text{s}$, conductivity of $k_f = 0,065 \frac{\text{W}}{\text{mK}}$ and a specific heat of $C_p = 1240 \frac{\text{J}}{\text{kgK}}$ and an average temperature of $T_{fluid_{av}} = 25 \text{ }^\circ\text{C}$ [27].

Table 4: Heat transfer coefficient for various flow rates

$Q_f \text{ (l/min)}$	0,5	0,8	1	1,2	1,5
$\dot{m} \text{ (kg/s)}$	0,014	0,022	0,028	0,033	0,041
$h_c \left(\frac{\text{W}}{\text{m}^2\text{K}} \right)$	487,7	710,3	849,1	982,4	1174,5

The table shows how the heat transfer may be expected to improve by increasing the flow rate, however may be limited by the conductive coupling of the tube itself, if we regard serial resistance from eq. (2.21)

2.4.6. Natural convection

The surface of the FR is cooled by natural convection, however since the lab environment is equipped with an air conditioning system and since the facility may be entered by people who are working in the lab, the flow of natural convection may be disturbed and may prove to be very difficult to model or predict even by first order. Therefore, the natural convection is correlated in the thermal model, which is based on the conductive properties and radiative properties of the FR and convective properties of the flow, which are relatively certain during steady state.

Originally the Nusselt number which may be used for free convection is a function of the Grashof number (Gr) and Prandtl number, which together form the Rayleigh number (Ra) [28]

$$Nu = C(Gr Ra)^z = C Ra^z \quad (2.32)$$

In which the constants C_{or}, z depend on the orientation of the heated plate. A simplification of this equation for air is produced in [29] which transforms the Nusselt number to the heat transfer coefficient

$$h_c = C_{or} \left(\frac{\Delta T}{L} \right)^z$$

The same source also provides values for C, z . We obtain the following values for a surface with characteristic length $L = 0,4 \text{ m}$ and temperature difference from surface to air $\Delta T = 15^\circ\text{C}$

Table 5: Natural convection heat transfer coefficients for differently oriented surfaces

Orientation	Vertical	Horizontal	Horizontal
Side heated	Both	Top side	Bottom side
C_{or}	1,42	1,32	0,59
z	0,25	0,25	0,25
$h_{c_{nat}}$	3,51	3,27	1,46

This demonstrates that the FR may be expected to be cooled the most if placed vertically. Furthermore, an order of magnitude which may be expected is now known, the air-conditioning system may however still influence this number, which we shall see from the correlation with the model.

2.4.7. Advective coupling

The thermal model makes use of advective couplings to determine the heat transfer between nodes which are connected throughout the flow. The definition of these couplings is given by eq. (2.33) which can be used by measuring the mass flow and the temperature difference.

$$Q_{FR} = \dot{m}_{Gald} C_{pGald} \Delta T_{in-out} \quad (2.33)$$

2.4.8. Radiator efficiency

The fin efficiency is determined to estimate the efficiency of the radiator. An ideal radiator has a constant surface temperature equivalent to its root. In reality the temperature varies over the surface of the radiator as a result of limited conductivity and therefore the possible radiative heat output reduces. Therefore, in its most basic form, the radiator efficiency is the ratio of actual radiated heat over the ideally radiated heat.

$$\eta_e = \frac{Q_{act}}{Q_{ideal}} \quad (2.34)$$

Which may be found from integrating a temperature profile on a surface and dividing it over the ideally radiated heat as demonstrated with (2.35).

$$\eta_e = \frac{\varepsilon \sigma \iint_{A_{tot}} (T^4(x, y) - T_{Space}^4) dA}{A_{tot} \varepsilon \sigma (T_{id}^4 - T_{Space}^4)} \quad (2.35)$$

T_{id} , which is the ideal/root temperature, which is constant throughout the radiator. Close spacing of heat pipes and very thick fins would result in the smallest radiator area and the highest efficiency due to high in plane conduction. However, this would make the design very heavy. Since mass is a critical design driver, a less efficient but lower mass radiator configuration may be preferred. The optimum combination must then be found between heat pipe spacing and fin thickness and so an approach to optimize the fin spacing is given in [30]. However, for the FR design a spacing is chosen and the efficiency shall be determined from the heat which is transferred per node by means of radiation and convection, which can be performed in the thermal model and can be measured during the test. Which boils down to eq. (2.36), which is reduced to eq. (2.34) in the absence of air.

$$\eta_e = \frac{Q_{act_{rad}} + Q_{act_{conv}}}{Q_{ideal_{rad}} + Q_{ideal_{conv}}} \quad (2.36)$$

2.5. Breadboard testing

This section is dedicated to breadboard tests which are conducted to support theory and to develop some understanding of the materials and techniques which are used in the FRA design.

2.5.1. Dyneema creep test

The HDRM utilizes Dyneema thread to close the lever and hold the FRRS with a tight grip. While closed, the HDRM is expected to withstand the launch load of $F = 440\text{ N}$. Since a part of this load is expected on the Dyneema thread, the thread must be placed under pretension, such that the lever remains closed once this load is experienced. This is a significant force, which is placed onto the thread for a long duration of time and may slowly relax the stresses after closing the HDRM. A test of a few days is performed to demonstrate if creep occurs, which would very likely also indicate possible relaxation.

The thread which is tested is a bundle of Dyneema SK75. According to manufacturing sheet [31] one 1760 *dtex* has a breaking force of $F_{br} = 610\text{ N}$ at 3,5 *GPa*. For the combined bundle, assuming that it breaks simultaneously the ultimate load is 6100 N. The elongation at break is 3,5%.

The pre-tensile load which is placed by the HDRM on the thread is $F_{HDRM} = 180\text{ N}$, a test is performed using $F_{mass} = 196\text{ N}$. The load however is suspended over two ends (Figure 21) which are attached to a piece of aluminum with $D = 4\text{ mm}$ holes, similar to those of the HDRM. The bundle ends are individually knotted by means of a single overhand knot. After the test, there have been no observations of damage or plastic deformation in the thread or knot.



Figure 21: Dyneema test thread

Since the stress strain curve is linear for a fiber until it breaks, the required elongation is $\frac{\Delta L}{L} = \frac{98}{6100} * 3,5\% = 0,056\%$. Which is an elongation of $\Delta L = 0,17\text{ mm}$ with respect to the original length of the test. The result of this test is not analyzed due to the complex uncertainties which are involved in this test. However, it is simply demonstrated how the thread responds to a load after a duration of time. The result is that after $t_1 = 67\text{ hrs}$, a slight displacement was measured, however since it is a horizontal displacement, it is assumed that the tape on the needle has released, which can be seen in Figure 22. Therefore, additional Kapton tape is used to tighten the grip on the needle and continue the measurement. After $t_2 = 24\text{ hrs}$ no significant creep is measured as can be seen in Figure 23, taking into account an uncertainty of $\pm 0,2\text{ mm}$.



Figure 22: Creep test observations during various dates and times

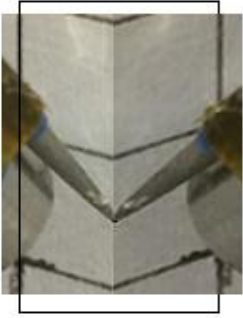


Figure 23: Geometric comparison of needle initial position t_1 (left) and at t_2 (right)

2.5.2. Inflatable breadboard based on a PET/PE tube

Since strong polymer materials are available the option to use thin walls, an inflatable structure is breadboarded to test the inflatability and structural stiffness of a thin walled polymer tube (Figure 24) and to develop some working knowledge on the materials to be used. The material which is used for the inflatable breadboard model is PET/PE foil. The foil is highly flexible and can be easily heat welded using Commercial Off The Shelf (COTS) equipment, into shapes which can be pressurized by air. A tube is produced from this foil, which is tested for bending stiffness and afterwards the tube is inserted into a radiator shape which can be structured by inserting the tube (Figure 24). The tube is simply produced by means of heat welding and the connection with an aluminum hollow rod is made by means of isolation tape and a ty-rop to seal it. Different diameters are tested for bending moment ($D = 6mm, D = 10mm, D = 20mm$), however the $D = 10mm$ only provided results as expected, indicating either unanticipated influence by tube stiffness, a weakness at the root hinge or inaccurate placement of the load attachment points for the other diameters.



Figure 24: Inflated PET/PE heat-welded tube

The tube is bended by means of an Unster which is attached at several locations on the tube, to obtain two predefined bending angles $\phi_1 = 33,33^\circ, \phi_2 = 66,66^\circ$, under different kinds of pressure. This is done to:

- calculate the bending moment for different pressures
- calculate the difference in bending moment due to a longer moment arm to obtain a constant deflection

The latter may be influenced by the elasticity of the straight part of the tube, or due to a slight curvature which causes less wrinkles at the root, leading to a lower bending moment. The accuracy of this test is approximated to be $\Delta M =$

$$\pm\sqrt{(0,005m)^2 + (0,01N)^2} = 0,01Nm$$

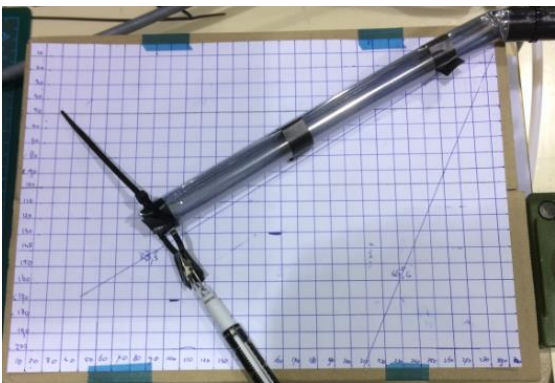


Figure 25: Bending test setup

The bending moment M_w of a foil tube which is expected is based on the approximations provided by [33], which describes the moment which is related to the formation of the first wrinkles at root of the tube with pressure P and initial tube radius R_o

$$M_w = P\pi R_o^3/2 \quad (2.37)$$

and the moment related to the complete circumferential wrinkling at the root or collapse moment:

$$M_c = 2M_w = P\pi R_o^3 \quad (2.38)$$

Furthermore, [34] proposes the equation for total bending moment as a function of pressure, including the stiffness of the tube wall

$$M_{press} = \pi R_o E t h^2 (0,6\gamma + \Delta\gamma) + 0,8P\pi R_o^3 \quad (2.39)$$

In which E is the Youngs modulus of the tube, th is the wall thickness and the 0,8 factor is chosen for design purposes [34]. γ and $\Delta\gamma$ are buckling constants which are also obtained from [34]. The tube bending test results are shown in Appendix A: Inflated tube bending test results.

It is observed that the bending moments which are produced by the shortest moment arms, almost exactly comply with the expected collapse bending moment from eq. (2.38). Moments generated with longer arms tend to reduce with increasing arm length. This may indicate that the tube is less wrinkled at the root. Furthermore, it is observed that the deflections which are made to comply with ϕ_1 produce approximately 10 – 30% lower moments than the values which are obtained from ϕ_2 . This may also indicate less wrinkly behavior at the root of the tube. Therefore, for the design of the radiator, a margin should be taken into account to compensate for these losses in terms of bending. However, depending on the materials used, the radiator also may be stiffer than expected by eq. (2.38). Therefore (2.39) should be used for determining the actual bending moment of the FR after deployment. During deployment eq. (2.38) may be used as the moment arm is shorter.

After observing the bending moments which can be carried by the tube, a PET/PE dummy radiator is heat welded around the tube. The dimensions of the dummy radiator are $LxB = 0,4x1 m^2$ and can be seen in Figure 26. The tube is made from a double sheet of PET/PE which is welded into a U shape on the entire circumference to produce a continuous tube. It is also closed on one side and pressurized on the other.



Figure 26: FR breadboard model made from PET/PE and pressurized with air at one bar pressure gauge

The figure demonstrates a stiff result; however, the dummy radiator only remains in this stretched position for a couple of seconds. The failure mode is assumed to be buckling due to instability. The far end of the dummy slightly moves sideways until it starts buckling. This instability is proposed to be the result of lateral torsional buckling. After calculating the required diameter of tubing to uphold the FR in this position as function of liquid mass, it seems unrealistic to demonstrate the FR in this position. A test to deploy the dummy from a rolled-up position furthermore demonstrated that the dummy would fall down and afterwards would not recover only by means of pressure. Therefore, other means of deployment of the dummy are considered, and also the analysis of the lateral torsional buckling is left out of this Thesis.

At this stage supportive mechanisms are not yet considered. Purely basic means of unrolling the dummy are first considered for the verification of the requirements.

Therefore, the option of restraining several axes to demonstrate its deployment characteristics is tested. Figure 27 demonstrates how the dummy deploys by means of pressurized air. The flat surface test demonstrates that $P_{gauge} = 1 \text{ bar}$ is sufficient to roll-off the low mass dummy radiator. Furthermore, the tube is rolled up and placed on its side to demonstrate how it unrolls from a top view in two dimensions. It demonstrates that the rolled-up tube is launched forwards and does not make a huge swoop. Therefore, it is considered that these tests may be used to fulfill the requirements, by adding additional mass which is representative for the FR/FRRS.

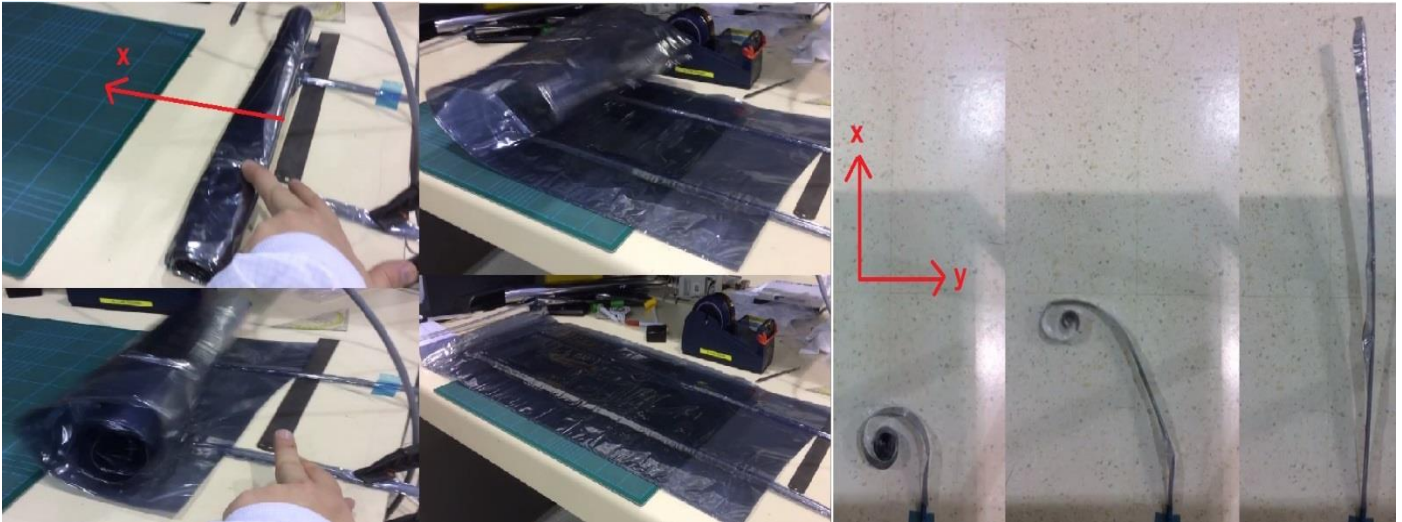


Figure 27: Simplified deployment tests: roll-off on a flat surface (left), sideways inflation of single tube (right)

2.5.3. Capstan equation

The Capstan equation is used to determine the tensile load which is present in the cross section of the FR as a function of windings around the FRRS. In particular it is used to determine the load which acts on the connection to the FRRS at the end of the FR. A Capstan can also be found on board of ships as it utilizes the friction which is present between the rope and the Capstan to greatly reduce the required force by the handler to hold heavy sails.

The equation is found in [35]. It relates the friction coefficient μ_{fric} of the rope and the number of windings β expressed in radians to the tensile forces in the rope (F_1, F_2). Assumed is that the FR is slipping, since it cannot be rolled up without some minor slack.

$$F_1 = F_2 e^{\mu_{fric} \beta} \quad (2.40)$$

If we consider that the launch load pulls on the FR laminate end which is held by the FRF. The tensile force within the cross section of the FR exponentially decreases with the number of windings around the FRRS. For a kinetic friction coefficient of Kapton [36] $\mu_{fric} = 0,48$, assuming that the full launch load is exerted on the FR, it is found that the tensile force F_2 in the FR laminate reduces to practically zero over the course of one winding due to the high friction coefficient. Therefore, it is assumed that the load which acts on the connection of the FR to the FRRS should be analyzed on handling rather than operational loads.

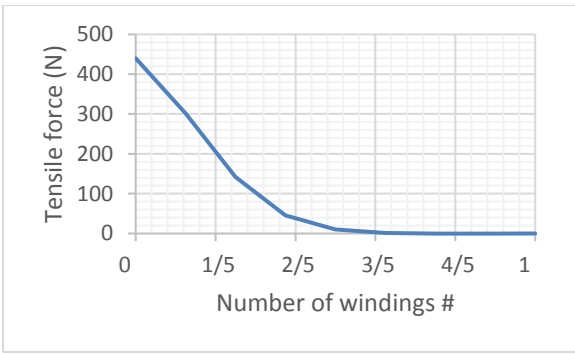


Figure 28: The reduction of tensile force within the FR as a result of friction forces while wounded around the FRRS

2.5.4. Roll up equation

As said before, the foil which is rolled up tightly around the FRRS may be rolled up and then slip slightly when placed into position with the HDRM. The foil + tube thickness (compressed and uncompressed) is between $0,35 \text{ mm}$ and $6,7 \text{ mm}$. The amount of length required to complete a number (n) of windings around the FRRS with radius $R_{in} = 37 \text{ mm}$ can be found by means of:

$$L_{req} = 2\pi \sum_{k=1}^n \left(R_{in} + \frac{th_{foil}}{2}(2k - 1) \right) \quad (2.41)$$

To complete 5 whole windings, $L_{req} = 1190 \text{ mm}$. Therefore with length $L = 1000 \text{ mm}$ and $th_{foil} = 0,35 \text{ mm}$ we can complete $N_{wind} = 5 * \frac{L}{L_{req}} = 4,2 \text{ windings}$ and for $th_{foil} = 6,7 \text{ mm}$ we aim for four windings and thus complete $N_{wind} = 4 * \frac{1000}{1267} = 3,15 \text{ windings}$.

The outer radius that is achieved by rolling up the foil is:

$$R_{out_{tight}} = R_{in} + N_{wind} * th_{foil_{min}} = 38,05 \text{ mm} \quad (2.42)$$

$$R_{out_{loose}} = R_{in} + N_{wind} * th_{foil_{max}} = 63,8 \text{ mm} \quad (2.43)$$

This demonstrates that the possible number of windings will be high enough to deal with the launch load, but also that the resulting roll thickness is relatively low $th_{roll} = R_{out} - R_{in}$; $1 \text{ mm} < th_{roll} < 26,8 \text{ mm}$ for a length of 1 m . It is however highly related to the tightness of the roll.

2.5.5. Mechanical, handling and thermal testing of applicable materials

To obtain an understanding of the physical and thermal properties of the materials which are likely to be used for the breadboard model, a number of tests are performed which shall be summarized in this section. The tests are performed on a foil of aluminized Kapton which holds six samples which are made from different stacks of PGS and different OSR configurations and sizes (Figure 29).



Figure 29: Bending test item

The entire foil was bended over a $D = 90 \text{ mm}$ diameter beam under various angles and different masses were applied to tests to see if the materials would break or peel off. The result was that the stacks of PGS seemed very flexible and durable as no visible change had occurred, however the OSR did show cracks on each surface except for the surfaces which were smaller than 1 cm^2 . This opens up the option to cover the FR in OSR's however a specific adhesive and a manufacturing method must be investigated for this purpose.

Furthermore, it is learned that PGS is very fragile and the pressure sensitive tape is difficult to use without generating bubbles in the laminate. This should be taken into account while assembling the FR. Furthermore, it is noticed that PGS becomes relatively stiff after placing more than two layers on top of each other. Therefore, it is not investigated if more PGS should be used for the FR to improve the conductive performance.

2.6. GEO Environment

Spacecraft in GEO are exposed to several environmental factors. Materials which are used for FR may be damaged by impacting MMOD but also material properties may change as a result of interactions with the environment. The most important factors for the lifetime of the FR considered that it operates in GEO are radiation, which may reduce the material strength or the optical properties of the surface or charge the surface which may lead to a static discharge which damages the material, and MMOD, which may penetrate the FR wall and cause punctures or delamination's. Finally, there is thermal cycling which cause stresses in and between the materials due to thermal expansion and outgassing due to exposure to vacuum, however these are not considered to be in the scope of this report and thus require more research before defining or verifying any requirement. The permeability of Kapton is something which must be investigated for the specific fluid of use, due to the long molecular chain of Galden, it is not expected at this point that the permeability of Kapton will be an issue for the design.

2.6.1. MMOD

MMOD is a combination of Space debris and micrometeoroids. In LEO, the probability of an impact is higher due to the presence of debris, which is shown in Figure 30. However, for GEO, debris is less prominently present and therefore a collision is expected to occur with micrometeoroids. The dominant mass and diameter of these particles is found to be $D \sim 200 \mu\text{m}$ and with mass of $m \sim 1,5 * 10^{-5} \text{ g}$, and these can reach impact velocities of $v_{imp} = 72 \text{ km/s}$ [37].

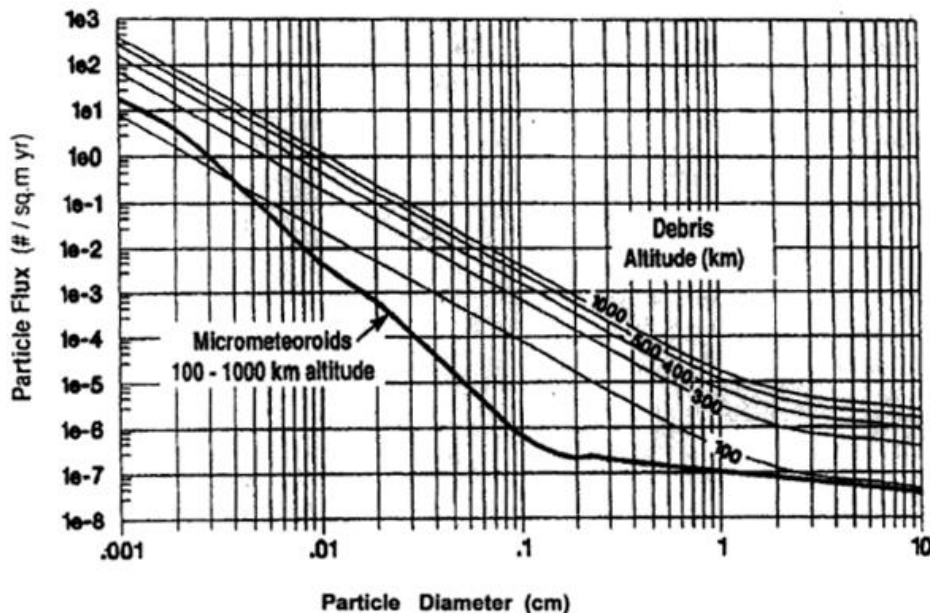


Figure 30: LEO particles [38]

Meteoroids are considered to be less harmful for Spacecraft, due to their small size and mass, despite of their large mean velocities, however they can cause punctures, or degradation of polymer surfaces [38]. Furthermore, the dominant part of meteoroid environment can be assumed sporadic and invariant with time [39]. Debris however, is constantly catalogued and an increase in fragmentation debris is observed in [40] over the last few years.

The following software and sources can be used to calculate MMOD and debris fluxes which help to determine MMOD risks for the FR: MASTER, DRAMA. These can be downloaded on the ESA website [41]. [37] has used MASTER-2001 database to obtain the following mean times between collisions of various sizes on a $A_{sphere} = 1 m^2$ spherical target (Table 6). It can be noted that in low earth orbit, the time between impacts is relatively low, which is explained before to be caused by the debris population.

Table 6: Time between collisions with particle sizes on a $1 m^2$ spherical surface modeled by master-2001 [37]

Orbit (semi-major axis)	$d > 0.0001 m$	$d > 0.001 m$	$d > 0.01 m$	$d > 0.1 m$
ISS ($\approx 360 km$)	221 d	271 y	149,253 y	$1.872 \times 10^6 y$
GPS (20,000 km)	4.52 y	10,090 y	$11,2 \times 10^6 y$	$990 \times 10^6 y$
GEO (35,786 km)	4.67 y	2,267 y	$2.44 \times 10^6 y$	$24.6 \times 10^6 y$

2.6.2. Radiation

Another risk for the thin walled FR is radiation. Thin walled materials are known to degrade due to radiation. Not only mechanical but also optical properties may be affected. The main radiation particles of concern in GEO are considered to be Solar wind particles, High Energy Protons and High Energy Electrons [38]. Electrons however penetrate deeper into the material. An overview of concentrations related to altitude can be seen in Figure 31.

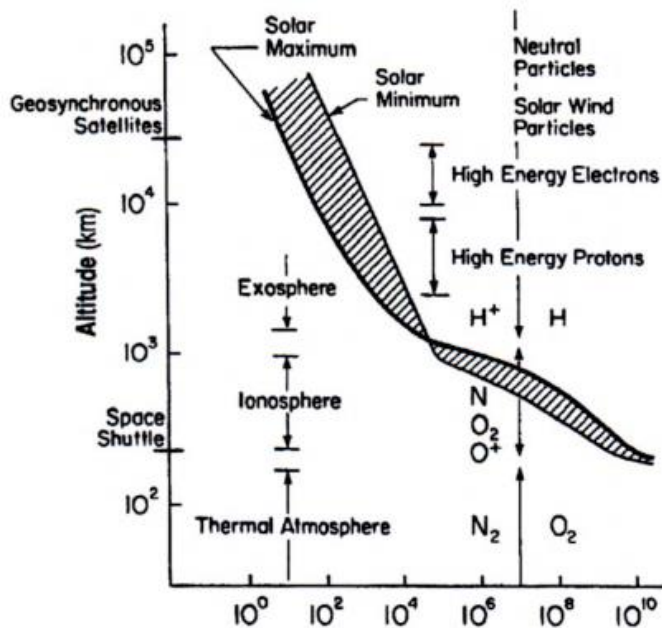


Figure 31: Concentration of radiation particles and gaseous species as function of altitude [38]

Solar flare protons and electrons however are considered negligible for inflatable designs and the significant protons and electrons are geomagnetically trapped and plasma/auroral particles [38]. Typical daily fluences for GEO are $4,94 \times 10^{12} \text{ Electrons/day/cm}^2$ and $1,87 \times 10^{12} \text{ Protons/day/cm}^2$. Predictions are provided in [38] concerning 5 years in GEO which related to proton and electron doses and their penetration depth for Kapton. Kapton is relatively well resistant to radiation and it is expected that mild to moderate damage may occur starting from a dose of 300 MRad . The expected depth to obtain this dose in 5 years' time by means of electrons is determined by means of AE8 MAX to be $0,9 \text{ mils} = 22,9 \mu\text{m}$ [38]. Protons by AP8 MIN model are expected to deliver this dose to a depth of $0,1 \text{ mils} = 2,5 \mu\text{m}$. Where Min and Max relate to the worst case solar activity conditions [38]. This shows that electrons pose a greater threat to the FR than protons. If we consider a lifetime of 15 years in space, the dose at 1 mil depth may become larger than the 300 MRad threshold. The models are however discussed in [38] to be inaccurate and or deficient for lower particle energies. It is demonstrated that by adding the low energy plasma electrons dose from the ATS-6 model, that the dose in 5 years' time may reach 1000 MRad at 1 mil depth and is much higher at the surface of the foil. A combination of electron dose-depth is also provided in [38] to simulate a modelled dose of 5 years in GEO.

However, since the material is not expected to sustain more than mild-to-moderate damage until it reaches a dose of 4000 MRad [38], and since the external materials are not critically loaded it is assumed that the HiPeR laminate will not sustain critical damage during 15 years in orbit. [38] also shows that the dose quickly reduces when approaching the 1 mil depth. Therefore, it is assumed that the complete laminate, which is much thicker and exists at least of 2 mil Kapton, will be sufficient to protect the adhesive and the tubing from mechanical degradation as a result of radiation.

It was found in [42] by means of AE8 and AP8 that the total dose reaching 1 mil during 15 years a simulated GEO environment is $\approx 8 * 10^5 \text{ Gy} = 800 \text{ MRad}$. A radiation test was conducted simulating equivalent dose/depth applied by electron and proton particles as shown in Figure 32. Furthermore 8897 Equivalent Sun Hours (ESH) of UV radiation was applied with solar constants varying between 7 and 9. The radiation was applied to a 5 mil specimen of Kapton, which hardly showed any mechanical degradation as it reduces $\approx 1\%$ in ultimate tensile strength and $\approx 20\%$ in Ultimate strain and is therefore practically unaffected by the radiation.

This is expected from a thicker layer of Kapton but it does not exclude that the FR surface will be damaged since the laminate is thinner. It is still fair to assume at this point that the tubing will not be critically damaged since it is shielded by HiPeR and HiPeR is already qualified to deal with radiation.

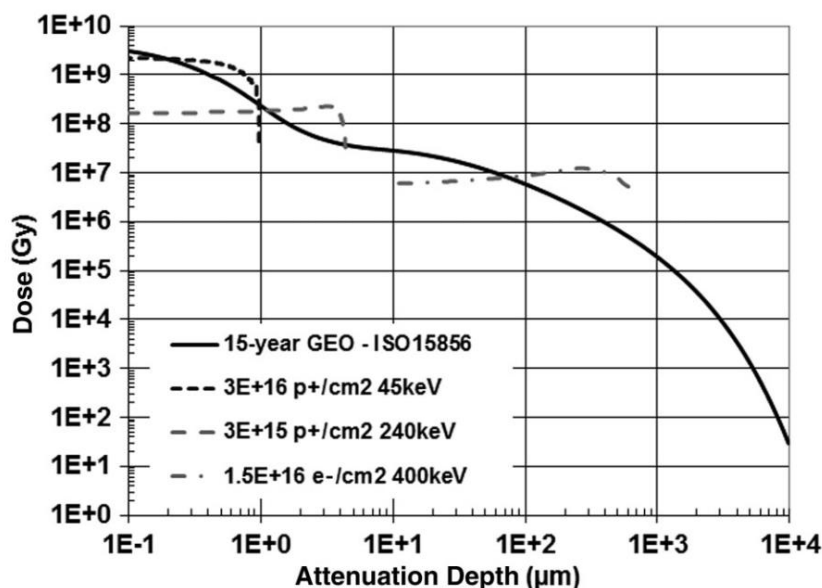


Figure 32: 15 year dose in GEO-equivalent particle environment [42]

2.7. Research questions elaborated

The research questions are shortly elaborated per question.

RQ 2.1: “What is INFRA and how can this graduation research work contribute to the INFRA project?”

A: INFRA is a project in which Airbus and the NLR are cooperating to develop a radiator system that combines their specialized technologies. This goal of this research project is to develop a subsystem for the radiator system and demonstrate its functionality. Furthermore, the research project is used to develop a thermal model or a MMOD analysis, which can be used to obtain a better understanding of the product.

RQ 2.2: “How to utilize HiPeR within INFRA and what is the state of the art?”

A: The state of the art of inflatables is based on rigidizing techniques, since INFRA is stiffened by means of pressure, rigidizing is not considered. Extensive research was conducted into similar concepts, however these all failed within a month time in space due to MMOD. HiPeR is expected to provide a longer lifetime besides a high performance to mass ratio and is therefore considered state of the art in inflatable and flexible radiators.

RQ 2.3: “Which thermal theory is applicable to the design and verification of the FR?”

A: The theory which is described in the Thermal section is theory which is used in determining the performance of the FR by means of first order approximations as well as by means of the thermal mathematical model.

RQ 2.4: “Which tests are required to obtain some working knowledge on the functionality of the FRA?”

A: The design is supported by means of breadboard tests in this case is more effective than analysis. Initially material tests were performed to better understand the HiPeR materials. Creep and melting tests were performed to better predict the behavior of Dyneema in the design. A PET/PE version of the FR also provided insights in the deployment mechanisms, inflatability and stiffness of the design.

RQ 2.4: “Which environments are to be considered for the design of the breadboard model and how will these environments impact the design choices?”

A: The environments which are considered are the Lab in which the tests take place and an ideal space environment of $T = 2,7 K$ and no additional heat sources, which will be used to predict the performance of the FR. For the Lab tests tooling is developed to hold the FRA during the thermal and deployment tests and for the space environment no additional tooling is required. A FRF is designed such that it can be integrated with or replaced by a S/C wall. Furthermore, the space environment requires an estimation of lifetime due to MMOD and also a prediction based on radiation.

3 INFRA Requirements

The development of the INFRA project is based on the system requirements. The system requirements are used in this project as a translation of the customer requirements and contributing rules or boundaries to help define the characteristics of the system. To define these requirements a House Of Quality (HOQ) was used at an early stage to define the most important characteristics of the system with respect to the customer requirements. Furthermore, a system context diagram was formulated and an input-output matrix was helpful to identify underlying requirements. The process of developing the breadboard is based on the well-known systems engineering 'V-model', which can be seen in Figure 33. The requirements and the design are defined and synthesized in the order as displayed by the arrows. And the reports which are delivered for the project are shown in the blue boxes. The results of the verification and validation resulting from this process are found in chapter 5.3.4.

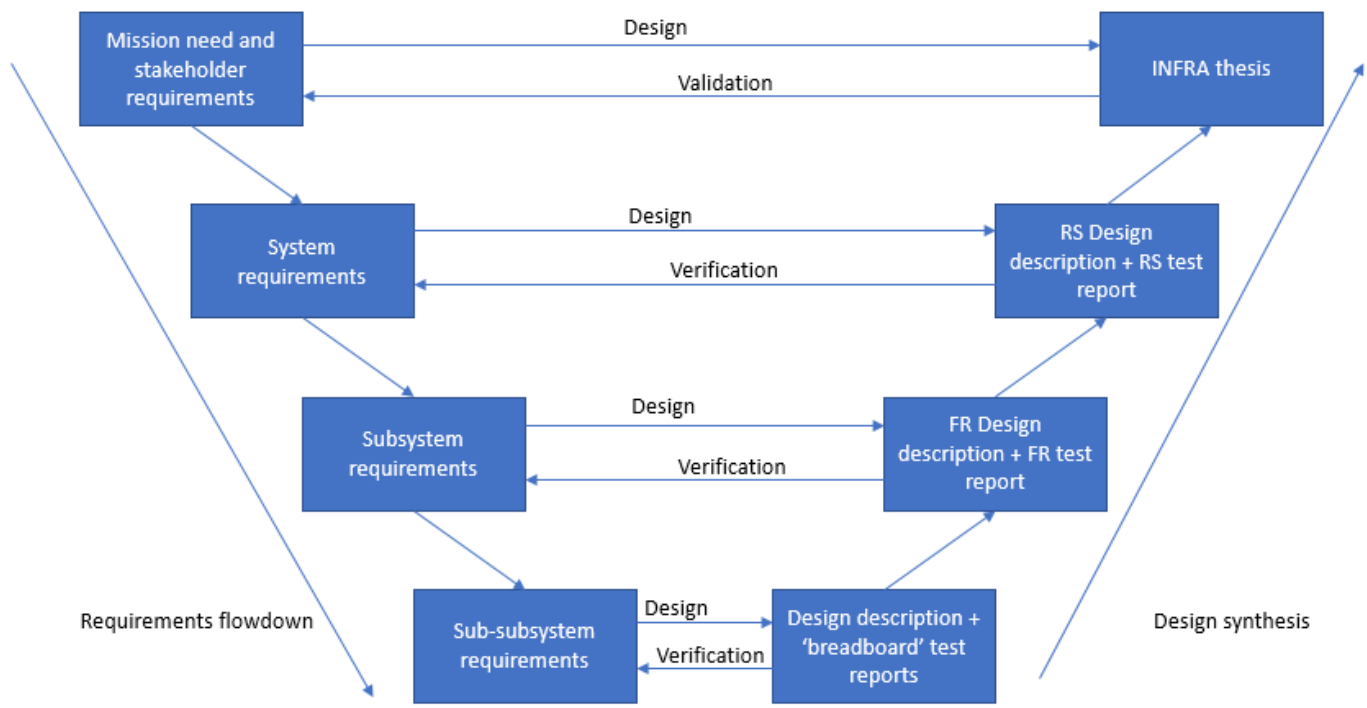


Figure 33: INFRA V-Model

This chapter shall provide the results of the techniques which were used as well as the resulting requirements and the lessons learned throughout the process.

Need and mission statement

For this project, the need is: *“To develop a breadboard (BB) model, that is tested for heat dissipation and deployment, to deliver a proof of concept of Inflatable Radiator (INFRA) technology, which combines High-Performance Radiator (HiPeR) with the Micro- Mechanically Pumped Loop (μ-MPL) technology, and which demonstrates competitive potential with respect to the state of the art, in terms of heat dissipation, stowed volume and mass.”*

The INFRA concept is identified for its potential on the deployable radiator market, amongst other things due to its low mass and low storage volume requirements. Therefore, the breadboard model is also used to verify these expectations.

The mission statement is hereafter formulated as: *“The INFRA project shall design, develop and test an Inflatable Radiator BB that can serve as proof of concept of Inflatable radiator technology, which utilizes HiPeR and μMPL technology, which can demonstrate deployment functionality and also demonstrates potential in terms of mass, stowed volume and heat dissipation.”*

3.1. Stakeholder requirements

The NLR & Airbus project members function as the key and active stakeholders since they cooperate and participate directly within the project group, and as a company the NLR and Airbus shall benefit passively from the long-term results. Individuals such as the Assembly Integration and Testing (AIT) engineers, are considered to be active stakeholders and therefore their interaction with the system is also taken into account. For the stakeholders, the key-requirements are identified in coordination with the customer expectations and are presented including the weights in Table 7.

Table 7: Key- Customer Requirements

Requirement	Weight
Competitiveness	8
Cost	7
Lifetime	8
Mass	6
Manufacturability / handling	8
Presentation	7
Radiator efficiency	6
Safety	4
Scalability	8
Technology demonstration	10

After defining the key customer requirements, the original INFRA proposal, together with a series of first order approximations related to the high-level design is used to identify a list of system characteristics. These are rated for importance in a House of Quality matrix and this matrix shows that the following system characteristics or functional requirements which are the most important for the success of the product are: the radiation resistance, flexibility of the radiator, ability to sustain internal overpressure, deployed stiffness, leak tightness, flow rate and conductivity in-plane. At this stage Micro Meteorites and Orbital Debris (MMOD) are not considered to be an issue and mitigation of risk by means of redundancy is considered to be sufficient to obtain a nominal lifetime in orbit, only while verifying the RS design lifetime a more detailed analysis is performed and it is discovered that the lifetime is indeed highly impacted by this factor (see chapter 4.4) Instead the requirements regarding to lifetime at this stage, are based on radiation, since previous classified HiPeR tests by Airbus have shown that high dose of Gamma radiation tests can be destructive on the polymers which are considered for this technology, however Kapton tests showed to be almost unaffected by a 15 years electron/ proton dose. It is further discussed in chapter 2.6. As can be read in the mission statement, the goal is to produce a system which can be tested to demonstrate and deliver proof of the INFRA technology and which demonstrates potential in the deployable radiator market. The focus of this project therefore is to produce a system which functions and which can verify the main requirements. It is considered acceptable by the clients to postpone the product lifetime developments relating to MMOD. In the following section the system requirements shall be elaborated.

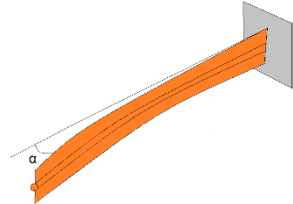
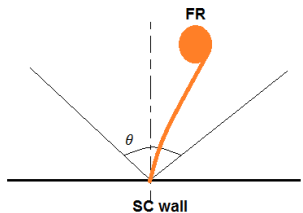
3.2. System requirements

The initial requirements which are directly obtained from the original INFRA proposal, are shown in Table 9. Included in this table are also refined requirements which are used in the System Requirements document, these are derived from the proposal and based on first order approximations and/or customer requirements which have been translated to systems level requirements. The requirements refer to Use Cases (UC), which are defined as UC 1; Representative deployment test, UC 2; Representative bending test, UC 3: Representative thermal balance test. These tests are divided in scenarios which are indicated as UCS, however these shall not be elaborated in this report. Note that not all the requirements are elaborated in this report to maintain a focus on the most fundamental aspects of the project. Requirements which are related to handling or detailed structural requirements for example. The verification methods are shown in Table 8 and are referring to Testing, Analysis, Review of Design (RoD) and inspection.

Table 8: Requirement verification methods

Method	Definition
Testing	Product performance or function measuring under simulated circumstances to verify compliance
Analysis	Engineering analysis, qualitative analysis, and/or computer modelling to verify compliance
RoD	Verification during an official Design Review meeting
Inspection	Visual evaluation of item and associated documentation to verify compliance

Table 9: System Requirements

Requirement ID	Requirement specification	Method
INFRA-prop-0002	Following a single (set of) commands, the INFRA BB shall manage the transition from stowed to deployed condition. This is a one-off operation, re-stow is not foreseen. Manual re-stows should be possible without degrading the hardware	-
INFRA-prop-0003	The RS shall exist out of the following elements: <ul style="list-style-type: none"> - A system to transport heat from the Payload i/f to the radiator panel - A system to initiate deployment - A system to maintain deployment - A flexible radiator panel with a suitable optical surface - A hold-down mechanism - Above functions should be combined - A payload capable of dissipating 400 W 	-
INFRA-prop-0005	The FR shall demonstrate a heat rejection performance of $> 588 W/m^2$ (refined by INFRA-BB-SR-5.2.6.2)	-
INFRA-prop-0006	The RS shall demonstrate a mass performance of $m_{RS}/Q_{outFR} < 10 kg/kW$	-
INFRA-prop-0018	The surfaces of the RS exposed to space, shall be able to sustain $-100 °C < T < 100 °C$	-
INFRA-prop-0024	The FR shall be able to withstand a typical radiation dose corresponding to $T_{oper} = 15 years$ in orbit (Refined in INFRA-BB-SR-5.2.5.4)	RoD
INFRA-prop-0027	The radiator surface area shall be $A_{FR} = 0,4 m^2$ (refined in INFRA-BB-SR-5.2.2.2)	-
INFRA-prop-0031	Pump selection shall be based on the system working point e.g. pressure head vs. flow rate	-
INFRA-prop-0032	The system working point shall be related to tube length and diameter	-
INFRA-BB-SR-5.2.1.4	The parts in fluid contact shall be chemically resistant to Galden HT and Ammonia	RoD
INFRA-BB-SR-5.2.1.10	The FR shall be considered deployed once a steady state at $P_{abs} > 1,5 bar$ internal system pressure is reached and also a deflection angle $\alpha < 30 °$ of the tubing is obtained	T
		
INFRA-BB-SR-5.2.2.1	The RS shall dissipate the heat loads without exceeding the max root temperature of $T_{rootmax} = 50 °C$, as measured on the wall of the tube at the fluid entrance of the FR	A,T
INFRA-BB-SR-5.2.2.2	The radiator surface area shall be $A_{FRsurface} = 0,8 m^2$	RoD
INFRA-BB-SR-5.2.2.3	Every component or material in the RS shall be able to sustain payload temperatures to be expected in space ranging from $-20 ± 5 < T < 65 ± 5 °C$	RoD
INFRA-BB-SR-5.2.3.1	The PA shall operate a fluid volume flow of $Q_f = 1 ± 0,1 l/min$	T
INFRA-BB-SR-5.2.3.4	The PA shall operate a maximum absolute system pressure (MOP) of $P_{abs} = 3 ± 0,3 bar$	RoD
INFRA-BB-SR-5.2.5.4	The FR tubing material shall sustain no more than mild to medium damage due to a Gamma radiation dose of 400 MRad	RoD
INFRA-BB-SR-5.2.6.2	The FR shall demonstrate an overall radiator efficiency of $\eta = 50 ± 10 %$	A
INFRA-BB-SR-5.2.7.1	The bending stiffness of the radiator cross section shall be low enough such that the FR can be stowed and inflated with a stowed volume of $V_{FRstow} = 0,016 m^3$	T
INFRA-BB-SR-5.2.7.2	The FR shall not deflect more than $\delta = 0,5 m$ during UC2	T
INFRA-BB-SR-5.2.7.4	The FR tubing shall be able to sustain max system pressure taking a safety factor of $s_f = 1.5$ into account during tests	A
INFRA-BB-SR-5.2.7.5	The FR shall deploy within $2\theta = 90 °$ cone from the rolled up/stowed starting position:	T
		

INFRA-BB-SR-5.2.7.6	The FR materials shall not deflect or deform when operating at $T = 65 \pm 5^\circ C$	RoD
INFRA-BB-SR-5.2.7.7	The FR, FRRS, FRF & HDRM shall be able to sustain static loads originating from the radiator ($m_{FR+FRRS} = 1kg$) in any direction during launch accelerations of $a = 30 g$, leading to main launch load ($F_{launch} = 440N$)	A
INFRA-BB-SR-5.2.7.10	A single HDRM shall be able to sustain a Load of $F = 100N$ originating from the center on the FRRS aiming in any direction	A
INFRA-BB-SR-5.2.9.2	The HDRM shall have both an electrical deployment mechanism and a mechanical deployment mechanism that can be used individually	RoD
INFRA-BB-SR-5.2.9.3	The electrical HDRM shall be able to release the stowed foil within $t = 2min$ after initiation	T

In the following section, some of the system specifications shall be shortly elaborated.

3.2.1. Requirement specification

Most of the specifications are straightforward; however, several requirements require some additional elaboration. The [INFRA-BB-SR-5.2.2.2] requirement is used to offer a benchmark to which the PA and FR performance could be coupled. The area is determined by first order estimations relating to the length which could be sustained and the width depends on the HiPeR fin efficiency. [INFRA-BB-SR-5.2.5.4] refers as a guideline for radiation dose which is provided to the tubing by electron particles, assuming the HiPeR laminate stops the low energy plasma electrons, however not the high energy electron particles. This is specified for the tubing since the mechanical properties must not be affected by radiation to be able to continue to sustain pressure. [INFRA-BB-SR-5.2.6.2] is defined to set a minimal efficiency of the FR, demonstrating the minimal mass required to operate a predefined surface. Furthermore, this efficiency requirement is less dependent on operating temperature, where the previous requirement could only be met with high fluid temperatures, which are less stable in a lab environment. The [INFRA-BB-SR-5.2.7.5] requirement is installed to provide an acceptable and achievable breadboard boundary for the deployment of the FR. The goal is to further reduce the deployment area during the development of the product. [INFRA-BB-SR-5.2.7.6] relates to the actual maximum payload temperature in space. [INFRA-BB-SR-5.2.7.10] is a rough estimate of deployment force due to spring and pressure which is experienced after a single HDRM release, incorporated is a factor to account for accidental handling loads. [INFRA-BB-SR-5.2.9.2] is used to make sure that the HDRM can be used efficiently during recurring tests. [INFRA-BB-SR-5.2.9.3] is defined with a margin after demonstrating the cutting time of Dyneema thread by means of COTS resistors at their rated power. Relating to the refinement of the requirements of the original proposal the [INFRA-prop-0006] requirement is changed to a mass performance of the FRA instead of the RS and the [INFRA-prop-0005] requirement, relating to the heat output is changed to a fin efficiency, which is less temperature dependent. Furthermore, [INFRA-prop-0031] and [INFRA-prop-0032] relating to the working point of the system depend on the tube size and length as the pressure drops more rapidly due to increase in velocity and friction over a long and narrow tube, and thus increases the heat transfer rate from the fluid to the radiator as the heat transfer coefficient increases. Since the micro pumps are only able to provide a limited amount of pressure head, the amount of heat transfer is quickly reduced by increasing the tube diameter. On the contrary, increasing the tube diameter also provides the FR with increased deployment force and increased stiffness, which is useful for stability and bending of the FR during maneuvers. Therefore, a requirement is added which limits the allowable deflection of the FR, which is expected to occur during a critical maneuver. The minimal tube diameter is increased and as a result [INFRA-BB-SR-5.2.3.1] is refined.

The following torque maneuver is suggested as critical for the INFRA radiator. The maneuver is based on a conservative and imaginary scenario using four reaction thrusters each able to provide $F_{th} = 20 N$. The thrusters together create a torque around the pitch axis of the S/C of $120 Nm$, which has a moment of inertia of $I_{sc} = 3500 kg m^2$, which would correspond to a solid square cube of sides $s = 2 m$, and s/c mass $m_{sc} = 5250 kg$, which according to a space enthusiast website, is in the range of the 'older' Eurostar E3000 series [43]. These values however are slightly conservative since the modern-day communication satellites are often of a lower mass as they operate electric propulsion, but which also typically generate (much) less thrust force than the bio-propellant thrusters during these maneuvers. Furthermore, the maneuver is typically performed using only half of the available thrusters. Adding a safety factor of 1,5 to the equation provides a very conservative load case. Note however that scaling does affect the moment on the base of the FR during these maneuvers as well as the natural frequency is also affected by increasing the size. The maneuver setup can be seen in Figure 3.

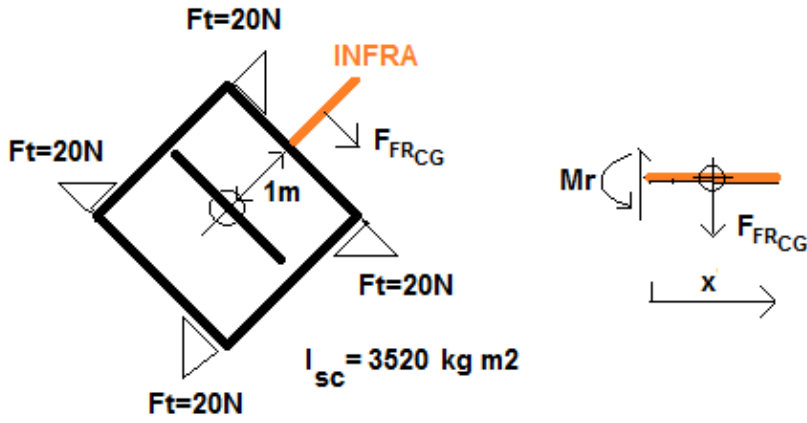


Figure 34: Torque maneuver causes bending moment on the base of the FR

As the main body is being rotated around its center of gravity, INFRA experiences a moment on its root as a result of the angular acceleration a_{ang} of the S/C. From newtons second law, we know that:

$$\tau = I_{sc}a \text{ [Nm]}$$

And thus, after rewriting and including a safety factor of $s_f = 1,5$ we obtain:

$$a_{ang} = \frac{\tau s_f}{I_{sc}} = \frac{120 * 1,5}{3500} = 0,0514 \left[\frac{rad}{s^2} \right]$$

And to determine the tangential acceleration a_{tan} which is experienced locally, we multiply with the radius of the location of the object r_{obj} .

$$a_{tan} = r_{obj} a_{ang} \left[\frac{m}{s^2} \right]$$

Since the local acceleration is a function of radius, we can use the center of gravity of the FR and the FRRS to determine the force F_{FRCG} F_{FRRSCG} which will be acting on the center of gravity. The Local force is based on the FR + tubing and the FRRS. The forces which are locally present due to the radius from the center of the S/C are:

$$F_{FRcg} = a_{tan} m_{FR} = 1,5 * 0,05 * 0,26 = 0,02 \text{ [N]}$$

$$F_{FRRSCg} = a_{tan} m_{FRRS} = 2 * 0,05 * 0,55 = 0,06 \text{ [N]}$$

The resulting reaction moment, where $r_{FR_{root-FRcg}} = 0,5 \text{ m}$ and $r_{FR_{root-FRRSCg}} = 1 \text{ m}$ is:

$$M_r = r_{FR_{root-FRcg}} F_{FRcg} + r_{FR_{root-FRRSCg}} F_{FRRSCg} = 0,07 \text{ Nm}$$

The required stiffness k_{FR} , which is known from Hooke's law to be related to load and displacement, is then obtained from the allowable deflection x_{all} [INFRA-BB-SR-5.2.7.2]. During this test a point load at $x_F = 1 \text{ m}$ is applied to obtain a deflection. The point load corresponds to the reaction moment M_r and therefore the required stiffness of the FR is:

$$k_{FR} = \frac{M_r}{x_{all}} = \frac{0,07}{0,5} = 0,14 \left[\frac{N}{m} \right]$$

The allowable deflection also includes a limitation on buckling of the FR. In case this loading condition is applied, the base of the FR shall not buckle.

3.3. Research question elaboration and conclusion

RQ 3.1: "Who are the main stakeholders, what are their needs and requirements and how will these influence the system requirements?"

A: The main stakeholders are the customers which are Airbus and the NLR. Their needs are to develop a FR as part of a RS which combines their latest pump and radiator technologies and which satisfies the product potential

RQ 3.2: "What are proper system requirements for the INFRA breadboard model that reflect the customer requirements and in what manner can these be verified?"

A: The system requirements which are developed, relate to system characteristics which are satisfying for the customers. The main goal is to demonstrate a technology and to demonstrate a certain performance by means of a simple design. The requirements are set-up to facilitate this and control the required characteristics. These requirements are all verified by means of Inspection, Testing, Analysis or a design review.

4 Design description

The design description addresses the entire Foil Radiator Assembly (FRA) design but also includes the thermal model, MMOD and structural analysis. The design is established by means of first order approximations and where needed by breadboard tests to support design choices. The main functionalities of the FRA are the deployment and heat dissipation. These functionalities are more difficult to predict and therefore require more advanced models. In this research project it is chosen to model and predict the thermal behavior of the radiator. The deployment behavior is therefore based purely on tests and it is recommended to perform a more detailed analysis or model the behavior during the development of the product, to improve deployment dynamics.

Regarding the mass of the design, reasoning is used to optimize the shape, mathematical optimization techniques are not utilized as the time to optimize is more effectively spent in correlating the test data, since mass optimization may literally save a few grams now, while mass optimization may in a design update be performed more effectively, for example by selecting a different material such as carbon fiber reinforced polymer to make the contour of the FRRS.

The research questions relating to the content of this chapter can be found in section 2.1 and shall be elaborated in section 4.5.

4.1. Foil Radiator Assembly (FRA)

The FRA is an assembly of several sub systems, which are all designed to support the FR. These systems can be seen in Figure 35. Excluded from this product tree are the tooling. These are not part of the (flight) design and are only intended to support the deployment and thermal tests.

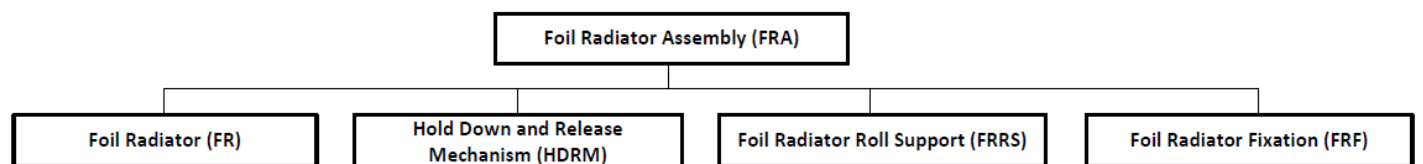


Figure 35: FRA subsystems

In the following subsections, the concepts will be defined for the individual subsystems, leading to the complete FRA design which can be seen in Figure 36.

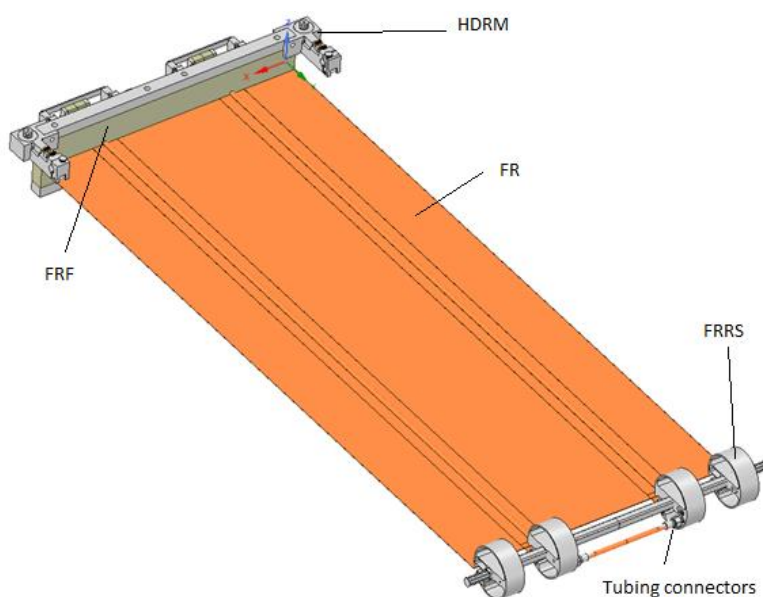


Figure 36: FRA final breadboard design

4.1.1. Foil Radiator (FR)

The most fundamental customer requirements are that the FR shall be deployed and remain deployed based on inflation, that the mass to heat rejection ratio must be relatively low and that the concept should also be scalable. Other important requirements relate to the handling, lifetime, the ability to be held down during launch and for the system to be practical in terms of volume on a S/C. For these requirements, several strawman concepts are identified. Some of these concepts can be seen in Appendix B: Strawman concepts

There is a distinction being made between single deployment and also retractable concepts. The concepts which are selected for the tradeoff, are based on a roll-able design, a design using several (stiff) foldable panels or origami-based techniques, utilizing smaller tiles and complex folding techniques. These are all described and sources are referenced to in chapter 2.3. Regarding the technology demonstration requirement, it is inherently required to deliver a functioning product within the project timeframe, therefore a preference is given to a simple but effective system.

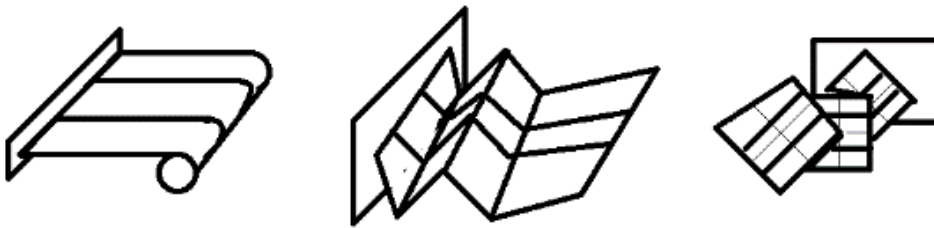


Figure 37: Foil Radiator main concepts

- The rolling system is selected as a concept since it allows for large surfaces to be stowed efficiently within relatively small volumes, without folding the laminate, which has been tested and shown to cause problems to the internal layers of HiPeR. Furthermore, it reduces the chance of plastic deformations in the radiator, decreasing the risk of a non-straight deployed position. The only point of attention is the unused space which is present within the roll during launch. However, this can be minimized by identifying the minimal rolling radius.
- The hinged concept exists of several panels which are connected by tubing and which can be stacked on top of each other. The system can also make use of metal tubes which have a reduced chance of being punctured by MMOD and which have a better conductivity than polymer tubes, of the same thickness. The deployment however can be difficult to predict since the flexible tubes may experience plastic deformation, and the tubes may be closed due to folding which may require additional subsystems to guarantee a repeatable deployment.
- The origami concept is selected since this technique can potentially store a large complex structure in any predefined volume. However, as a result many folds shall be present in the radiator, which also reduces the effective radiator surface. Since the folds cannot be made in the HiPeR foil without possibly breaking the thermal path which is based on the Pyrolytic Graphite Sheet (PGS), each panel must be placed in thermal contact with the tubing. This may result in a relatively heavy or stiff result which is difficult to fold. A repeatable deployment may also be an issue due to deformation, however due to the distributed tubing may be more reliable.

The tradeoff between these concepts is based on the discussed criteria. The results are shown in Table 10. Note that complexity not only relates to design, but also handling effort. Degradation is related to the amount of damage occurring to the HiPeR laminate after stowing multiple times.

Table 10: Trade off tube concept

		Criterion				
		Stowed volume	Degradation	Complexity	Mass	Reliable deployment
Concept	Roll able	Average	Good	Good	Average	Average
	Foldable	Good	Average	Average	Average	Undesirable
	Origami	Good	Undesirable	Undesirable	Undesirable	Good
Scoring		Good	Average	Undesirable		

The concepts which are considered can be used for a single deployment design. Retractable options are identified for the rolling concept Appendix C: Deployment concepts. Since this is not a requirement, it is not included in the trade off,

however this may be interesting for future developments, such as making the FR retractable by means of party whistle concepts such as shown in Figure 38.



Figure 38: Breadboarded "Party whistle" concepts

The result of the tradeoff is that the roll able concept is confidently identified as the best concept for the INFRA project. Especially the low degradation and simple handling makes this a valuable concept. None of the concepts score good on mass properties, which is because all the concepts require some sort of stowing structure for stowing the radiator in safely during launch. The origami concept however also requires more tubing to connect to all panels and thus more mass. The heat performance is not addressed since all concepts can be equipped with multiple fluid lines and/or low spacing to increase the performance. On the criteria such as stowing volume and reliable deployment it does not outperform the other concepts, however since the criteria are still rated acceptable the roll able concept is considered to be the best choice for INFRA. In the following sections, the tube and its interface with the FR is selected.

4.1.1.1. FR Tubing

To identify the possible tubing to be used in the FR, a design option tree is generated which can be seen in Figure 39.

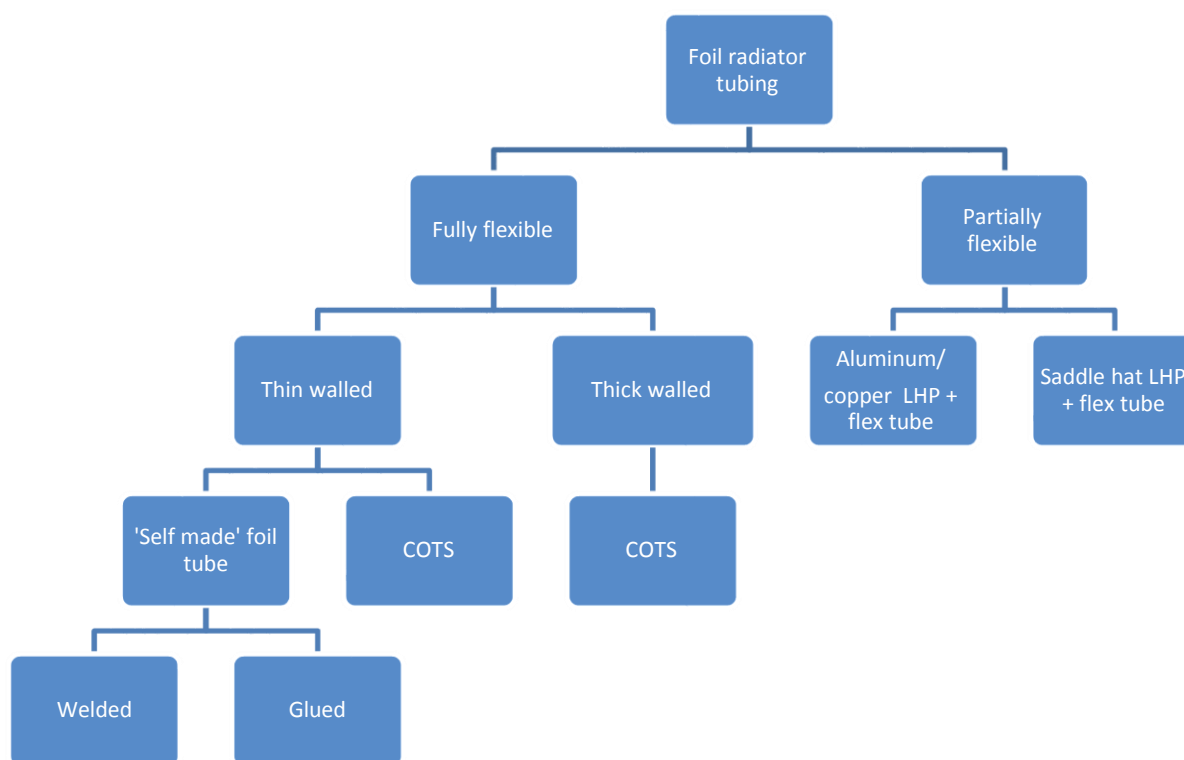


Figure 39: FR tubing Design options

The design option tree first of all distinguishes between a fully flexible and a partially flexible design to include the option of making the FR stiff in one dimension such as a roll-up ladder. This could reduce the risks of a puncture by MMOD. The fully flexible options distinguish between thin- or thick-walled tubing. The thin-walled tubing can be bought COTS or be self-made by means of an adhesive or a welding method.

Partially flexible tubes however make the design heavy, which is undesirable for the client and it will require interfaces between the solid and flexible tubes, which may increase the risk of leakage. Furthermore, it is also more complex to inflate and support the partially metal structure during the deployment test. Therefore, the choice is made for a completely flexible design, and since the thick-walled tubes limit the effect that pressure has on the stresses in the wall and thus on the shape of the tube, thin walled tubing is selected. Self-made tubing shows serious opportunities since it allows for the possibility to use practically any polymer foil available, depending on the option to heat weld or use an adhesive on the material. It also allows customization of the wall thickness and the radius. However, the heat weldable PET/PE foil tube tests showed that it can be very hard to prevent leakage [8]. Furthermore, it would require advanced techniques which are unavailable at Airbus NL to produce a customized reliable tube of a higher quality material than PE. The self-made tube by means of adhesive, can be unreliable over time as the fluid may eat away the adhesive and particles could end up in the flow, which affects the operation of the PA. Since thin walled tubes are available and appear to be more reliable, it is chosen to use COTS thin walled tubes.

Based on the procurable options a selection is made between several materials. The materials have in common that they can be procured in thin walled versions ($t_w < 0,1 \text{ mm}$), that they are highly radiation resistant, that they have high tensile strength, that they are resistant to Galden and Ammonia and that they can sustain operating temperatures as provided in the requirements. The tubing must be able to sustain radiation since it is thin walled and structural properties will degrade due to the ionizing effects of radiation which may pose a problem as the tubes will be pressurized. Based on these requirements, a selection is made between capable polymers which showed strong characteristics on these various terrains. Polymers are chosen for this application as these are flexible and since these are widely used and proven to be highly dependable for all kinds of fluid transfer. The result of the tradeoff is shown in Table 11.

Table 11: Thin walled COTS material selection

		Criterion				
		Radiation resistance	Tensile strength	Cost	Chemical resistance	Production experience
Concept	Kapton	Good	Good	Average	Good	Good
	PEEK	Good	Good	Undesirable	Good	Undesirable
	Polyurethane	Good	Average	Good	Undesirable	Good
Scoring		Good	Average	Undesirable		

Poly Ether Ether Ketone (PEEK) is a capable material. However, no manufacturers are identified which produce these tubing of the required dimensions as COTS. An attempt is made to order a custom-made tube from PEEK, however the manufacturer explained to be inexperienced with this product and could not guarantee the designated tolerances, furthermore the offered price for this product is much higher than that of the COTS Kapton tubing. It is however unknown if other manufacturers exist which could offer better quotations. Polyurethane (PUR) was identified to have a lower mechanical strength than Kapton and PEEK and not to be compatible with ammonia. Since this could become a liquid of choice in a future design, it is requested by the NLR to use tubing which are compatible with ammonia. Besides the reasons named before, Kapton is a material which is already used in the radiator and it can be attached by using tape adhesives which have been tested as well, therefore the choice seems to be most grounded to use Kapton as tube. Regarding the use of Kapton tubing, no direct leads were found that it is incompatible with the substances except for water. Since water may be used during the tests, it is taken into account that Kapton water absorption is relatively high as the manufacturer of Kapton film suggests [36] a loss of $\sim 50 \text{ MPa}$ in tensile strength during the first 300 hours. Safely assumed is that the non-boiling water will have a similar effect. Therefore, breadboard test including water shall be limited in time to minimize mechanical property alteration.

4.1.1.2. Tubing interface

Since all of the heat will enter the radiator through the tubing interface and the flexibility of the FR will be almost completely dependent on it, the tubing interface is chosen based on a combination of these properties. The interfaces considered for the FR can be seen in Figure 40. Since in the previous section during the tubing selection a choice was made to use a flexible tube, concept 2 which contains a solid saddle hat heat pipe, is excluded from the selection. Furthermore concept 5 is shown since it demonstrates a high potential due to its large contact area between the fluid and the laminate. For this goal a tube is discovered which is called lay-flat tubing, which could be made from PEEK, however since the manufacturer could not make any promises regarding tolerances of the manufactured wall thickness, concept 5 is also excluded.

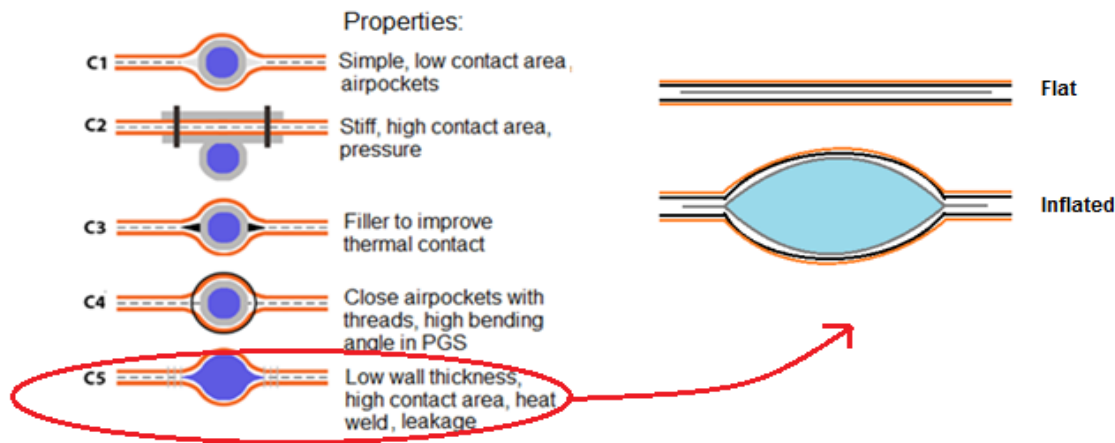


Figure 40: Tubing interface concepts

Interface C1 is the simplest interface which however does not include full contact area between the tube and the foil. The third interface utilizes conductive filler material to fill the pocket of concept 1 to improve the thermal contact. C4 uses thread to tighten the interface and maximize contact area between laminate and the tube. A tradeoff is performed in Table 12.

Table 12: Interface trade off

		Criterion			
		Thermal contact	Flexibility	Degradation	Assembly
Concept	Concept 1	Average	Good	Good	Good
	Concept 3	Good	Average	Good/average	Undesirable
	Concept 4	Good	Undesirable	Average	Average
Scoring		Good	Average	Undesirable	

The tradeoff shows that the first concept is selected because it scores good on almost all criteria. The third concept scores also well and even has a better contact area between the tube and laminate. However, depending on the choice of thermal conductivity filler, it may be very difficult to actually implement the filler within the FR. In case a smear or oil is used it may exit the FR from the sides and contaminate the FR. And a filler made from Pyrolytic Graphite or any other highly conductive material must be tailored to fit next to the tube. Also, during the breadboard tests, it is noticed that PGS has a bad cohesion with the adhesive used in the interface, therefore it is not considered for the INFRA breadboard model. Concept 4 scored worst and is therefore not selected.

After selecting an interface concept, a bending and delamination test is conducted using various methods different methods of applying adhesive. Figure 41 shows the tested interfaces.



Figure 41: Tubing-laminate interfaces

The first two i/f's are symmetric. The left i/f is completely connected to the foil and the center i/f is partially attached to make sure the laminate does not delaminate due to the sharp angle in the intersection (Figure 42).

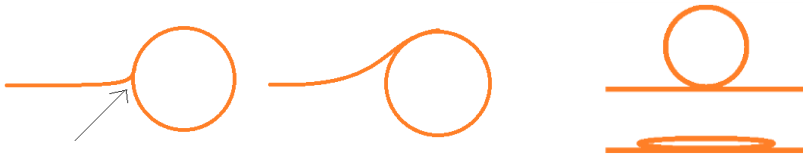


Figure 42: Sharp angle may cause delamination within the laminate (left) flattening tube does not affect with of underlying laminate (right)

It is however noticed, that when bending the interface around a cylinder of $D = 10 \text{ cm}$, the second and the third interface show signs of delamination within the HiPeR laminate. The reason for this is most presumably related to the application of adhesive. In Figure 43 it can be seen how the adhesive is applied. It is assumed that due to the complete surrounding of the interface in adhesive, there is less friction between the layers as a result of a more compact interface. Concept 3 is also completely covered in adhesive, however due to the sharp bend angle at the bottom of the tube, the HiPeR tends to delaminate there internally. Interface 1 is therefore selected for the FR.

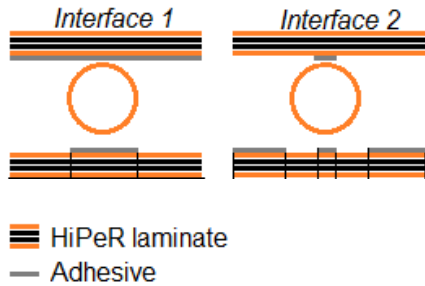


Figure 43: Lay-up Interface 1 & 2

4.1.1.3. Tubing layout

Besides tubing interface, the distribution of tubing, is an important aspect of the radiator performance. To obtain a high performance and radiator efficiency, the tube spacing can be set to a certain optimum. By modelling HiPeR, an estimation regarding the fin efficiency can be made. Depending on the interface and the fin length, HiPeR is capable of having a high fin-efficiency ($\eta_{fin} \geq 80$) for a fin length of $L_{fin} = 0,1 \text{ m}$ (in space environment) due to its high in-plane thermal conductivity. Therefore, it is theoretically possible to have an efficient radiator ($\eta_{FR} = 50 \pm 10\%$) of width $B_{FR} = 0,4 \text{ m}$ the mentioned plan view is shown in Figure 44 on the left. Notice that the dimensions of the FR are based on the requirements as well as the manufacturing limitations.

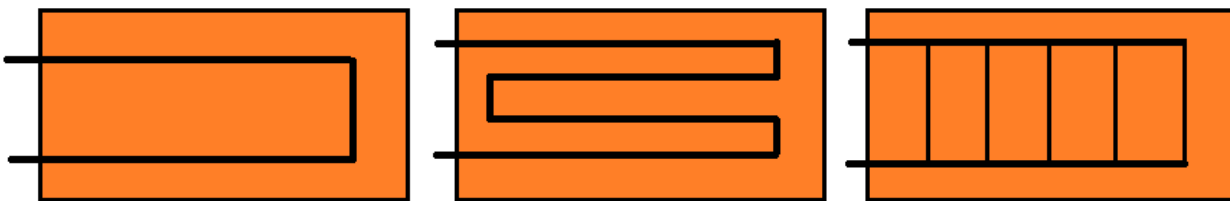


Figure 44: FR tube spacing concepts

As can be seen in the figure, preference is given to symmetrical designs to provide equal stiffness over the length of the FR, which is the least stiff dimension. The second design and the third concept both have a relatively high efficiency. The third design however requires several additional connectors. The additional lines of fluid also make the latter concepts heavier and stiffer, which may cause problems while rolling up the FR. Since the first concept is sufficient to demonstrate the technology, this will be used for INFRA. In case the efficiency must be improved in a future design, an upgrade to the second concept is easily performed.

4.1.1.4. Tubing connector design

The heat welding method also shows to be useful for interfacing between various tubes in the breadboard tests. Since the foil can be welded into almost any kind of shape by means of a soldering iron or a dedicated heat welding device, it can be made to connect two tubes with different diameters. A demonstration of several fittings is shown in Figure 45. The foil tube does require an isolation like tape between the fittings and a strap such as a ty-rap to compress the

interface and make it leak tight. However, since it was tested and shown to only sustain a limited amount of pressure, and to be susceptible to leakage, it is not considered as interface for INFRA.

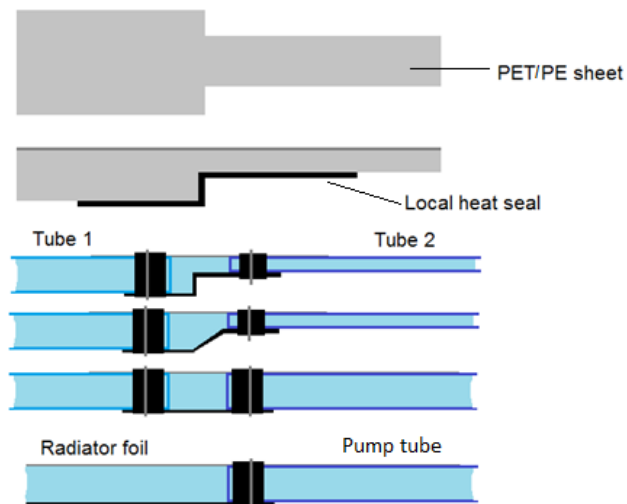


Figure 45: Heat sealed PET/PE tubing as interface between various sized tubing

As a replacement of the foil connectors, a more robust design is identified. The locations of the connectors can be seen in Figure 46.

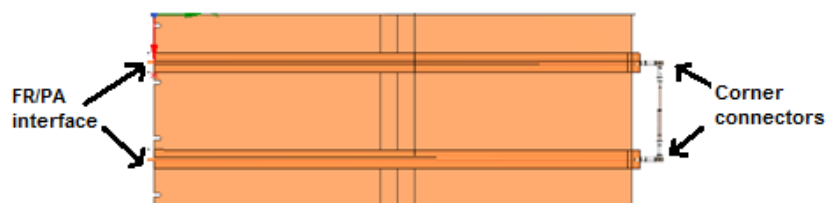


Figure 46: Corner connectors and FR/PA interfaces

Two connectors are placed at the interface with the PA and two more are placed within the FR roll support to support the 90-degree angle within the laminate, which cannot be made by the straight tube. For these 90 degree turns, usually barbed connectors are used. But since they only connect well with thick elastic tubes, and an alternative are COTS steel connectors, which are heavy and may be difficult to connect to a roll up system, a dedicated aluminum connector is designed for which several concepts are identified which can be seen in Figure 47.

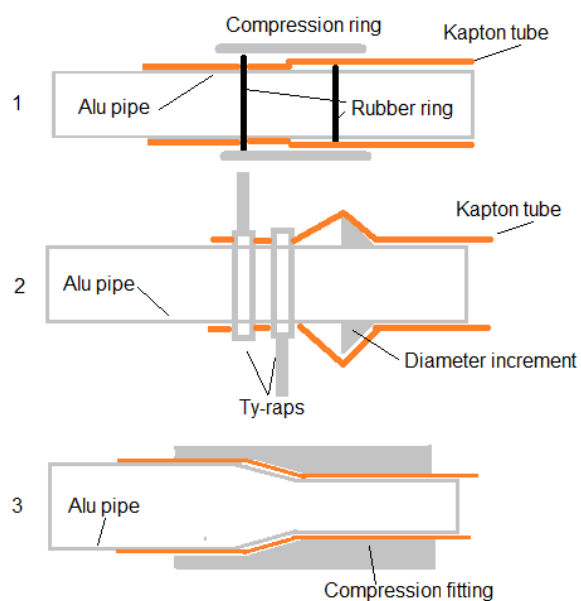


Figure 47: Connector concepts

The first concept uses rubber rings to form a seal which is compressed on the inside and on the outside of the Kapton tube. Since the tube is pulled under and over the rubber ring, a fitting is created that also allows some loading in the axial direction of the tube. The second concept uses a locally increased diameter of the pipe similar to a barbed connector to make the tube stretch and tightly connect to the pipe section such that no fluid is leaked. The ty-rap(s) are then placed behind the barb to support forces in the axial direction that might pull the tube over the slope. The third concept uses a compression fitting which is slid over the pipe which has a small tapered section milled into it. The tube is therefore stretched somewhat which creates a tight fit. The compression fitting provides extra pressure on the material to make it leak tight and to make the tube not slip when axial forces are introduced.

Eventually the three concepts are compared and it is clear that the most important factor of the design is its leak tightness in the long term. Since rubber degrades and loses its flexibility over time, the leak tightness may become less sure. Ty-raps leave an opening and may locally apply high stresses on the tube material which can lead to failure. The third concept is therefore the most elegant solution with the highest chance of long term functionality. Additionally, a leak test shows that the compression fitting is sufficient to strongly support the tube as well as provide a leak tight solution. However, it must be noted that during the leak test a straw was used made from Polypropylene, which has better stretching abilities than Kapton and was also slightly thicker than the eventual tube. Therefore, this test is repeated using the real tube to make sure the results are the same. Concept 3 can be seen in Figure 48. Since this concept is proven it shall be used in INFRA.



Figure 48: Connector concept 3 breadboard test

An additional upgrade to improve the design in a later stage can be seen in Appendix D: Design options. This model uses a screw thread and a nut to tighten and manually compress the fitting.



Figure 49: Corner connector

The corner connector which is shown in Figure 49 is based on the regular connector. However, its end is slid into a cubical shape which directs the flow around the 90-degree corner into another connector. On top of the corner piece, a small dot is produced which can be used to center a Vespel (PI) bridge part, which is used to provide thermal isolation from the FRRS, which is described in the next section. The part is made from Vespel which is strong, stiff, can sustain high temperatures, it has low thermal conductivity and it can be milled easily. The Vespel part is placed over the cylinder shape and may be glued onto it, however it is not necessary since the aluminum part will become warmer than the Vespel and due to thermal expansion, the H7 fitting also ensures a firm grip.

4.1.2. FR roll support (FRRS)

A rolling system is designed to provide rolling support to the FR which can also be used to safely stow the FR in the HDRM during launch. Therefore, a low mass cylindrical shape is designed, which can be easily manufactured and which can be placed around a central bar which connects to several cylindrical shapes or 'Rollers' as shown in Figure 50. The inner rollers are connected to the tubing, the outer rollers are in this case used to provide more stiffness to the rolled-up foil to destructible prevent vibrations within the foil during launch. Appendix D: Design options shows alternative cylinders which can be used on the ends. The diameter is determined from the length of the corner connectors.

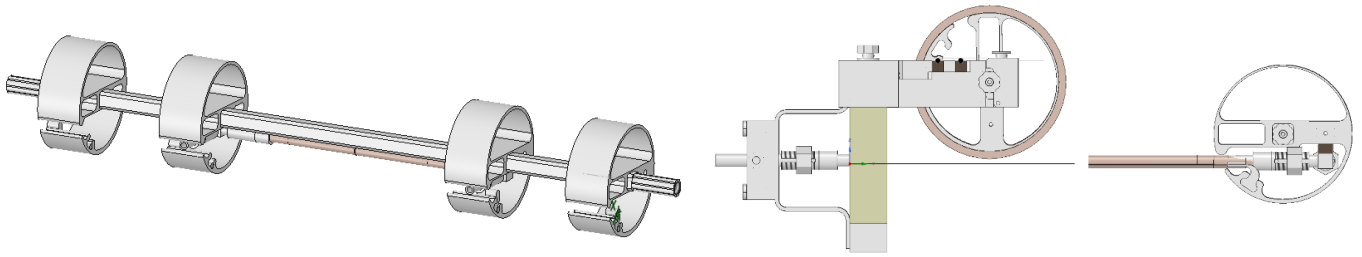


Figure 50: FRRS (left), stowing of the FRRS in the HDRM (right)

The inner rollers can connect to the tubing by inserting the corner connectors and while rolling, they compress the tube such that the flattened tube can be folded around the rollers such that it can be stowed as seen in Figure 51. Additional rollers can be added at the cost of mass and balance (since it is a tip mass) however it can be easily scaled with the spacing of the tube in the FR.

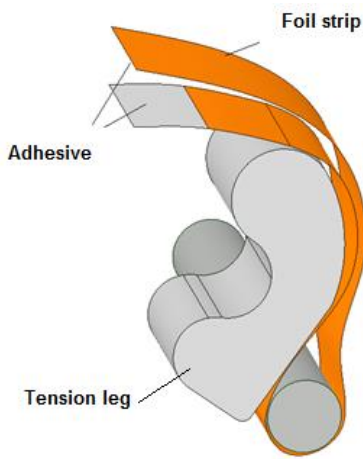


Figure 51: FRRS to FR interface: Foil tension legs and strips

The design is producible either by milling aluminum or by 3D printing due to its easily printable shape furthermore, with corners of $r_{mil} \geq 2\text{ mm}$ and a depth of $d_{roll} = 3\text{ cm}$, which is manufacturable by most milling machines.

Inside the rollers are foil attachment legs. The foil attachments are used hold the foil straight in place and prevent any handling loads to act completely on the tubing connectors. The foil attachment legs are shifted into the roller from the side, such that they can be mounted after placing the tubing connectors in the center of the roller. Thin Kapton strips can be connected by means of adhesive to the FR and be placed behind the legs. A bolt is then used to secure the foil strips. See Figure 51 for the foil legs. Figure 52 shows the design, the prototype and the final model which is used for the INFRA breadboard. The final model is also equipped with a corner connector in the figure.



Figure 52: Roller: 3D CAD design, to 3d printed prototype, to 3d printed breadboard model

The bar which connects the rollers (Figure 53) is required to be able to endure the forces and moments as a result of launch forces. The shape of the bar is chosen to provide a large second moment of area which can transmit torsion which occurs in the Rollers and still be relatively easy to manufacture. I-beams and half cylinders were also considered;

however due to the required tight fitting, these options were discarded due to the manufacturing difficulties and related tolerances.

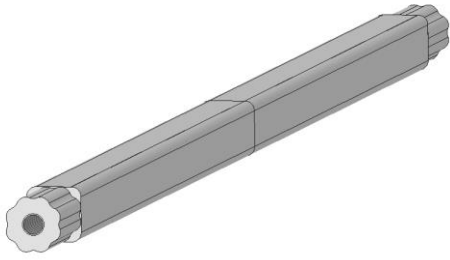


Figure 53: FRRS bar

The rollers are connected to the bar by sliding them over the bar and attaching them by means of adhesive or by thermally exciting the material. Once the thermally excited bar is expanded into the rollers, it is stuck and cannot be removed afterwards. For the breadboard it is sufficient to use adhesive since vibration tests are not included. The bar also contains end pieces which can be mounted into the HDRM. The octagonal shape makes it possible to rotate the bar 45 degrees between locked positions. This provides an option to choose a tighter or less tight fit while handling the rolling up of the radiator. Additional adjustments to the fitting can be made by repositioning of the FR within the FRF, which is described in the next section.

4.1.3. Foil radiator fixation (FRF)

The FRF is used to clamp the base of the foil radiator and at the same time provide a platform to which the HDRM as well as the tubing supports can be attached. In Figure 54 it can be seen that aluminum clamps are used to pressurize two isolative stacks, which are made from Norcoat Liege plate, onto the foil of the radiator, such that the FR base is locked tightly while preventing any damage to the laminate as well as provide thermal isolation between the s/c wall (FRF) and the FR. The reason that the full width of the FR is used, is to make sure the entire base of the radiator is clamped as what would most likely be the case with integration in a S/C wall. The thickness of the Norcoat stack was found from a compressive test, showing the maximum thickness allowed before instability would occur due to compression.



Figure 54: Foil Radiator Fixation 3D design to breadboard model and mounting of HDRM onto FRF

The FRF is also used to support the interface with the PA. Since the interface may be loaded with forces and since the tube is also generating heat, the interface is supported by a similar clamping system as the FRF which can also be seen in Figure 54. For integration with the S/C wall, this component should be revised in a later stage of the INFRA development schedule, since available volume may vary depending on the S/C and location of placement on or within the S/C. The FRF also houses a HDRM on both sides, which is used to hold the FRRS ends. The location of the HDRM is shown as well in Figure 54, and is discussed in the next section.

4.1.4. Hold Down and Release Mechanism (HDRM)

The HDRM has the function to hold down the FRRS bar during the launch and release it after orbit insertion such that the FR may deploy. The required functionalities are all combined into the bracket which shall be elaborated in this section. The concept design of the HDRM can be seen in Figure 55.

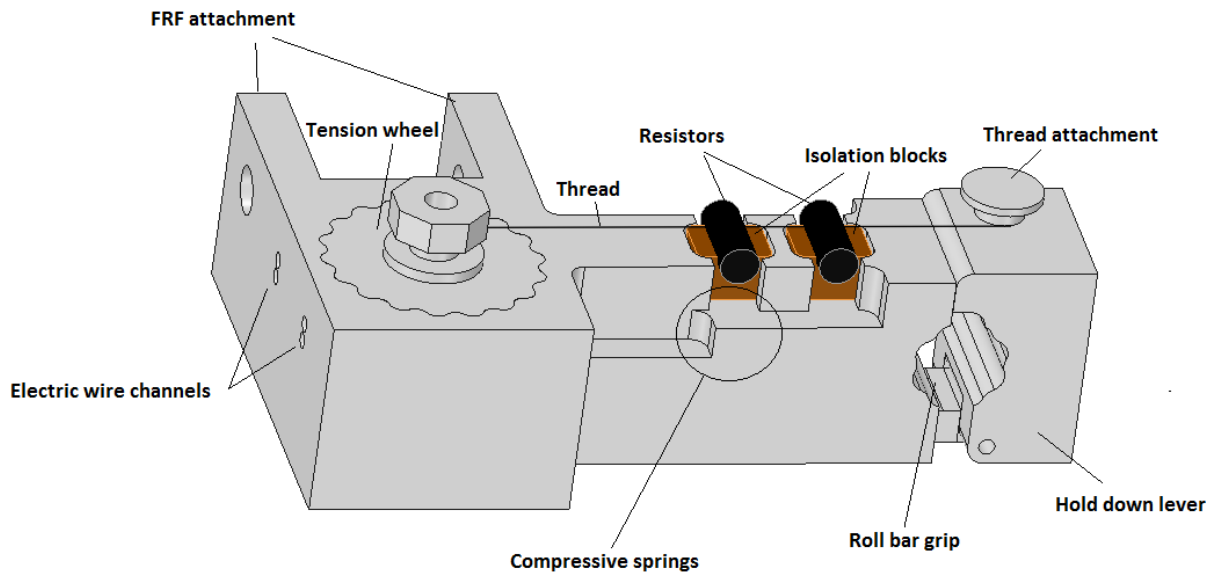


Figure 55: HDRM conceptual design

The HDRM uses a lever to capture the roll bar and a thread to close it. The thread is made from Dyneema wire which is also used in the MHRM [44] and which has a relatively high tensile strength can be molten at relatively low temperatures. This material opens up the option to melt the thread with a COTS resistor such as was already performed on the Delfi-C³ nano-satellite [45]. The thread is placed under a tensile force, sufficient to hold the lever in closed position while experiencing the 30g launch accelerations. The tension is placed manually by rotating a tension wheel by means of a wrench. The tension wheel is finally locked when the pretension is sufficient.

The thread is cut by redundant resistors. These generate sufficient heat as they are placed under a voltage source of $U_s = 2\text{ V}$ and will reach a temperature $T_r > 200^\circ\text{C}$ within the required time [INFRA-BB-SR-5.2.9.3]. The Dyneema thread is slowly heated until it melts. Springs are used to provide contact between the resistors and the thread to prevent damage to the resistor due to the tensile forces in the thread. Furthermore, the resistors are placed on top of Vespel which thermally isolate the resistors, guaranteeing a fast buildup of temperature. Vespel is used to sustain the high temperature which is required to melt the thread. Since Vespel can operate continuously at $T_{max} = 260^\circ\text{C}$, the thermal knife must be switched off manually after melting the thread, which occurs approximately at $T_{cut} = 150^\circ\text{C}$. The resistor which is selected for this task is a conventional resistor ($R = 1\Omega$). More regarding this subject can be found in section 5.1.3. The location of the sockets below the Vespel isolators which hold the springs can be seen in Figure 56.

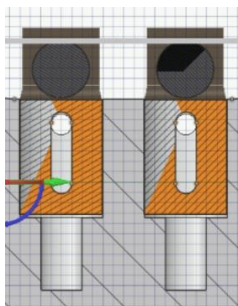


Figure 56: Thermal knife spring sockets

The HDRM is located on both sides of the FRF. The option of placing the HDRM centrally on the FRF and releasing both sides at the same time by means of a shared thread was also considered, however the choice for the individual release configuration is made for the following reasons:

- Short hold down cable
- Hold down main bodies offered sufficient space to house the thermal knife and tension wheel, and therefore it saves mass and volume to not design another centralized cutting mechanism
- At the S/C side of the FRF it will be difficult to operate the tension on the thread due to the tubing which are also held in place around the same location, the sides of the FRF are free

- The disadvantage is that the electrical power required is doubled, however it may be chosen to release each side individually to reduce power required at the same time since the hold down mechanism can be designed to be able to support the bending moments which occur due to a single side release.

The final breadboard model of the HDRM can be seen in Figure 57. It can be noticed that the tension wheel is made circular as it increases the control on pretension in the thread with respect to the toothed shape of the original concept. Furthermore, there is a small hole halfway the thread which can be used to place a pin that holds the thread to allow a mechanical deployment.

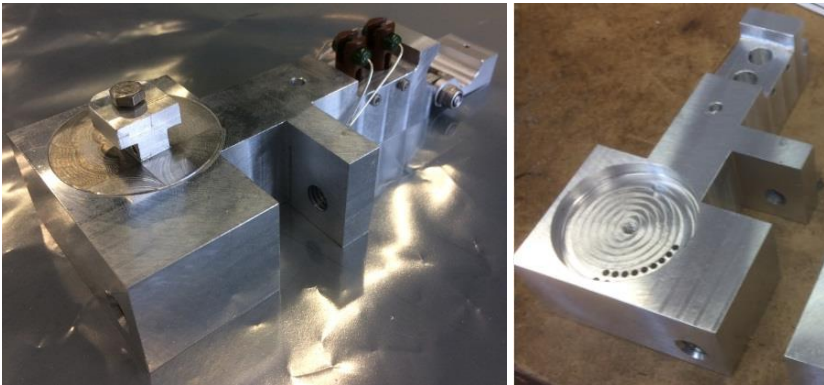


Figure 57: HDRM breadboard model

4.1.5. Tooling

For the deployment and handling of the FRA several tools have been developed. The tooling is designed with the rule of thumb that it must be strong enough to support the RS during the test and therefore mass optimization is not required. Since the forces are not considerably large, the brackets are all designed without structural analysis. The tooling is designed to be mounted on top of an optical table with $D = 6\text{ mm}$ holes with spacing of 25 mm and can remain there while the FRA is tested. The tools which are considered are described in Table 13 and further explained in this section.

Table 13: FRA tooling

Tooling	Application
FR roll-up supports	Hold the FRF while rolling up the FR
Pre-tensioning supports	Support the moment and loads while pre-tensioning the HDRM thread
Hover disk	Support the base of the FRRS and provide low-friction deployment
Deployment support structure	Support the FRF during deployment and testing

The s-shaped clamps as can be seen in Figure 58 are used to hold the FR at table height when rolling up the foil. Since no loads other than that resulting from the FRF mass is expected, small simple brackets are designed for this purpose. The location of the supports is to the sides of the FRF for balance and a M6 bolt hole is used to lock the FRF in place.

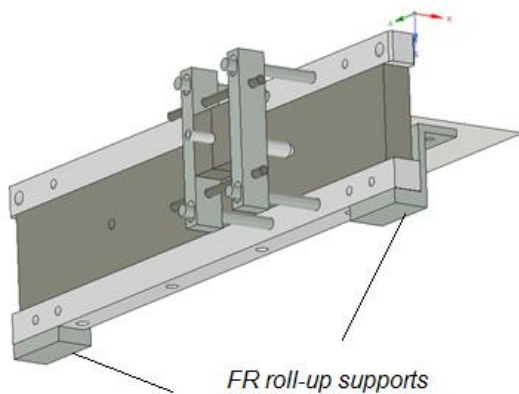


Figure 58: Radiator roll-up tooling

The FRF that supports the HDRM is equipped with pre-tensioning supports to support the loads which will occur while applying pre-tension on the thread by means of a wrench. The pre-tensioning supports can be seen in Figure 59. To spread the loads over several bolt holes, four bolts are used per support. This is to protect the optical table from damage while applying pre-tension to the tread.

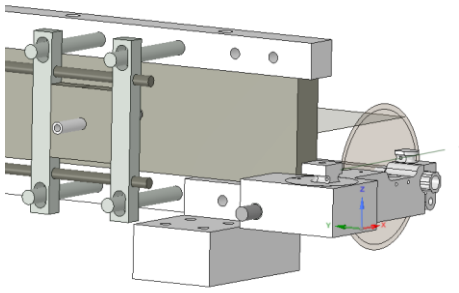


Figure 59: Pre-tensioning supports

The hover disk utilizes three air bearings to lift the honeycomb disk by means of pressurized air from the table surface to create a low friction deployment. The bearings are capable of lifting the platform $20 - 25 \mu\text{m}$ by applying $5,5 \text{ bar}$ gauge pressure according to manufacturer performance data [46]. The applied pressure can be tweaked to obtain proper deployment functionality. The setup of the hover disk can be seen in Figure 60. The base is shaped as a circle to provide a platform that does not collide with the support structure while unrolling the FR while providing a stable platform with equal spacing between the bearings. The disk was made from a honeycomb sandwich, which is low of mass, but with high stiffness. Between the FRRS and the disk is also a cylindrical standoff to make sure that the HDRM does not make contact with the disk. The stability of the disk can be adjusted using the system pressure as it may vibrate slightly and the height of the FRRS may be adjusted using rings near the location of the cylindrical standoff.

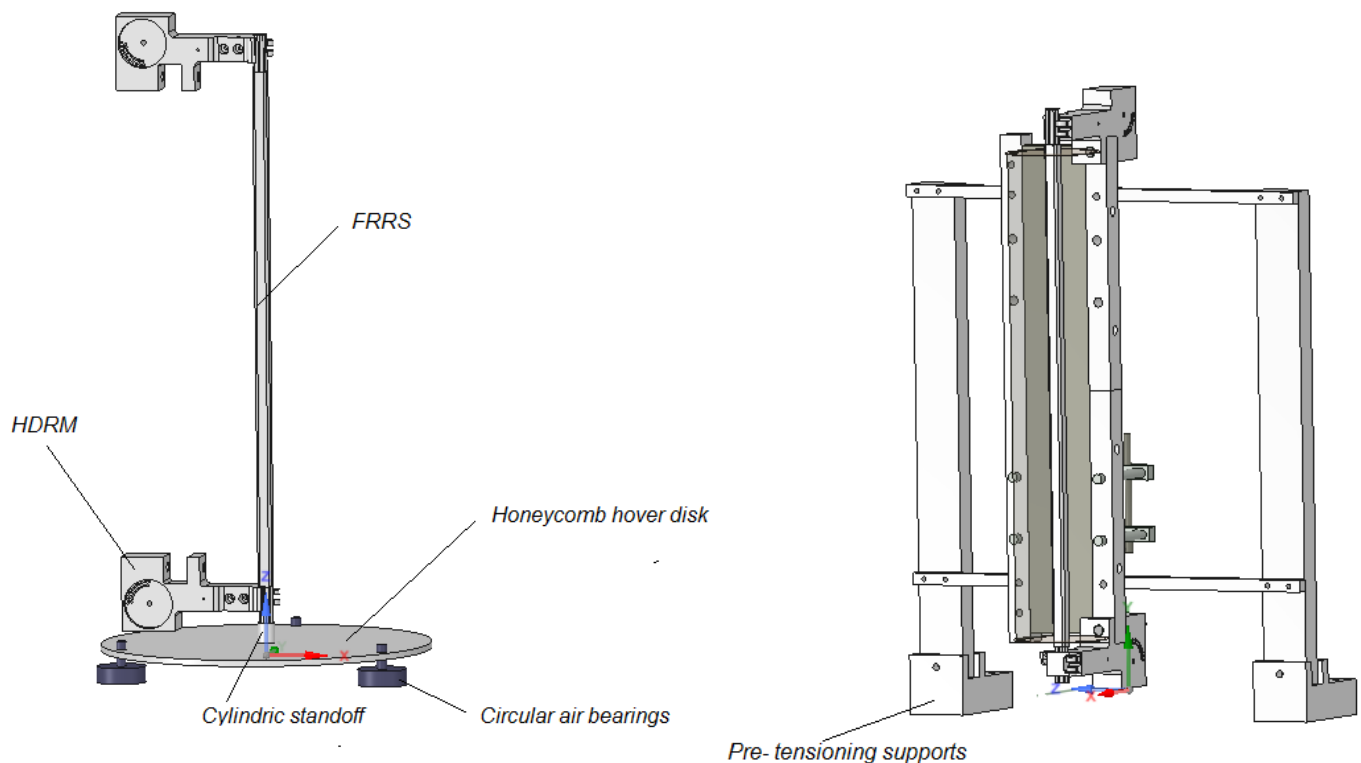


Figure 60: Hover disk deployment platform and deployment support structure

The deployment support structure is designed to hold the FRF in an upright position during the tests. This function is performed by the horizontal and vertical aluminum beams, which can be used to slightly adjust the deployment direction of the FR by adjusting the bolts in the horizontal beams. The structure is mounted on the Pre-tension support tooling that was discussed before and therefore can be easily installed. The structure also can be seen in Figure 60.

$$GL_{1001-11} = \frac{\kappa_{PGS}A}{L} = 0,0485 \left[\frac{W}{K} \right]$$

Note however that only the laminate can be coupled in this fashion. The conductive coupling for nodes 612-622 is not considered since PG is not present in the tubes. The convective and radiative couplings are determined as follows, assuming both sides are exposed and the following parameters apply: $h_{c_{nat}} = 5 \frac{W}{m^2K}$, $\varepsilon_{FR} = 0,93$, $\varepsilon_{env} = 1$, $F_{11-9000} = 1$;

$$GL_{11-9000} = h_{c_{nat}}A_{11} = 5 * (2 * 0,026 * 0,1) = 0,026 \left[\frac{W}{K} \right]$$

$$GR_{11-9000} = \varepsilon_{FR}\varepsilon_{env}A_{11}F_{11-9000} = 0,92 * 1 * (2 * 0,026 * 0,1) * 1 = 0,0047 m^2$$

The tube node couplings are lower as they are based on less exposed surface area. The radiative couplings assume a view factor of $F = 1$ with space. There is some radiation exchange with the FRRS and the FRF however the view factor to the FRF is $F_{FR-FRF} = 0,04$ and the view factor to the FRRS is not calculated however, it is expected to be much lower due to the low radius, the space between the rollers and the cylindrical shape of the roller. Furthermore, the temperature of these objects is also much lower than the FR and therefore these are not taken into account in the model but rather taken into account as uncertainty.

4.2.2. FR-tubing nodes

The tubing nodes are located in the center of the fluid, the inner wall and the center of the laminate as can be seen in Figure 62. In the main model, each foil node which is connected to the tubing also uses two underlying nodes to identify the heat transfer from the fluid to the foil at that location.

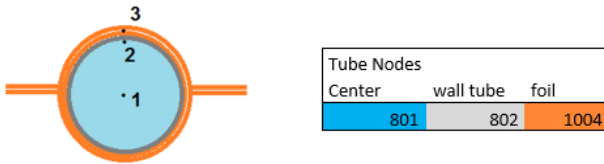


Figure 62: Out of plane tube node locations

The root of the radiator is considered as temperature boundary node, which is located at the center of the entrance point of the fluid. From the root node, the flow is transferring heat by means of advection to the other flow center nodes in the tube. This thermal coupling is (assuming a volume flow of $Q_f = 1 l/min$):

$$G_{adv} = C_{p_{galden}} \dot{m}_{galden} = 963 * 0,0275 = 26,48 \left[\frac{W}{K} \right]$$

From the center of the fluid to the inner wall of the tube (node 1 to node 2 in Figure 62), the heat transfer is performed by convection. For the specific flow rate and liquid properties, the heat transfer coefficient is found in section 2.4.5. The thermal coupling between node 1 and 2 can be determined by:

$$GL_{1-2} = h_{c_{conv}}A_{tube} = 767 * 2\pi * 0,003175 * 0,1 = 1,53 \left[\frac{W}{K} \right]$$

The coupling between node 2-3 is found by summing up the contributions of the individual layers inversely. In the model, a reduction factor of 0,8 is included in the contact area estimation, to compensate for incomplete contact, which can be tweaked during the correlation.

$$\frac{1}{GL_{2-3}} = \frac{1}{\frac{k_{tube}A_{tube}}{th_{tube}}} + \frac{1}{\frac{k_{kap}A_{cont tube}}{th_{kap}}} + \frac{1}{\frac{k_{adhesive}A_{cont tube}}{th_{adh}}} + \frac{1}{\frac{k_{PGS_{oop}}A_{cont tube}}{th_{PGS}}}$$

$$GL_{2-3} = 1,55 \left[\frac{W}{K} \right]$$

It can be seen that the Kapton tube and foil, but also the adhesive has a large influence on the thermal coupling, relative to the PGS. Thickness or conductivity improvements of these layers would benefit the thermal performance since all the heat enters the FR at the tube interface.

The radiative and convective couplings are only relevant for the part of the tube which exits the FR between the FRRS. These couplings are:

$$GL_{612-9000} = h_{c_{nat}} A_{11} = 5 * (2\pi * 0,003175 * 0,046) = 0,0046 \left[\frac{W}{K} \right]$$

$$GR_{612-9000} = \varepsilon_{kap} \varepsilon_{env} A_{612} F_{612-9000} = 0,92 * 1 * (2\pi * 0,003175 * 0,046) * 1 = 0,00084 m^2$$

4.2.3. FRF nodes

2021	2022	2023	2024	2025	2026	2027	2028	2029	2030	2031	2032	2033	2034
1021	1022	1023	1024	1025	1026	1027	1028	1029	1030	1031	1032	1033	1034
1001	1002	1003	1004	1005	1006	1007	1008	1009	1010	1011	1012	1013	1014
1021	1022	1023	1024	1025	1026	1027	1028	1029	1030	1031	1032	1033	1034
2021	2022	2023	2024	2025	2026	2027	2028	2029	2030	2031	2032	2033	2034

Figure 63: FRF nodes

The nodes within the FRF are shown in Figure 63. Introducing the thickness of a single Norcoat stack as $th_{norcoat} = 0,03 m$, and the conductivity $k_{norcoat} = 0,09 \left[\frac{W}{mK} \right]$, which is assumed and known to vary with temperature. We now take two times the area to cover for the contact on both sides. The thermal couplings between these nodes are as follows:

$$\frac{1}{GL_{1001-1021}} = \frac{1}{\frac{k_{norcoat} 2A_{1001}}{\frac{th_{norcoat}}{2}}} + \frac{1}{\frac{k_{kapton} 2A_{1001}}{th_{kapton}}} + \frac{1}{\frac{k_{adhesive} 2A_{1001}}{th_{adhesive}}} + \frac{1}{\frac{k_{PGS} 2A_{1001}}{th_{PGS}}}$$

$$GL_{2-3} = 0,0062 \left[\frac{W}{K} \right]$$

Which shows the large isolative contribution of the Norcoat stack. The couplings between the aluminum and the Norcoat are found from: $k_{alu} = 120 \left[\frac{W}{mK} \right]$, $th_{alu} = 0,02 m$.

$$\frac{1}{GL_{1001-1021}} = \frac{1}{\frac{k_{norcoat} 2A_{1001}}{\frac{th_{norcoat}}{2}}} + \frac{1}{\frac{k_{alu} 2A_{1001}}{\frac{th_{alu}}{2}}}$$

$$\frac{1}{GL_{1001-1021}} = 160,3 + 0,08 \Rightarrow GL_{2-3} = 0,0062 \left[\frac{W}{K} \right]$$

The radiative and convective couplings are determined from the exterior surfaces and are depending on the location. The view factors are again assumed to be $F_{2021-9000} = 1$, and $\varepsilon_{alu} = 0,3$:

$$GL_{2021-9000} = h_{c_{nat}} A_{2021} = 5 * (3 * 0,026 * 0,02 + 0,02^2) = 0,01 \left[\frac{W}{K} \right]$$

$$GR_{2021-9000} = \varepsilon_{alu} \varepsilon_{env} A_{2021} F_{2021-9000} = 0,3 * 1 * (3 * 0,026 * 0,02 + 0,02^2) * 1 = 0,00059 m^2$$

4.2.4. FRRS

The since the FRRS geometry is rather complex, and the heat flow towards it is rather low, the nodes are greatly simplified to the situation as shown in Figure 64.

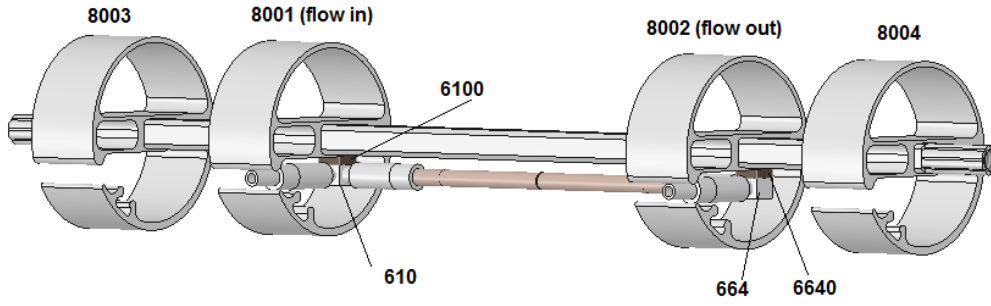


Figure 64: FRRS nodes

The interface with the FR is at the tubing corner node, which is a combination of the Aluminum corner connector (610) and the Vespel standoff (6100), which isolates the FR from the FRRS. Since the corner connector is made from aluminum and the heat transfer coefficient of the fluid is also relatively high due to the narrow passage, it can be assumed that the coupling is mostly determined by the Vespel standoff. Considering the distance or length of the coupling (Figure 65), we can obtain the thermal coupling using: $k_{vesp} = 0,4 \left[\frac{W}{mK} \right]$, $A_{conn} = 0,0001 \left[\frac{W}{mK} \right]$

$$\frac{1}{GL_{610-6100}} = \frac{1}{\frac{k_{AL}A_{conn}}{0,005}} + \frac{1}{\frac{k_{vesp}A_{conn}}{0,011}} \Rightarrow GL_{610-6100} = 0,0036 \frac{W}{K}$$

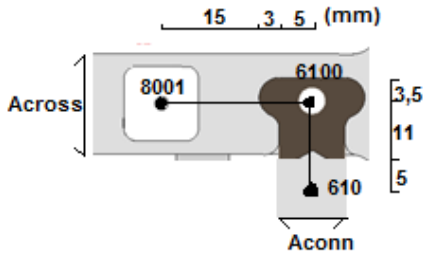


Figure 65: Conductive coupling from corner connector to center of roller

If we consider a worst case scenario, where the temperature of the FRRS is the same as the environment, and the tube connector temperature is the same as the FR root, the maximum temperature difference between the FR and the FRRS can be; $T_{FR_{root}} = 45^{\circ}C$ and $T_{env} = 20^{\circ}C$; $\Delta T = T_{FR_{root}} - T_{env} = 25^{\circ}C$, we can in that case estimate a maximum heat flow of $Q = GL_{610-6100}\Delta T = 0,09 W$. And since this occurs on both sides of the FRRS, we can say that the actual heat which is leaving the FR through this coupling, is so low that it can be considered as a minor loss and therefore the model regarding the FRRS is not further elaborated in this chapter. The space case would however have a larger temperature difference and would lead to a theoretical maximum loss of $GL_{610-6100}\Delta T = 0,0036 * 315,45 = 1,13W$ (per connector). Which is still much lower than the actual dissipation of the FR: $\frac{Q_{FRRS_{loss}}}{Q_{FR_{diss}}} < 1\%$. More elaboration of the model can be found however in Appendix E: Thermal model .

4.2.5. Simulation

The FR is simulated in different environments. For each situation, a root temperature of $T_{root} = 45^{\circ}C$ is considered. The environments are simulated by varying the following parameters.

Table 14: Environment settings

Environment	Temperature (°C)	Convection
Lab	20,5	Natural ($hc = 5 W/m^2K$)
Vacuum	-80	-
Space	-270,45	-

The simulated heat output of the model can be found in Table 15. Q_{in} is based on the sum of heat entering the exposed FR nodes, the FRRS and the FRF are not accounted for in the table. Q_{out} is based on the convective and radiative heat flows leaving these nodes. $Q_{out_{ideal}}$ is used to demonstrate the performance of a 100% efficient radiator (defined here

as $T = T_{root}$ for all nodes). Hence, the radiator efficiency is determined by dividing the total FR heat output over the ideal heat output.

Table 15: Heat balance in the FR

Environment	$Q_{in}(W)$	$Q_{out_{rad}}(W)$	$Q_{out_{conv}}(W)$	Balance (W)	$Q_{out_{ideal}}(W)$	Efficiency (%)
Lab	103,63	51,92	51,71	0	207,7	52
Vacuum	218,85	218,85	0	0	333,3	66
Space	255	255	0	0	385,7	67

Therm XL settings

The following Therm XL settings were used

- Max no iterations = 4000
- Convergence criterion = $1 * 10^{-5}$
- Damping factor = 0,8

These settings produced the best results in terms of both convergence time and heat balance and were therefore used.

The results show an almost equal IR radiative and convective heat dissipation from the FR in the lab environment, which can be verified by using eq. (4.1) & (4.2) which describe the heat which would be dissipated if we consider the average temperature of the radiator. (Table 16)

$$Q_{rad} = \varepsilon_{FR} \sigma A_{FR} (T_{av-FR-foil}^4 - T_{env}^4) \quad (4.1)$$

$$Q_{conv} = h_{c-nat} A_{FR} (T_{av-FR-foil} - T_{env}) \quad (4.2)$$

Table 16: First order estimated heat output FR

Environment	$T_{av-FR-foil} (°C)$	$Q_{out_{rad}}(W)$	$Q_{out_{conv}}(W)$	$\Delta Q_{model-1st ord}(W)$
Lab	33,43	52,66	51,72	0,75
Vacuum	19,90	225,26	0	6,4
Space	15,64	261,86	0	6,9

A comparison with the first order approximations shows an increasing difference in the heat outputs. For the lab model the difference is negligible $\approx 1\%$ of the heat output, however for the vacuum and space estimations a difference of 3% with the model is estimated. It is assumed that this is the result of the nonlinear temperature distribution within the radiator which is not accounted for by the first order approximation. The increasing difference between the model and the approximation seems to be the result of the T^4 term of the IR radiative heat output as plotted in Figure 66 as a function of temperature.

It also shows that the difference in output does not vary much for the colder temperatures, explaining the similar offset for the Vacuum and Space simulation. The curve also shows why a radiation test in vacuum conditions already provides a decent approximation of the pure radiative heat dissipation performance of a radiator in space at a constant temperature, since the output could only increase an approximate 10 % for any lower environmental temperature (see Figure 66). This of course does not take into account the heat sources which are available in space, and which can yet influence the dissipating performance tremendously.

The main model is also compared with two other models which are less extensive and only simulate the FR in 2D. One of those models was used for the sizing of the HiPeR products. The other model was produced to make fast estimations regarding the efficiency and power output of the simplified radiator. The root temperatures which are used for the models are provided by the main model and the location of the foil which is verified is the last line of nodes before the FRRS (191-197) as this part is least influenced by the conductivity of the FRF. The temperatures which are shown are those of the FR foil and do not include the fluid or tubing temperatures. The models are compared in Figure 67, Figure 68 and are modelled from the foil on top of the tube to the outside edge of the foil.

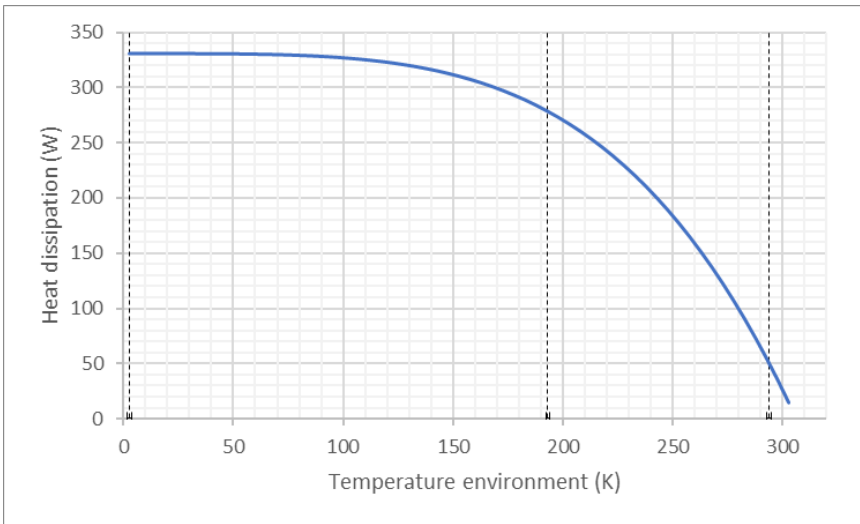


Figure 66: IR heat output of the FR for varying environmental temperatures

It can be noted that the 2D and the main model are almost perfectly similar. The HiPeR model however, has a slight temperature variation at the root of the foil. This relates to the different interface at the root, which impact is filtered out in the simulation. Since the models do not include convection, the lab environment is not compared.

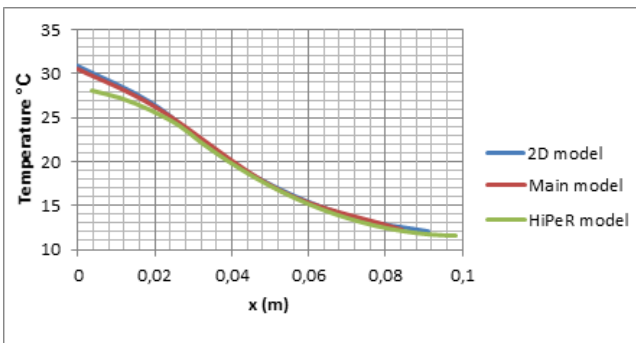


Figure 67: Comparison of 3D main model with two different 2D models in vacuum ($T = -80\text{ °C}$)

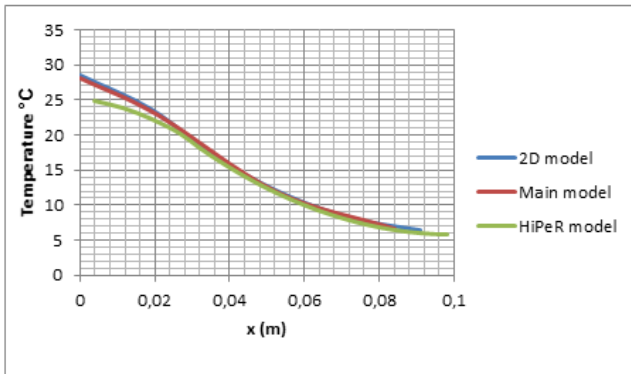


Figure 68: Comparison of 3D main model with two different 2D models in Space environment ($T = -270\text{ °C}$)

4.3. Structural analysis

The FRA is structurally analyzed to verify its ability to sustain launch and handling loads. All components have been analyzed by means of first order approximations regarding critical locations in the design in relation to those loads. This chapter is used to provide only the relevant information to verify the requirements, not to provide a complete workout of the analysis performed. Observations which are made during the analysis shall also be provided.

4.3.1. System mass and scaling

The mass of the FRA defined in section 4.1, is estimated with Ansys Space claim by using the volumes and applicable material properties. The estimated mass of the components and the total system mass is shown in Table 17.

Table 17: FRA estimated system mass

Subsystem	Mass (kg)
FR	0,15
FRRS	0,48
HDRM (2 brackets)	0,54
Liquid	0,12
Connectors + tubing	0,08
Total + Margin (10%)	1,37 + 0,137 = 1,5
FRF (additional)	0,35

The mass which is responsible for the loads on the bar and on the HDRM is a summation of FR, FRRS, Liquid, Connectors + tubing: $m = 0,83 \text{ kg}$, which is rounded to a conservative value of $m = 1 \text{ kg}$. The mass of the FRF is not included in the total system mass since the aluminum clamps are only used for the breadboard demonstration. The real model is integrated possibly by means of Norcoat stacks and for example honeycomb compression panels, which weigh much less than the solid beams which are used here. The total mass should be taken with a 10% margin for excluded items such as bolts and nuts. Note that a mass optimization of the HDRM and FRRS may lead to a total mass reduction of approximately 0,4 kg by mass optimization, however this or other design optimizations are not included in the mass estimations. A rough mass estimation of the scaled system is also provided. We can find how the total FRA mass scales in Figure 69. It is assumed that the following applies for the scaling, which includes a 10% margin. Obviously, it pays off to scale the radiator in length, however this is limited by the stiffness of the FR (section 5.2).

- For each additional 0,4 m of width, a single HDRM bracket and the full original FRRS mass is added
- The dimensions of the metal parts are unaltered except for the length of the FRRS bar
- FR, liquid, connectors and tubing scale in length and width based on the original FR surface area and mass

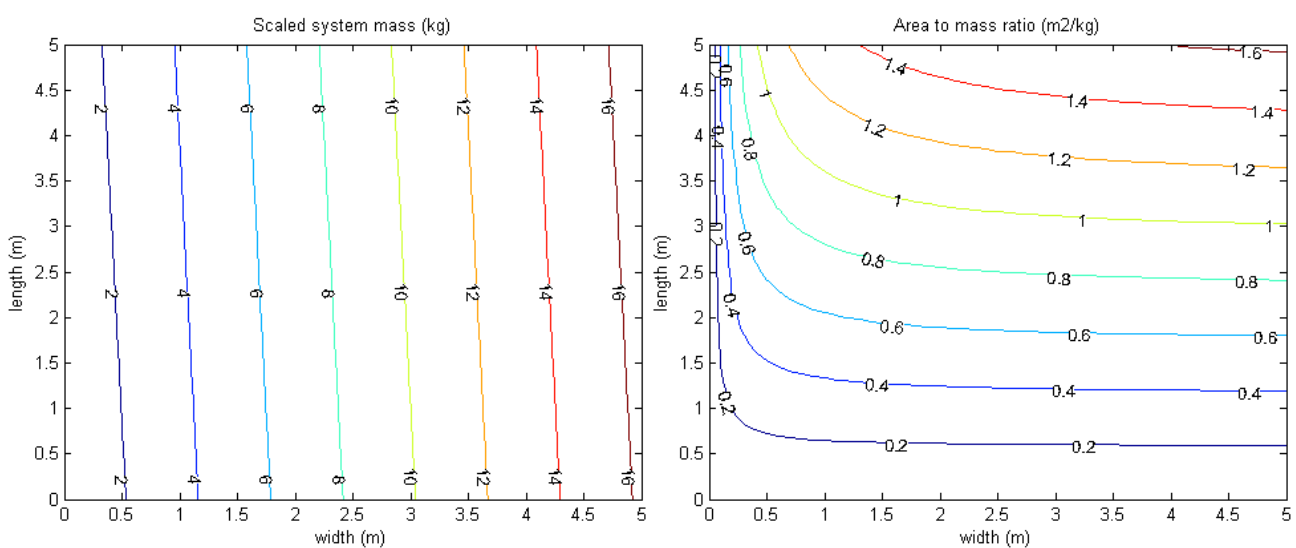


Figure 69: FRA System mass (left) and area to mass (right) contours with respect to scaling of FR length and width

4.3.2.FR

For the verification of the FR structural requirements, the loading conditions which may occur during handling and operations have been analyzed to demonstrate that the FR will not fail during these circumstances. A description of the analysis and the applicable system requirements, are shown in Table 18. The bending moment estimation is however provided since it relates to the test as described in chapter 5.

Table 18: FR structural analysis to verify system requirements

Requirement ID	Description of analysis
INFRA-BB-SR-5.2.7.4	Tube and laminate tensile stresses under Maximum Operating Pressure(MOP) + FRA system mass (without FRF) while hanging straight down from FRF (may occur during handling)
INFRA-BB-SR-5.2.7.4	Tube and laminate tensile stresses under Maximum Operating Pressure (MOP) during bending test
INFRA-BB-SR-5.2.7.2	Maximum bending moment and deflection during operation (moment of collapse) with respect to internal pressure
INFRA-BB-SR-5.2.7.7	Tube and laminate stresses during launch
INFRA-BB-SR-5.2.7.7	Adhesive surface area required to hold the two laminates of the FR together during launch and handling, as well as the connection with the FRRS

The allowable bending moment and the relating deflection, is elaborated. An estimation for the system requirements is provided in section 3.2.1, however an estimation relating to its actual geometry and the previously obtained system mass is provided here.

Bending moment during maneuver

The angular acceleration which is used to find the local acceleration, is found from the moment of inertia of the entire S/C (considered $I_{sat} = 3520 \text{ kgm}^2$ for a communications sat), using a torque generated by $n_{th} = 4$ thrusters delivering a thrust force of $F_{th} = 20 \text{ N}$ each including a safety factor of $s_f = 1,5$ at a distance of $x_{th} = 1,5 \text{ m}$ from the core of the S/C.

$$\tau = s_f n_{th} x_{th} F_{th} = 180 \text{ Nm}$$

The angular acceleration of the S/C is:

$$a_{ang} = \frac{T}{I_{sat}} = 0,0511 \frac{\text{rad}}{\text{s}^2}$$

The average local acceleration at the center of mass of each component is then found by multiplying the angular acceleration with the distance to the center of mass, which can be done since the local acceleration scales linearly with distance. And the bending moment is found by multiplying the resulting force with the distance from the FR root to the center of mass. The resulting moment contributions can be seen in Table 19.

Table 19: FR bending moments during operational load

Components	Distance to center of mass SC (m)	Local Acceleration (m/s ²)	Mass (kg)	Bending moment at FR root (Nm)
FR+tube	1,5	0,077	0,256	0,0098
Tube perpendicular	2,06	0,105	0,051	0,0056
FRRS + connectors	2,04	0,104	0,5	0,056
Total			0,8	0,0714

The stresses resulting from this moment per tube are combined with the maximum stress occurring due to MOP. Taking the second moment of area of two tubes which each have $I_{xx} = \pi r^3 t h = 8,94 \text{ mm}^4$. The result is that the stresses are much lower than the allowable yield stress of Kapton and are thus not critical during operation.

$$\sigma_{maneuver} = \frac{Mr}{2I_{xx}} + \frac{S_f Pr}{2th_w} = 13,51 \text{ MPa}$$

During testing and operations, the worst case could be that the tubes buckle while experiencing internal pressure from the fluid. The term used for this case is collapse load which is higher than the unpressurized buckling load. From

reference [34] obtained is the following equation which calculates the allowable root moment based on structural strength (left term) and internal pressure (right term). The 0,8 term can be adjusted to the moment carrying capability of the tube and is in this reference taken as 80%. However, since the right-hand term is of relatively low influence (< 20% of M_{press}) and the bending moment is not critical, this is not something worth investigating for this tube.

$$M_{press} = \pi r E t h^2 \left(\frac{\gamma}{\sqrt{3(1-\nu^2)}} + \Delta\gamma \right) + 0,8 P \pi r^3$$

Where $E = 2,5 \text{ GPa}$, correlation factors $\gamma = 0,77$, $\Delta\gamma = 0,055$, Poisson ratio is $\nu = 0,34$ of Kapton. This leads to a maximum bending moment of $M_{press} = 0,11 \text{ Nm}$ for a pressure difference of 1 bar with the atmosphere and $M_{press} = 0,12 \text{ Nm}$ for a pressure difference of 2 bars with the atmosphere, showing that the pressure increase only has a small influence on the bending moment. Note however that this is the allowable bending moment on a single tube, the moment which can be carried by both tubes simultaneously is $0,22 \text{ Nm} < M_{press} < 0,24 \text{ Nm}$.

Using the allowable bending moment, the collapse stress for each tube becomes:

$$\sigma_{collapse} = \frac{M_c r}{2I_{xx}} + \frac{S_f P r}{2t h_w} = 21,31 + 7,95 = 29,26 \text{ MPa}$$

This is still not sufficient to reach the material yield of the Kapton tube even when taking a safety factor $s_f = 1,5$ into account. Higher bending moments than this will cause the FR to collapse and therefore it will not endure higher stresses after this point during normal operation.

The tensile stress which may occur during handling while hanging upside down from the FRF is estimated (considering all the mass is carried by the tubes from

$$\sigma_{tens} = \frac{g(m_{FRA} - m_{FRF})}{2A_{tubecross}} s_f = 6,22 \text{ MPa}$$

This is also far below the allowable Kapton stress and therefore considered sufficiently strong.

4.3.3. FRF

The main structural analysis relating to the FRF is performed on the capability of clamping the FR during launch to verify [INFRA-BB-SR-5.2.7.7]. It is sufficient to analyze the situation however; a simple test provided a fast and reliable method to support the analysis. During the launch, the FR may pull itself out of the FRF as a result of the launch load, the distributed load relating to this is

$$W_{FRF} = \frac{F_{launch}}{B_{FRF}} = 1,1 \frac{\text{N}}{\text{mm}}$$

Testing of the same clamping method demonstrated it was capable of carrying 50 N over a Norcoat setup width B of 30 mm. This is sufficient as the allowable load is the expected load times a safety factor of 1,5.

$$S_f = \frac{50}{W_{loc} 30} = 1,5$$

The load which can be carried depends on the clamping force which is applied by the bolts. A maximum pressure is obtained from breadboard tests. In the actual breadboard model this force is delivered by compressing the FRF to obtain the same amount of deformation of the Norcoat material as during test. No margin is included and therefore this should be rechecked in case the launch loads would increase.

4.3.4. FRRS

The structural analysis which is performed to verify the FRRS requirements are shown in Table 20.

Table 20: FRRS structural analysis to verify system requirements

Requirement ID	Description of analysis
INFRA-BB-SR-5.2.7.7	During launch the mass of the radiator may be accelerated in any direction, resulting in force $F_{launch} = 440N$. Due to tensile forces in the FR which is clamped at the FRF, the foil may exert a compressive force on the roller as the FR is pulled around it (Figure 70). This force causes bending + compression stresses at the critical locations of C_1 and C_3 .
INFRA-BB-SR-5.2.7.7	The allowable compressive force relating to C_3 for a single roller is identified to support handling protocols
INFRA-BB-SR-5.2.7.7	The launch load may create a moment around the center of the roller, which may cause shear stresses in C_2 , the stresses should not exceed the allowable limit of the material
INFRA-BB-SR-5.2.7.7	The FRRS bar can bend due to the launch accelerations and the distributed mass of the FRRS which is clamped between the HDRM. The allowable bending moment is verified.

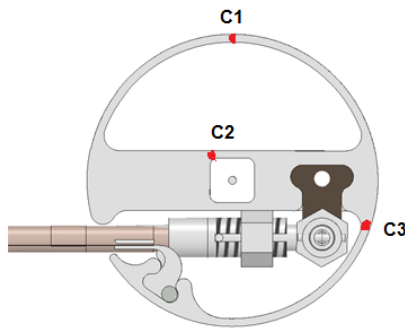


Figure 70: Critical locations on the roller with respect to a radially exerted compressive Launch load

The results of the analysis are that the critical location c_1 will not be loaded sufficiently during launch or handling to be at risk. There is an additional margin that would allow at least twice the launch load. Critical location c_3 is found to be not at risk during launch, however should not be compressed with more than 250 N during handling. The stresses at c_2 also have an additional margin of more than three times the shear stress before the material fails. The beam is bended due to the launch loading and is deflected however an additional margin of more than twice the load is considered before material failure occurs. The first eigenmodes and deflections have been determined by means of first order approximations and have been shown to be conservative by a simplified FEM model. The obtained first order natural frequencies are shown in Table 21. Since the launch frequencies which may be encountered are expected to be in the range of 0-100 Hz, it is therefore likely that the launch load will not be amplified due to the launch vibrations.

Table 21: Eigen frequencies FRRS

Natural frequency (Hz)	F1	F2	F3	F4	F5
FEM	169,38	321,91	1193,29	2571,65	2925,82
Harris functions	128,93	355,12	696,43	1151,12	1715,17
Sakshat	135,58				

4.3.5. HDRM

The structural analysis related to the verification of FRRS requirements can be found in Table 22. The loads which are expected are

- Static launch load ($F_{launch} = 440 N$)
- Single side deployment load ($F_{depl} = 100 N$)

Table 22: FRRS structural analysis to verify system requirements

Requirement ID	Description of analysis
INFRA-BB-SR-5.2.7.7/5.2.7.10	Determination of reaction loads and moments on the HDRM components
INFRA-BB-SR-5.2.7.7/5.2.7.10	Determination of pre- tensile force in the thread to hold the FRRS during launch
INFRA-BB-SR-5.2.7.7/5.2.7.10	Determination of required dimensions of main body, lever and tension cap + parts
INFRA-BB-SR-5.2.7.7/5.2.7.10	Verification of allowable shear stress on curved grappling section of the lever
INFRA-BB-SR-5.2.7.7/5.2.7.10	Determination of required Dyneema thread thickness with respect to pre-tension and relaxation

The loads and moments have been translated to dimensions of the parts with applicable allowable stresses taking into account a $s_f = 1,5$. No critical locations were identified which require additional care during handling. The thread which is used in the breadboard mode is strong enough to carry a load of approximately $F_{tensile} = 6100 N$, while it is only required to carry a load of 180 N. This also reduces the threat of relaxation. A small test is performed (section 2.5.1) to verify this. It is also determined that while applying pretension in the thread, it should not be attempted to stretch the thread by more than 4 pin holes, to prevent the tension cap from being destroyed by the torque originating from the thread and the wrench which is used to apply the torque. The main body is designed with an eye on simple manufacturability and is therefore still optimizable in terms of mass. The stresses which occur in the main body are all well within the allowable limits.

4.4. MMOD risk analysis

The FR is made from polymer tubes, which are easily penetrated by debris or micrometeorites. However, since the surface area of the tube is relatively small it may be sufficient to perform risk mitigation techniques such as redundant fluid loops to reduce the chance of a system failure. In this section it shall be discussed how large the risks are for the tube and if mitigation techniques are indeed sufficient for the design. But before starting the analysis, the tube interface which may be punctured is shortly discussed.

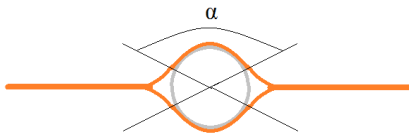


Figure 71: Tube interface

The interface which can be seen in Figure 71 can in case of a failure either be punctured or delaminated. Puncture of the tube would however be fatal for the entire system. This is most likely to occur in the angle alfa on both sides of the tube. The inter-laminar pockets may cause the impacted debris to disperse and due to less concentrated energy, not puncture the tube. However, since this effect may be so little that it may be negligible and also to be conservative in the approach, the entire circumference of the tube is selected as impact sensitive area. Furthermore, a single laminate thickness, is added to the tube wall thickness to determine the penetration thickness $t_{w_{tot}} = 270 \pm 10 \mu m$, which is shown in Figure 72.



Figure 72: Layers which are penetrated

4.4.1. Impact research on Kapton and energy method

Research is performed in reference [47] on the penetration of Kapton by high speed particles. By launching particles of diameter $23 < D < 29 \mu m$ at a velocity of 1730 m/s onto foil thicknesses of 25, 50 and 125 μm , it was tested how the impact area changes due to increasing the foil thickness. By comparing the images of the punctures, the puncture type and size is observed and collectively displayed in Table 23.

Table 23: Compared impact results from [47]

Kapton foil thickness (μm)	Final flyer Velocity (m/s)	Puncture type	Measured size average
25	1400	Ductile rupture	10-50 μm
25	1650	Ductile rupture/ small cracks	10-50 μm
25	1730	Brittle /Radial cracking	500 μm (hole size) 1500 μm (crack length)
25	2900	Radial crack/bitle rupture	1-3 mm (hole size) 1 mm (crack length)
50	1730	Semi-ductile	10-100 μm (hole size)
125	1730	Ductile	50 μm (hole size)

The ductile rupture can be described from the image as a hole without cracks or ruptures. The purely ductile puncture can only be witnessed in the thickest laminate for a flyer velocity of 1730 m/s. However, the thinnest foil displays ductile rupture punctures only at a lower velocity. It can also be noted that these ductile punctures first rupture than grow cracks for higher velocities of the particles. This indicates that the velocity of a particle that just barely penetrates a surface, should produce a crater like ductile puncture, without any cracks.

The loss of kinetic energy of a ΔE_{kf} due to an impact can be described by as the summation of the following energy contributions [47]:

$$\Delta E_{kf} = E_{ks} + E_{sh} + E_c + E_h$$

In which E_{ks} is the kinetic energy which is transferred to the piece of Kapton which sheared off, E_{sh} is shearing energy, E_c is the crack propagation energy, E_h is the energy transformed to heat. For the puncture threshold, it is assumed that the puncture does not produce cracks as with a ductile puncture, and that the part which is sheared off is sheared off without creating flying particles. In that case the energy which is absorbed at the impact is only transformed into heat and shear energy:

$$\Delta E_{kf} = E_{sh} + E_h \tag{4.3}$$

Where $\Delta E_{kf} = m_p v^2 / 2$

The shear energy and force are described in [47] to be:

$$E_{sh} = P_{sh} h / 2$$

$$P_{sh} = 0,85 h L \sigma_u$$

In which: h the thickness of the foil, L is the length of the cut, which equals the circumference of the puncture, σ_u is the ultimate tensile strength of Kapton.

And E_h is the energy transformed to heat:

$$E_h = m c_p \Delta T$$

A graph is produced in Figure 73, based on the energy balance equation, which describes various random metal density particles with varying diameters and energy levels that could puncture the Kapton laminate based on kinetic energy transferred to heat and shear force. Note however that the adhesive and PGS layers are in reality also absorbing heat and are in fact slowing down the particle, which makes this approach rather conservative. It however does provide an indication on the stopping power of the laminate. Note also that this approach assumes the surface of the particle is flat and that the particle is spherical. Impact craters on the Hubble space telescope, indicate MMOD with diameters of 7 to 98 μm and velocities of 2900 to 11500 m/s [47]. This area of interest is indicated by a square in the figure. Shear forces which are related to the cross section of the puncturing particle are also shown in the graph. These are only dependent on geometry and not on density and indicate the instantaneous load which is transferred to the FR during a strike.

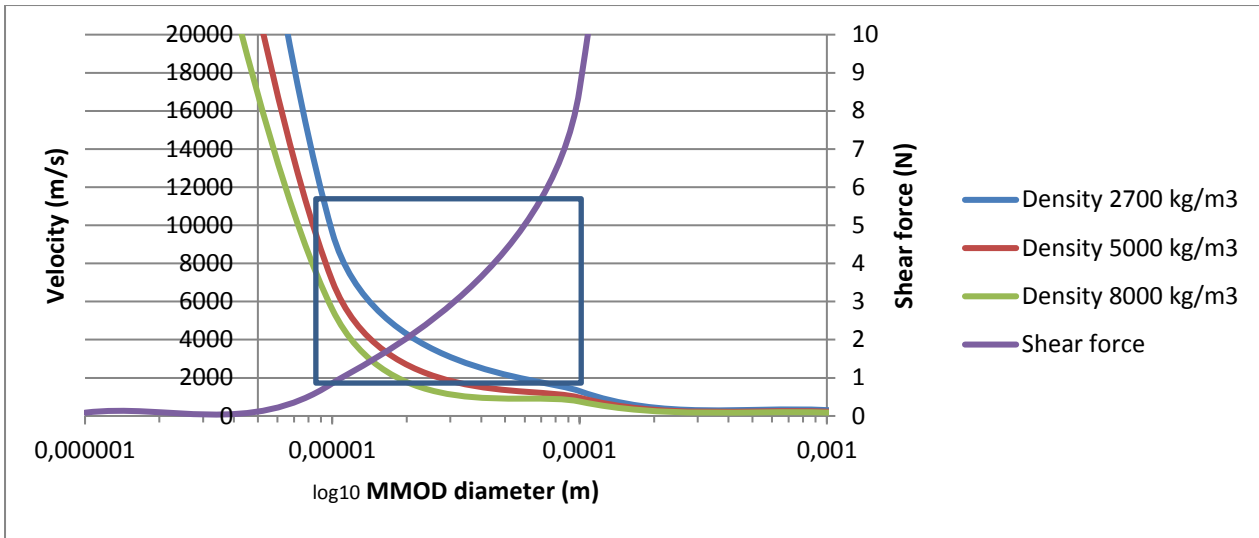


Figure 73: Velocity required to puncture Kapton for various densities and the related shear force

Comparing the impacts on the Hubble space telescope with the velocity and size required to puncture the tube plus laminate, we can see that the impacts which occurred on the Hubble could be fatal for the FR. However, the area of the Hubble telescope is much larger than the tubing area, and therefore the FR tubing area will be held against the density population of various MMOD in GEO in section 4.4.4 and 4.4.5.

4.4.2. Ballistic limit equation

The required wall thickness to stop debris, can also be elaborated using the ballistic limit equation. The approach is elaborated in [39]: The diameter of an impact crater can be estimated by

$$d_c = K_1 d_p^\lambda \rho_p^\beta \rho_t^\kappa v_p^\gamma (\cos \alpha_p)^\xi$$

The maximum defeat able projectile diameter is therefore

$$d_p \leq d_{p,lim} = \left(\frac{1}{K_1 \rho_p^\beta \rho_t^\kappa v_p^\gamma (\cos \alpha_p)^\xi} \right)^{\frac{1}{\lambda}}$$

The minimal thickness to defeat an incoming projectile can be defined by

$$t_t \geq t_{t,lim} = K_1 d_p^\lambda \rho_p^\beta \rho_t^\kappa v_p^\gamma (\cos \alpha_p)^\xi$$

Which uses K_1 as material constant, ρ_p^β as particle density, ρ_t^κ as material density, v_p^γ as particle velocity and α_p as angle of impact. The remaining factors are constants which are defined in Table 24.

Furthermore the following equation relating to the required thickness is found in [12], which derives the equation from the thin plate equation, stating it as the best means of estimating the puncture behavior of meteoroids on plastics. For this equation. [12] uses a general meteoroid density and velocity of $\rho = 0,5 \left(\frac{g}{cm^3} \right)$, $v = 20 \left(\frac{Km}{sec} \right)$.

$$t = K_1 \rho^{1/6} m^{0,352} v^{0,875}$$

Table 24: Ballistic equation calibrated constants of a single wall ballistic limit equation [39]

Source	Target	$K_1(min)$	$K_1(max)$	λ	β	γ	ξ	κ
ESA	thin plate	0,26	0,64	1,056	0,519	0,875	0,875	0
Pailer en gruen	any	0,77	0,77	1,212	0,737	0,875	0,875	-0,5
frost	any	0,43	0,43	1,056	0,519	0,875	0,875	0

naumann et al.	any	0,65	0,65	1,056	0,5	0,875	0,875	-0,5
Naumann	any	0,326	0,326	1,056	0,499	0,666	0,666	0
NASA [12]	-	1,18	1,18	-	0,1666	0,875	-	-

By comparing results using the constants found in Table 24, it is found that ESA (max K1) produces the most conservative results, however shows also closest result to the method from [12]. Therefore, we continue using ESA's thin plate settings to determine the diameters and densities which may be defeated by the laminate.

4.4.3. Comparison with energy method

When comparing the methods, we find the graphs as shown in Figure 74. It shows that the single wall ballistic equations imply that the FR would be able to handle larger diameter MMOD than the energy equations imply. This may be an indicator of the conservativeness taken into account in the energy equation.

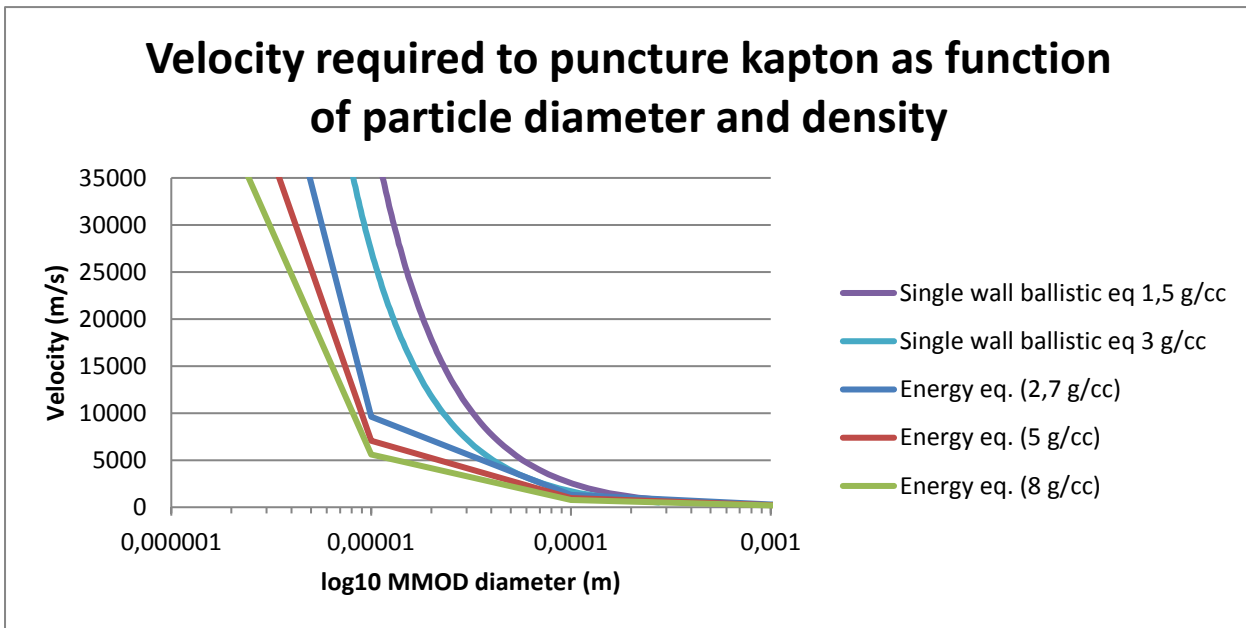


Figure 74: Comparison of energy method with ballistic limit equation for various densities

4.4.4. Meteoroid spatial density

The meteoroids population which is concerned in [39] is mostly assumed to be spherical, and the mass and size of the meteoroids varies with source. The variation ranges from $\sim 0,5 \text{ g/cm}^3$ to $\sim 3,5 \text{ g/cm}^3$ for cometary and asteroid micrometeoroids, where the $\sim 3 \text{ g/cm}^3$ are considered to be of μm scale and the $\sim 1,5 \text{ g/cm}^3$ are scaled in millimeters. A few target orbits are also analyzed in [39] among which the GEO. It is estimated by means of MASTER-2001 software, for an averaged inclination between ($0^\circ \leq i \leq 30^\circ$) that the mean time between impacts on a $A = 1 \text{ m}^2$ spherical surface, is $2,83 \text{ h}$ for particles of $d > 1 \mu\text{m}$ and $20,7 \text{ h}$ between impacts of size $d > 10 \mu\text{m}$. This indicates that the particles which may be damaging for the FR can be expected to strike roughly once on a daily basis on the FR surface. However, if it will hit actually the tube and with which relative velocity is another question.

It is also shown in Figure 75 that the meteoroids have impact velocities between $2,5$ and 30 km/s , with the most probable impact velocity of $\Delta v = 12 \text{ km/s}$ for a GEO orbit.

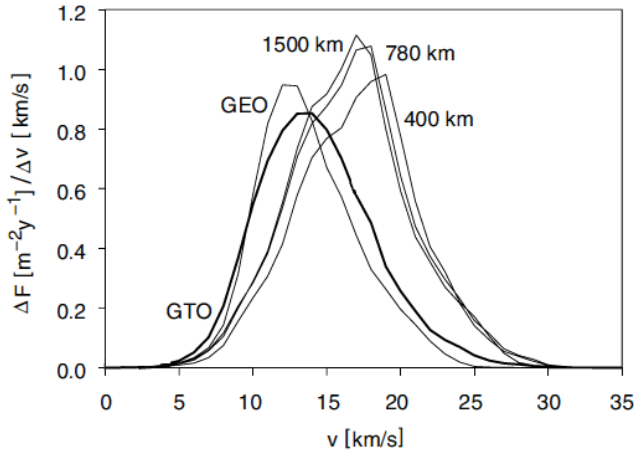


Figure 75: Velocity profile of the meteoroid flux distribution $\Delta F/\Delta v$ for spherical targets on typical Earth orbits [39]

Taking into account a conservative maximum velocity (30 km/s), we can find from the density and diameters, the lowest particle mass that may penetrate the FR at that relative velocity. Below this mass it is assumed there are no particles which may penetrate the FR. The minimal required masses to penetrate at this velocity which is found for $\sim 3 \text{ g/cm}^3$ is approximately $m_{min} = 3 * 10^{-11} \text{ g}$. If we look at Figure 76, we can see how the flux of meteoroids in a heliocentric system is reduced if we do not take into account the particles below m_{min} . The cumulative flux which could be fatal for the FR becomes $N \approx 1 * 10^{-5} \left(\frac{1}{\text{m}^2\text{s}} \right)$.

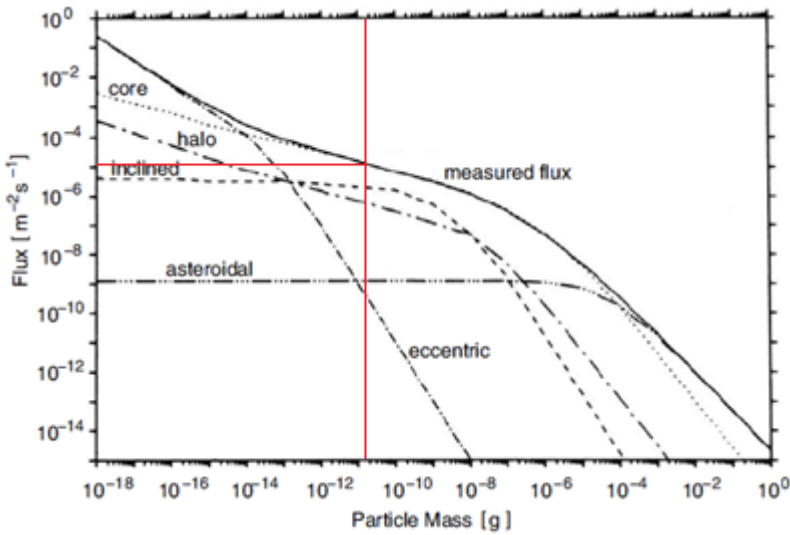


Figure 76: Predicted cumulative meteoroid flux in a heliocentric system at 1 AU, due to meteoroids of masses larger than m_{min} [39]

4.4.5. Collision probability

The probability $P(nocol)$ of no collisions over a period of time τ , onto the total exposed tube area $A_{tube} = 2,2 * 2\pi r = 0,0439 \text{ m}^2$ for this specific flux N is estimated by eq. (4.4) [12]

$$P(nocol) = e^{-NA_{tube}\tau}; P(col) = 1 - P(nocol) \quad (4.4)$$

This is used to determine the probability of a Collision, which is assumed to result in a puncture with probabilities as shown as a function of exposure time in Table 25.

Table 25: Probability of a collision with a mass that may puncture the FR related to exposure time

Exposure time	Probability
Hour	0,0016
Day	0,037
Week	0,23
Month	0,68
Year	1

It can also be determined by using Eq. (4.4) and the cumulative flux from Figure 76, if we strengthen the laminate and tube, such that higher mass particles at 30 km/s can be stopped, we can reduce the probability even during a period of 15 years considerably. If the tube be designed to sustain impact masses of $m_{mmod} \geq 10^{-5}g$, the probability of surviving 1 year in space becomes $P(nocol_{year}) = 1$ and $P(nocol_{15years}) = 0,8$. Which is very desirable.

If we would for example consider stainless steel tubes with material properties such as described in Table 26, we would be able to sustain collisions with meteoroids of mass $m_{mmod} \geq 10^{-5}g$ and the highest density $\rho = 3500 \frac{kg}{m^3}$ particles, by providing a thickness to the tube wall of $t_w = 0,81 mm$. To stop particles of the most occurring density: $0,5 \frac{kg}{m^3}$, we need to have a steel tube of wall thickness $t_w = 0,31 mm$.

Table 26: Stainless steel type 304 material properties [48]

Material property	Value(unit)
ρ	7500 (kg/m^3)
σ_{ult}	505 (MPa)
Hardness, Brinell	123 (HB)
T_{melt}	1455 ($^{\circ}C$)
C	5790 (m/s)
C_p	500 (J/kgK)
K_1	0,345

Note however that we are considering the worst case of maximum particle velocity and impact to occur perpendicular to the surface. If the distribution of the actual impact velocity, as well as the distribution of impact angles would be considered in the analysis, the required thickness to withstand most strikes could be significantly less.

Therefore, DRAMA is utilized, which is a software developed by ESA for the purpose of identifying the damage occurring to surfaces in particular orbits and orientations in space, due to space debris and meteoroids. For this verification, the MIDAS Impact flux and damage analysis tool shall be used. The software utilizes the MASTER environment to setup the MMOD environment. MASTER uses several models such as the Divine Staubach meteoroid model to provide an estimation of the MMOD flux. For the damage analysis ballistic equations such as Jenniskens-McBride or Cour-Pallais are used to determine the damage based on an earth oriented/sun fixed/inertial fixed surface with a predefined area thickness and density. The MMOD and debris environment is then analyzed for possible damage resulting from the impact. A simulation is performed based on the year 2009 and selected are all debris sources and meteoroid sources. The meteoroids streams are based on the Jenniskens-McBride model and the orbit selected is GEO. The software also offers a prediction of debris to the year 2055. However, since the probability that a puncture is formed during the first year is very high, it is not analyzed over a longer period of time. The exposed cross section which is should be chosen is based on the exposed surface of the tube, unfortunately DRAMA only allows a minimum cross section area of $A_{cross} = 0,05 m^2$. This corresponds for a Sphere with $A_{surf_{sphere}} = 4A_{cross} = 0,2 m^2$ and for a tumbling plate with $A_{surf_{plate}} = 2A_{cross} = 0,1 m^2$. Hence the exposed area is much larger than that of the exposed area of the tube. The results of the analysis plotted and are provided in Appendix F: DRAMA results. The probability of collisions reverse cumulatively are read from the graphs and the values observed are shown in Table 24. The probability values are therefore to be taken with an error of $\pm 0,1$. The dates which are used to model the probabilities are also shown in the same table.

Table 27: Probability of collision between MMOD and randomly tumbling plate or a sphere with $A_{cross} = 0,05 \text{ m}^2$ in GEO analyzed by DRAMA and the date settings of the model

Particle mass (kg)	P(col) Plate			P(col) Sphere		
	1 Week	1 month	1 year	1 Week	1 month	1 year
$m > 1 * 10^{-9}$	0,004	0,02	0,1	0,01	0,1	0,6
$m > 1 * 10^{-12}$	0,09	0,8	1	0,4	1	1
$m > 3 * 10^{-14} (= m_{min})$	0,6	1	1	1	1	1
$m > 2,2 * 10^{-15}$	0,7	1	1	1	1	1
Dates	From	To				
Week	2009/06/01	2009/06/08				
Month	2009/05/01	2009/06/01				
Year (reference setting)	2009/06/01	2009/06/01				

DRAMA determines that the probability of the surface being punctured during the first year to be one. The mass which is capable of penetrating the tube would penetrate the targets within a week. However, this is also the result of the larger areas of the simulated targets. $A_{surf_{sphere}} > 4A_{tube}$ and $A_{surf_{plate}} > 2A_{tube}$.

The analysis can at this stage be continued, however additional settings are required such as FR orientation and size. Since these settings also may have a great impact on the results of an actual mission, it is recommended to perform this additional simulation.

If the options are considered of scaling the FR and or performing risk mitigation by redundancy, it can be quickly identified how the results change. The probability of a collision is based on an exponential distribution, which has the memoryless property. Furthermore, there may be two surfaces of the same size tumbling in space with the same probability of being hit by a meteoroid, these events are independent. The probability of both surfaces being struck during a week, month or year, is therefore predicted first order by:

$$P(A_1 \cap A_2) = P(A_1) * P(A_2) \quad (4.5)$$

The impact that the scaling or making the system redundant has on mitigating the risk of a collision by eq. (4.5) are shown in Table 28.

Table 28: Probability of a collision of MMOD with mass m_{min} , with the FR tube related to exposure time

Exposure time	Probability (Single area)	Probability (Double area)	Probability (redundant loop)
Hour	0,0016	0,0032	0,0000026
Day	0,037	0,073	0,0014
Week	0,23	0,41	0,053
Month	0,68	0,90	0,46
Year	1	1	1

4.4.6. Conclusion

It is determined by first order analysis what the threshold mass of a micrometeoroid is that may puncture the FR. Furthermore, it is identified from the cumulative flux what the probability is of a collision with this particle mass, which is verified by DRAMA software. The outcome is that the tube will be punctured within one year and it is very likely that it will occur during the first month. Furthermore, it is estimated that a stainless-steel tube could eliminate the risk of penetrations by particles which are present in relatively dense populations. To obtain a high probability of survival $P(nocoll_{15years}) = 0,8$, the masses which have to be stopped are found to be $m_{mmod} \leq 10^{-5} \text{ g}$. This would require a tube with a steel wall of thickness $t_{wsteel_{min}} = 0,81 \text{ mm}$ relating to high density particles according to the ballistic analysis. Scaling showed to significantly increase the probability of a collision with a particle, and a redundant loop reduces the probability of collision with a particle of critical mass. The Probability was reduced to $P(nocoll_{month}) = 0,46$, which does not demonstrate a direct solution to the problem. Therefore, a combination of material selection and or wall thickness adaption and redundant loops may provide the solution. However, this may also impact the flexibility of the FR and thus

creates a problem for the selected design. It is in any case wise to make a more detailed analysis since the assumptions which are made are conservative and proper assumptions may lead to much more favorable collision rate.

4.5. Research question elaboration and conclusion

The research questions related to the design description chapter are elaborated here. The main research questions are defined per section and shall also be presented in that order. The chapter conclusion is presented here as well, which relates to the answers to these questions as well as the content of the chapter.

RQ 4.1: “What is a feasible radiator design for INFRA that may potentially fulfill the main system requirements, and which tubing type and interface should be selected? Are there additional systems required to support the functionality of the FR?”

A 4.1: The design which may fulfill the requirements is based on a roll able radiator, which can be deployed by means of inflation. Furthermore, the thin walled tubes provide the radiator with excellent flexibility and sufficient heat transfer capabilities. The radiator materials have also been analyzed and determined to possess sufficient strength for handling and launch. To support the deployment of the radiator several subsystems are designed such as the HDRM, FRRS, FRF. These are designed for the breadboard in Aluminum and utilize several high-tech space ready materials such as Norcoat Liege, Vespel and Dyneema. However, the aluminum construction can be replaced by honeycomb, polymer or composite materials to reduce the mass. A thermal model is created to verify the thermal performance, and a first estimate shows an efficiency of $\eta > 50\%$. Relating to competitive requirements, the system is estimated to have a mass performance of $P_{mass} = 15 W/m^2$ in the lab, and $P_{mass} = 6 W/m^2$ in space. Of which the latter is representative and which would fulfill the requirement. The only obstacle of this design, which is not relevant for the breadboard demonstration, but which can reduce the lifetime are the possibility and probability of a meteoroid puncturing one of the tubes. It is estimated that the FR will very likely be punctured within a month in GEO. This does affect the position between other deployable radiators on the market and a design update to reduce this effect is recommended. The question related to which tube to select, is also based on requirements which are working against each other and thus require a tradeoff. One the one hand, the radiator must be of low mass and inflatable, on the other hand it must be able to survive MMOD during 15 years in space. The actual risks with respect to orientation of the FR in space should be more carefully simulated and it may yet be required to perform a design update of the tubes. However, what the effect on the deployment and the thermal performance is cannot yet be predicted. The thermal and deployment performance is to be verified by tests in chapter 5, however potentially the design can fulfill these requirements, which are also the most important for the technology demonstration.

RQ 4.2: “How can the FR be modeled such that its performance in the lab test as well as in Space can be predicted and which error can be accomplished? Is this error reasonable?”

A 4.2: When modelling the behavior of the radiator in a lab environment and in space, the deployment dynamics and the thermal performance can be considered. Since zero gravity tests are relatively simple to perform, it is chosen to develop a thermal model which can be used to predict the radiators performance in various environments. The thermal model is only setup to provide an initial estimation. After the test, the model can be correlated and become more accurate. There are influences in the test which may significantly affect the results. Such as the unpredictable/unstable natural convection and/ or varying room temperatures. Based on these factors it is accepted and expected to encounter large offsets during the lab test, however the maximum offset should not lead to the exceedance of the requirements. Since the model was verified against the 2D HiPeR model, it is expected that the calculated performance offset in space will be low ($< 10\%$ of Q_{tot}) which is sufficient to comply with the requirements.

RQ 4.3: “Which parts of the design must be analyzed to verify the system requirements and which cases are critical under the identified load cases?”

A 4.3: All the parts which are loaded during handling and launch must be analyzed to verify the structural requirements since these cannot be tested. Summarized these parts are the FR, FR connection strips, FRF compression, HDRM lever, thread and tension hat, FRRS rollers and bar. The critical locations of these parts are identified in the subsequent chapter sections. Not a single location is regarded critical under the loading conditions, however it should not be attempted to place pretension on the thread of the HDRM, by rotating the tension hat by more than four pin holes.

RQ 4.4: “How large is the risk that MMOD poses to INFRA and what is the life expectancy of the current design? How does this compare to a metal tube design?”

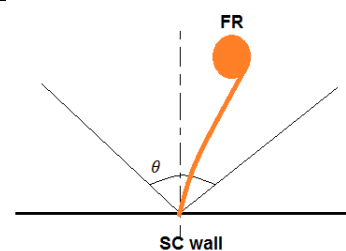
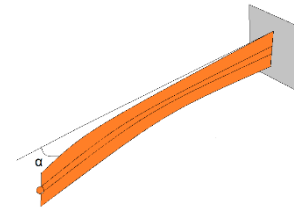
A 4.3: This question is already partially answered in A 4.3. A metal tube may increase the life expectancy based on the thickness and material properties of the metal. A wall thickness of $t_w = 0,81 \text{ mm}$ of stainless steel may reduce the probability of a collision with a critical mass during 15 years in GEO to $P = 0,2$.

5 Test setup and results

In this chapter the deployment, bending and thermal test shall be elaborated. The deployment and the thermal test were performed in two sets. Due to careful planning several valuable tests could be performed which tested the limits of the breadboard model and which were also used to monitor changes in its performance. The tests sequences can be found in Appendix G: Test planning. The first test sequence included only the FR and the second tests included also the PA. A distinction is made to identify individual functionality and combined functionality, but also to make sure that issues are resolved before integrating the subsystems into the RS. In the following sections both test setup and the results shall be discussed. In the thermal test chapter also, a correlation with the thermal model shall be provided and in the final section the research question is answered. The requirements which are verified in this chapter are shown in Table 29.

Table 29: System requirements and verification methods

Requirement ID	Requirement specification	Method
INFRA-prop-0002	Following a single (set of) commands, the INFRA BB shall manage the transition from stowed to deployed condition. This is a one-off operation, re-stow is not foreseen. Manual re-stows should be possible without degrading the hardware	T
INFRA-prop-0006	The FRA shall demonstrate a mass performance of $< 10 \text{ kg/kW}$	A, T
INFRA-BB-SR-5.2.1.10	The FR shall be considered deployed once a steady state at $> 1,5$ bar absolute internal system pressure is reached and also a deflection angle $\alpha < 30^\circ$ of the tubing is obtained	T
INFRA-BB-SR-5.2.2.1	The RS shall dissipate the heat loads as described in UCS32 by means of cooling as described in UCS32, without exceeding the max root temperature of 50°C , as measured on the wall of the tube at the fluid entrance of the FR	A, T
INFRA-BB-SR-5.2.3.1	The PA shall be able to provide a fluid volume flow of $1 \text{ l/min} \pm 10\%$	T
INFRA-BB-SR-5.2.6.2	The FR shall demonstrate an overall radiator efficiency of $50 \pm 10\%$	A, T
INFRA-BB-SR-5.2.7.1	The bending stiffness of the radiator cross section shall be low enough such that the FR can be stowed and inflated with a stowed volume of $0,016 \text{ m}^2$	T
INFRA-BB-SR-5.2.7.2	The FR shall not deflect more than $0,5 \text{ m}$ during UC2	T
INFRA-BB-SR-5.2.7.5	The FR shall deploy within $2\theta=90^\circ$ cone from the rolled up/stowed starting position:	T
INFRA-BB-SR-5.2.9.3	The electrical HDRM shall be able to release the stowed foil within 2 minutes after initiation	T



5.1. Deployment test

In this section the deployment tests are described. During these tests a number of requirements are verified by means of the following actions: After stowing the FR [INFRA-BB-SR-5.2.7.1] is verified by measurement of the packed volume. [INFRA-BB-SR-5.2.7.5] is verified by means of video images taken with a top view to identify the cone in which it deploys, and [INFRA-BB-SR-5.2.9.3] is verified by performing the electrical deployment within the provided time. Several thread-cutting tests are performed beforehand and demonstrate that the resistors function without showing signs of degradation. The verification of the deployment status is performed by measuring the deflection and monitoring the pressure during and after deployment [INFRA-BB-SR-5.2.1.10].

5.1.1. Test setup

The first deployment test is performed without the PA and therefore the test is executed by means of pressurized air. By releasing the FR, the deployment initiates as a result of material stresses. Afterwards the pressure is slowly increased. The tubing is connected to an improvised interface to the available pressure source in the test facility. The optical table which is used to perform the deployment on is perfectly flat and therefore it is perfect for the pressurized air bearings which perform very well under 5,5 bar pressure gauge. It is however a few centimeters too small and therefore a platform is used to act as limiter at one side of the table to prevent the FR from falling over the edge. A pressure valve is used to provide the required pressure for the radiator as well as the air bearing pressure. The deployment is HDRM installed only on the top side to prevent the hover disk from making contact with the lower HDRM. Due to the longer than required bearing/bolts it was impossible to leave the lower HDRM in place. However, it is not expected to be influential to the deployment and thus on the test results. The deployment is performed mechanically to demonstrate the reaction of the FR. The functionality of the HDRM is tested individually. The deployment is observed by a top view camera and the FR is rolled up which can also be seen in Figure 77. The grid on the optical table contains a 2,5 cm spacing which is used to measure the deployment angle. The accuracy of this measurement is $\pm 1 \text{ cm}$, however this is not restraining verification of the results. While the FR is rolled up, only slight pressure is required to flatten the tube. While connecting the FRRS with the HDRM, it is very tempting to apply some extra torque to tighten the fitting. However, this may have caused a leak in the tube afterwards as a result of local stress buildup in the tube. Luckily this occurred at the end of the FR tests such there was some time to repair the tube. For the RS (FR+PA) test, the setup is the same, however one single base of the support structure is taken away to not hinder the deployment. The pressure which is produced by the PA is also constant, however the buildup of pressure is slower due to the slow heating up of the accumulator and the applied pressures are now lower. Before the leak a max pressure gauge was tested of 3 bars for the full FR. The tubing plus connector is tested until 5 bars. However, after the repair only 1,5 bar gauge pressure is used, which is sufficient to fulfill the requirements.

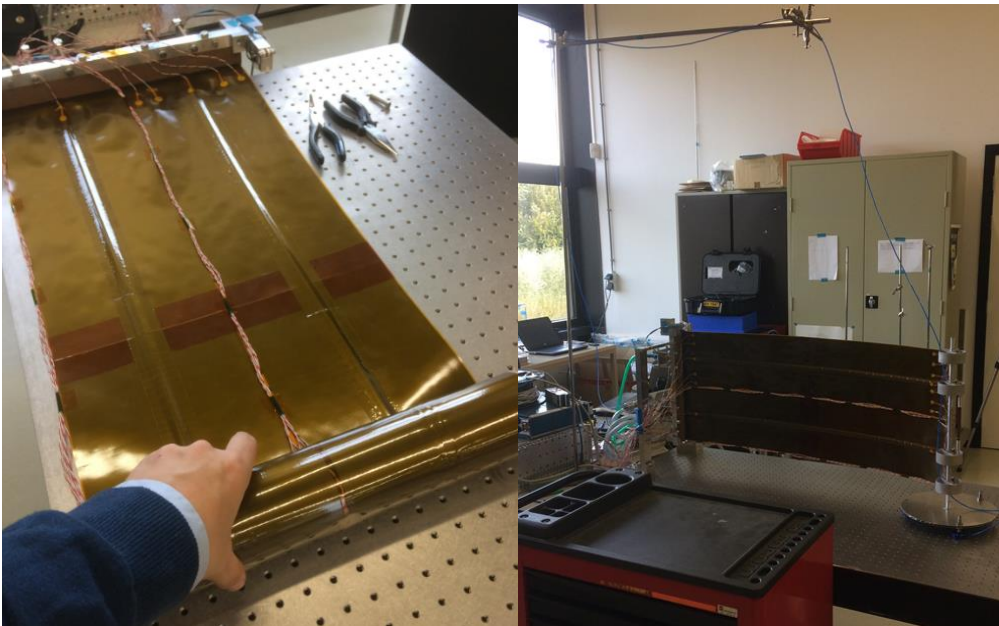


Figure 77: Rolling up the FR (left), deployment test setup (right)

5.1.2. Results

The deployment tests were successfully performed. A total of ten attempts was performed to demonstrate full functionality according to the following requirements of which the observations which have been made can be seen in Table 30. The requirements which are satisfied in this test are: The FR shall be considered deployed once a steady state at $P_{abs} > 1,5 \text{ bar}$ internal system pressure is reached and also a deflection angle $\alpha < 30^\circ$ of the tubing is obtained [INFRA-BB-SR-5.2.1.10] and The FR shall deploy within $2\theta = 90^\circ$ cone from the rolled up/stowed starting position [INFRA-BB-SR-5.2.7.5]

Table 30: FR test observations and deployment verification

Attempt	Observations	Req verified?
FR-d1	Unsuccessful deployment: Hover disk entangles with air bearing tube, deployment unpressurized	No, No
FR-d2	Unsuccessful deployment: Hover disk entangles with air bearing tube, which restrained the FR while deploying	No, No
FR-d3	System pressure 2 bar abs ; final deflection angle is $11,3 \pm 0,6 \text{ deg}$: Air bearing tube is placed through FRRS center. FR lower thermocouples hits one of the bearing bolts which stopped the deployment. One of the air bearings hit the deployment structure. After a few seconds it deployed however launched itself to the edge of the table. After lifting the outer air bearing back on the table, a low deflection result is obtained. FRRS center exceeds the conical bounds.	Yes*, No
FR-d4	System pressure 2 bar abs ; final deflection angle is $7,12 \pm 0,6 \text{ deg}$: A restraint was placed next to the table and successful deployment was observed. It slightly touches the restraint however is not expected to deploy differently on a larger table. FRRS center hits the conical bounds, however does not exceed it.	Yes, Yes
FR-d5	System pressure 2 bar abs ; final deflection angle is $8,5 \pm 0,6 \text{ deg}$: Violent deployment, hits the support twice as well as the table restraint. Does not exceed conical bounds.	Yes*, Yes*
FR-d6	System pressure 2 bar abs ; final deflection angle is $7,8 \pm 0,6 \text{ deg}$: No restraint, instead additional table is used. Hits the support while deploying and stops rotating, slides over table and stops due to friction on curved table. Completes deployment after gentle push. Exceeds conical bounds.	Yes*, No
FR-d7	System pressure 2 bar abs ; final deflection angle is $8,5 \pm 0,6 \text{ deg}$: Completely deploys however hits the supports and is stopped by friction between bearing and additional table. Exceeds conical bounds.	Yes*, No
FR-d8	System pressure 2 bar abs ; final deflection angle is $8,5 \pm 0,6 \text{ deg}$: Deploys aggressively, hits support but deploys completely. Does not exceed conical bounds.	Yes*, Yes*
FR-d9	System pressure 2 bar abs ; final deflection angle is $< 11,3 \text{ deg}$: Deploys well, does not hit support, video stops before final position is obtained. Slightly exceeds conical bounds.	Yes, No
FR-d10	System pressure 2 bar abs ; final deflection angle is $< 4,3 \text{ deg}$: After repairs: Obstructed three times during deployment, video stops before final position is obtained. Exceeds conical bounds due to thermocouple entanglement and resulting springiness.	Yes*, No

* Requirement verified according to specification, however obstructions were present

Test d4, d5 & d8 verify both system requirements. Only test d4 did so without obstructions during the deployment. Since the obstructions always resulted in aggressive and unpredictable behavior, it is assumed that if the obstructions were not present, the requirements would be met for the majority of the tests. For the RS tests, the supports which are obstructing the deployment are taken away. The RS deployment test setup is shown in Figure 78. Results can be found in Table 31.

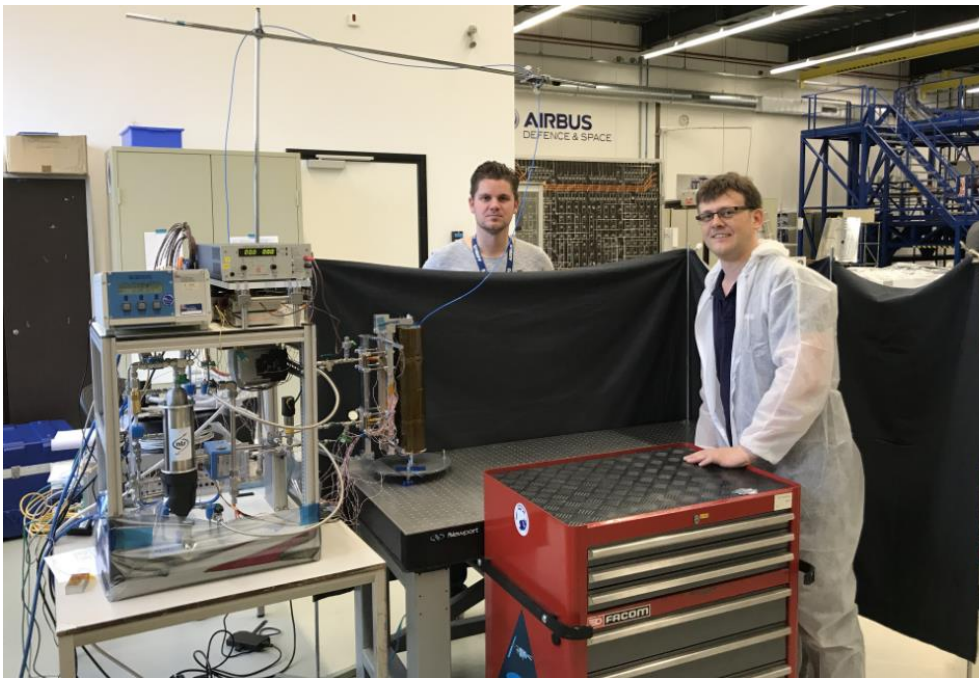


Figure 78: RS deployment test setup

Table 31: RS test observations and deployment verification

Attempt	Observations	Req verified?
RS-d1	$\alpha < 2^\circ$ final angle practically straight at 2 bar absolute pressure: Smooth deployment due to 0,3 bar gauge pressure before deployment, slightly influenced by table boundaries	Yes, No
RS-d2	$\alpha < 3^\circ$ final angle practically straight at 1,4 bar absolute pressure: 0,5 bar initial gauge pressure caused slightly aggressive deployment resulting in obstruction during unwinding and large swing after release	Yes*, No
RS-d3	No deployment: Electrical deployment failed due to defective voltage source, after switching source this was solved	No, No
RS-d4	Successful deployment however uncaptured by video image. Some obstructions were again observed in the thermocouple wires and the bearing bolts	Yes*, No

Four deployment tests are conducted. The hover disk slightly touches the table boundary support during the first attempt. A slight exceedance of the conical area was also observed. The FR tests did however demonstrate one fully verified deployment and two deployments which were fully verified but were obstructed. Therefore, it is considered that the requirements are verified however, it should be taken into account that during future tests the thermal couplings should not be able to interfere with the hover disk, it is very likely that initial pressure will lead to a wider deployment exceeding the conical area and that it would wise to use a larger table and use a single deployment support leg, to have a truly unobstructed deployment. Therefore, it is recommended to not pressurize the system before deployment or perform additional tests to identify the perfect pressure for a smooth deployment.

5.1.3. HDRM electrical release test

The [INFRA-BB-SR-5.2.9.3] requirement is verified in this section by means of several independent tests. Since it takes some time to prepare the HDRM, the deployment is performed manually instead of electrically during the FR and RS tests. A single attempt was made during RS-d3, however due to incorrect preparations this did not proceed as planned. Therefore, the verification is performed based on the results from independent test results. The first test which succeeded was performed on a thin Dyneema thread which according to the manufacturing fact sheets [49] has a melting temperature between $152 > T_{melt} > 144$. The second test is performed on thicker thread of a different type, which also has a higher tensile strength, although the melting temperature is the same. Both tests can be seen in Figure 79. The first setup on the left in this figure was used to identify the best resistor to melt the thread. The selection process regarded aspects of the resistor such as reliability, allowable temperature range and shape. Preference is given to concave cylinders since these centralize the thread on the resistor. The tests on the right shows how the thicker wire is cut by means of the selected resistor.



Figure 79: Dyneema thread thermal knife cutting tests

The results of the thick wire cutting test are found in Table 32. By slowly building up the voltage, a melting point is identified.

Table 32: HDRM thread cutting results

Test #	U (V) (measured)	I (A) (measured)	R (Ω)	P (W)	Time (min:sec, start to end)
Knife 1	1,8	1,68	1,071	3,024	Not cut
Knife 2	1,8	1,70	1,059	3,06	Not cut
Knife 3	1,9	1,76	1,079	3,34	1:38 - 2:06
Knife 4	2,0	1,85	1,081	3,70	1:15 - 2:05
Knife 5	2,2	2,04	1,078	4,49	0:50 - 1:13
Knife 6	2,2	2,05	1,073	4,51	0:58- 1:13
Knife 7	2,2	2,04	1,078	4,49	1:17
HDRM 1	3,0	2,78	1,079	8,34	-
HDRM 2	3,5	3,24	1,080	11,20	0:35-0:42

As can be seen in the table, the preliminary tests have demonstrated the functionality of the resistor as thermal knife. During the complete HDRM tests higher voltages were used to reduce the cutting time even further. The lever spring mechanism also worked flawlessly. Since the voltage source was switched off directly after cutting the thread, no damage was observed to the Vespel standoff or to the resistor. The test can be seen in Figure 80.



Figure 80: HDRM test

In the end, it can be stated that all the requirements of the complete deployment tests are verified. There were some limitations on the deployment. This was caused by the structural supports and the size of the table. However, some smooth deployments were observed during the FR as well as the RS tests which ended in the proper angle and pressure. The FR demonstrated several deployments within the conical bounds and the pre-pressurized RS system demonstrated slight out of bound deployments, probably due to the pressure which was provided before the deployment since the FR during the air pressured tests, always untangled by its own material stresses since pressure was applied after unrolling, which resulted in a less violent deployment.

5.2. Bending test

The bending test is performed to demonstrate that the FR can sustain the critical maneuvering load which is described in section 3.2.1. and required by [INFRA-BB-SR-5.2.7.2]. This is done by applying a critical bending moment and by demonstrating that the FR does not deflect more than the allowable distance and that it also does not buckle in case this deflection is obtained. The moment which is tested as a result of the design mass is $M_{maneuver} = 0,07 Nm$. The setup is the same as during the deployment test, utilizing a hover disk to perform a frictionless deployment. Furthermore, a setup is produced which can also provide a point load to the FRRS as shown in Figure 81.

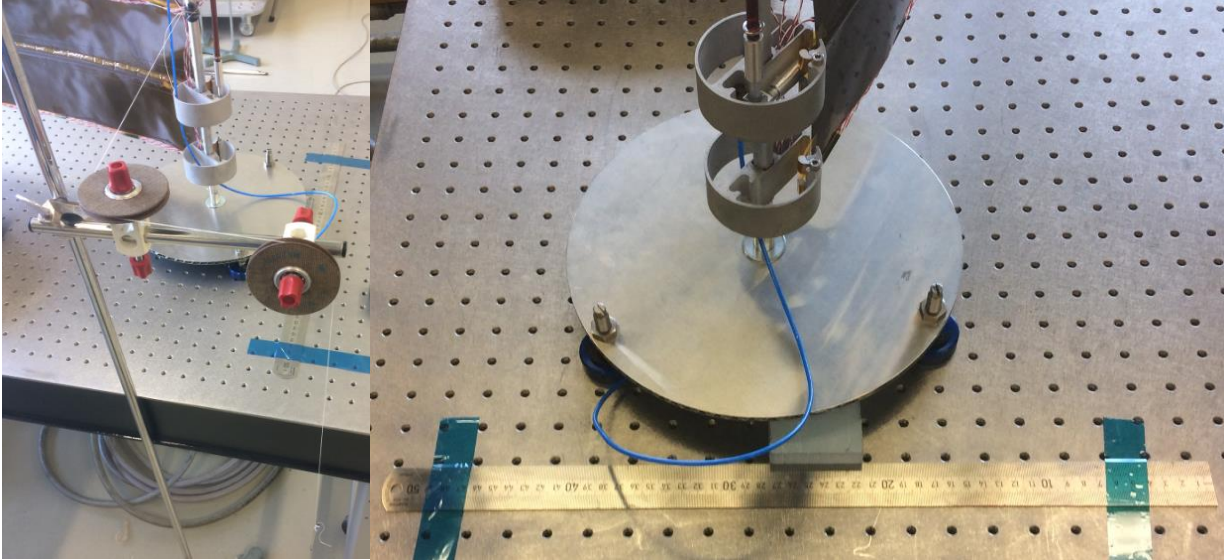


Figure 81: Bending test: point load (left), deflection measurement (right)

In the figure are the point load and the deflection shown. By placing a rectangular block against the heart of the hover disk, the deflection is measured from the start of the ruler. This measurement has an accuracy of $\pm 2 mm$. Air pressures in the tube are set manually and can be controlled with $\pm 0,1 bar$ accuracy.

5.2.1. Bending deflection results

The deflections (δ) during the test relating to pressures (P_{gauge}), loads (F_{bend}) and stiffness (k) is shown in Table 33.

Table 33: Bending deflections of FR tip for various pressures

Bend test #	$P_{gauge} \pm 0,1 (bar)$	$\delta \pm 0,01 (m)$	$F_{bend} \pm 0,001(N)$	$k \pm 0,005(N/m)$
1	0	0,275	0,07	0,254
2	0,5	0,271	0,07	$0,259 \pm 0,005$
3	1	0,254	0,07	$0,276 \pm 0,005$
4	1,5	0,243	0,07	$0,288 \pm 0,005$
5	2	0,219	0,07	$0,320 \pm 0,005$

It can be seen in the table how the deflection reduces with increasing pressure. For the breadboard demonstration a pressure of $P_{gauge} = 1,5 bar$ is used to demonstrate thermal and deployment characteristics. However, it can be noticed that for higher pressures, problems such as vibrations due to maneuvering impulses or stability effects may be solved, by increasing the pressure. A quick test was performed as well to test the response of a bending impulse of an unpressurized FR. An impulse released from δ_{max} showed a settling time of $\pm 12 sec$. Furthermore the damping seemed to be slightly less than critical, a rough eyeball estimation would be $\zeta = 0,4$. A total of two oscillations were required to provide a full stop to its motion and after the first oscillation the FR was within a 2,5 cm band from its final position. However, since there is no pressure in the tube, and since drag on a pendulum has been described to have a damping effect [50], we may assume that damping is largely caused by the drag force of the FR. As a result, the system is expected to have a larger overshoot and a longer settling time in Space. This should be investigated further in the future also in relation with scaling.

We now look at [51] for the relation for the first natural frequencies of a cantilever beam with mass m_{beam} , which has a free end, and an end mass m_{end} . In which E is the Youngs modulus and I_{beam} is the second moment of area.

$$f_t = \frac{1}{2\pi} \left(\frac{y_t}{L_{beam}} \right)^2 \sqrt{\frac{EI_{beam}}{\rho_{beam}A_{beam}}} = \frac{y_t^2}{2\pi} \sqrt{\frac{EI_{beam}}{m_{beam}L_{beam}^3}}$$

Which can be filled in from the cantilever bending stiffness equation

$$k_{bend} = \frac{3EI}{L_{FR}^3} \left(\frac{N}{m} \right) \Rightarrow \frac{y_t^2}{2\pi} \sqrt{\frac{k_{bend}}{3m_{FR}}} \text{ (Hz)}$$

By substituting values for y_t [51] which is dependent on the ratio between the end mass and the beam mass $\frac{m_{end}}{m_{beam}} = 1,6 \left(\approx \frac{m_{FRRS}}{m_{FR}} \right)$; $y_1 = 1,13$, $y_2 = 3,99$, $y_3 = 7,11$, we obtain the first natural frequencies of the FR and FRRS, which can be found in Table 34.

Table 34: First natural frequencies FR+FRRS

Bend test #	$P_{gauge} \pm 0,1 \text{ (bar)}$	$k \pm 0,005 \text{ (N/m)}$	$f_1 \text{ (Hz)}$	$f_2 \text{ (Hz)}$	$f_3 \text{ (Hz)}$
b1	0	0,254 \pm 0,005	0,108	1,346	4,274
b2	0,5	0,259 \pm 0,005	0,109	1,359	4,316
b3	1	0,276 \pm 0,005	0,113	1,403	4,455
b4	1,5	0,288 \pm 0,005	0,115	1,433	4,551
b5	2	0,320 \pm 0,005	0,121	1,511	4,797

To determine if these frequencies pose a problem, further research must be conducted to the dynamic behavior of the FR but also investigate input frequencies which are delivered by the Attitude and Orbit Control System (AOCS). This is however considered to be out of the scope of this report.

5.2.2. Maximum deflection results

An additional test is provided to demonstrate that even in case that the maximum deflection ($\delta_{max} = 0,5 \text{ m}$) is obtained during a step input, the FR does not buckle. To demonstrate this, the base of the FRRS is attached to an Unster, and a deflection of δ_{max} is performed by pulling the Unster perpendicularly to the original longitudinal axis of the FR as shown in Figure 82.

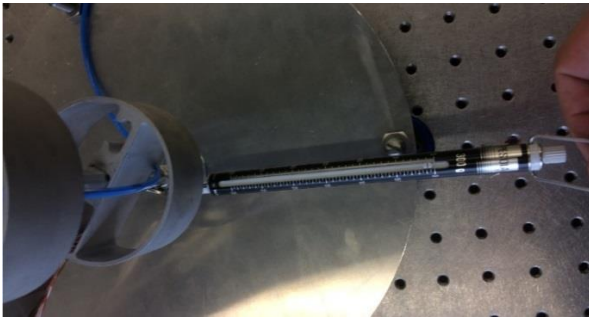


Figure 82: FR is deflected ($\delta = 0,5 \text{ m}$) by means of an Unster

The deflection and the measured loads are shown in Table 35.

Table 35: Maximum deflection test

Bend test #	$P_{gauge} \pm 0,1 \text{ (bar)}$	$\delta_{max} \pm 0,025 \text{ (m)}$	$F_{bend} \pm 0,005 \text{ (N)}$	$k \pm 0,02 \text{ (N/m)}$
b6	0,5	0,5	0,10	0,20
b7	1	0,5	0,14	0,28
b8	1,5	0,5	0,18	0,36

Now it can be concluded that the maximum deflection is not reached during the critical maneuver and that the maximum allowable deflection does not cause buckling of the FR and therefore the system requirement [INFRA-BB-SR-5.2.7.2]

is verified. After releasing the FR from a bended position, the FR obtains a steady state within a few seconds. However, it is not yet identified how the system will behave with respect to more exotic inputs and without drag to damp the motion. The natural frequencies are also provided of the FR, by scaling the size of the radiator, these will change which must be taken into account.

5.3. Thermal balance test

The thermal test is performed to identify the steady state heat dissipation of the system for various mass flows, while demonstrating a performance as described by the system requirements. The Thermal test is performed twice, it is first performed on the FR to test its capabilities and afterwards the RS is tested by coupling the FR with the PA. The reason for performing a FR test individually is to make sure that the setup is capable of collecting the required data and that lessons may be learned which may be implemented before commencing the integrated RS tests. The requirements which are to be verified by these tests are: [INFRA-BB-SR-5.2.2.1], [INFRA-BB-SR-5.2.3.1], [INFRA-BB-SR-5.2.6.2].

5.3.1. Test setup

The FR is connected to an improvised thermal bath, which functions as PA dummy. The PA dummy is made from a large cooking pan, which contains a thermocouple connected to a block of aluminum to measure the temperature of the water, a 1000 W heating element and a 5W aquarium pump theoretically capable of transporting $Q_f = 300 \text{ l/h}$ which has a maximum elevation head $h_{e_{max}} = 0,5 \text{ m}$. The thermocouple and the heater are linked to a PID regulator to maintain a programmable temperature level. The thermocouple indicating the thermal bath temperature is thermally isolated from the metal pan by means of wood and the pump is placed at a proper height such that it provides the required mass flow. The thermal bath and the test setup can be seen in Figure 83.



Figure 83: FR standing setup (left), Thermal bath or "PA dummy" (right)

The mass flow is measured for each test by aiming the return flow hose onto a weighing scale. By measuring the time between which 50 grams is added until 250 g is obtained in the scale, the mass flow can be calculated by taking the average of the five measurements. This is performed to reduce the read off errors from the stopwatch and the scale. A maximum of 250 grams is taken to uphold the water level in the thermal bath such that it does not drop below the pump inlet. For each test a mass flow of $\dot{m} = 8 \pm 0,1 \text{ g/s}$ is found. This corresponds to a heat transfer coefficient estimated $h_{c_{water \text{ lam}}} = 753 \frac{\text{W}}{\text{m}^2\text{K}}$ for laminar or $h_{c_{water \text{ turb}}} = 2160 \frac{\text{W}}{\text{m}^2\text{K}}$ for a turbulent flow. Since the Reynolds number at the connector is estimated $Re_{connector} = 4210$ and throughout the rest of the tube $Re_{tube} = 2652$ the entire flow is expected to be in the transitional/ turbulent flow regime.

For the RS thermal balance test, the PA dummy is replaced with the actual PA, and the polymer tubes are replaced with 1 m long stainless steel braided hoses which are connected by Swagelok's. Since the FR may be moved or reoriented, the requirements included an interface spec relating to the flexibility of the combined system. The PA uses Galden as heat transport liquid, which has different thermal properties than water. However, for a mass flow of $\dot{m} = 27,5 \text{ g/s}$ or $Q_f = 1 \text{ l/min}$ the heat transfer coefficient is comparable to that of the (laminar) water flow which is tested in the FR test, $h_{c_{galden \text{ turb}}} = 767 \frac{\text{W}}{\text{m}^2\text{K}}$. The heat outputs of the FR and the RS tests are therefore compared.

The thermocouples are of type-T and are placed on the FR before the first test. The expected measurement error at room temperature is $\Delta dT = 0,1 K$. The placement and numbering of the thermocouples can be seen in Figure 84. T-01 indicates the inflow connector and thermocouple T-05 and T-12 are placed on the rear side of the FR to measure the temperature on both sides of the tubing interface to measure the difference between the main laminate and the tube cover laminate. The steady state criterion is required to be $\frac{dT}{dt} = \frac{0,1deg}{30min}$ for vacuum tests, however due to the presence of natural and maybe even forced convection caused by the building's air conditioning and by individuals walking by the FR in proximity of a few meters to the FR during the tests, fluctuations in the data were observed and the steady state criterion could not always be met. Therefore, steady state criteria are taken from the test data at the most favorable or steady moment.

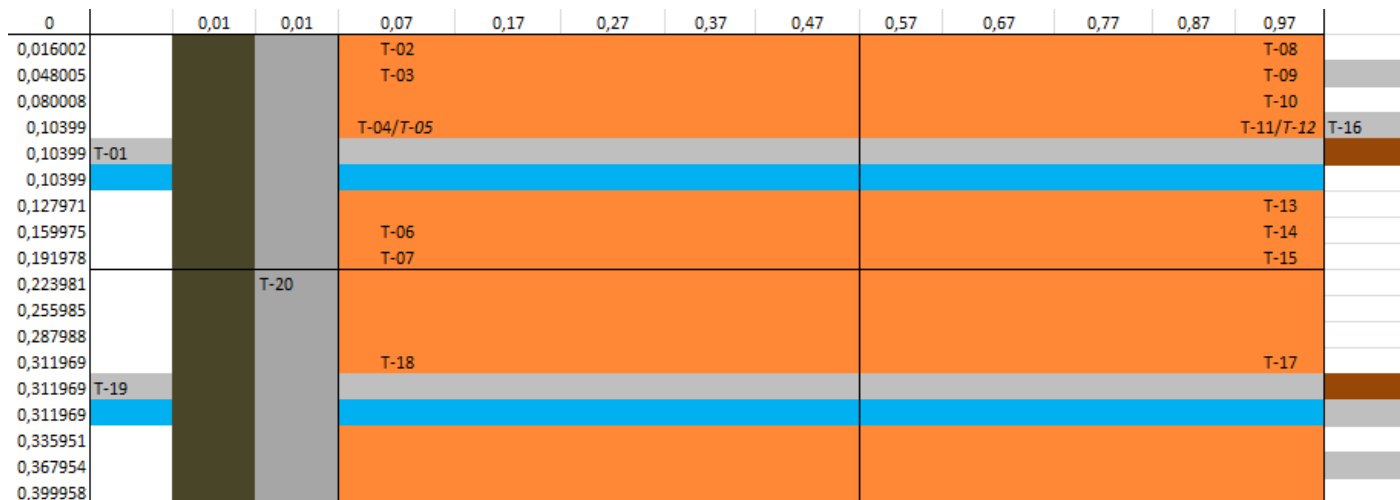


Figure 84: FR Thermocouples number and location

5.3.2. Test results FR

The data which is obtained from the FR tests is shown in Appendix H: Thermal Data. The heat outputs which are measured for the various FR tests and their uncertainties due to the obtained steady states are shown in Figure 85. Especially the higher temperatures have large temperature fluctuations during steady state. The FR is also tested in a lying position; it was suspected that the natural convection influenced the semi symmetrical temperature distribution in a standing configuration however, a lying FR showed to provide a lower heat output and furthermore it is easier to deploy and test the FR in the upright position, therefore it is chosen to continue the tests and model correlation with a standing FR.

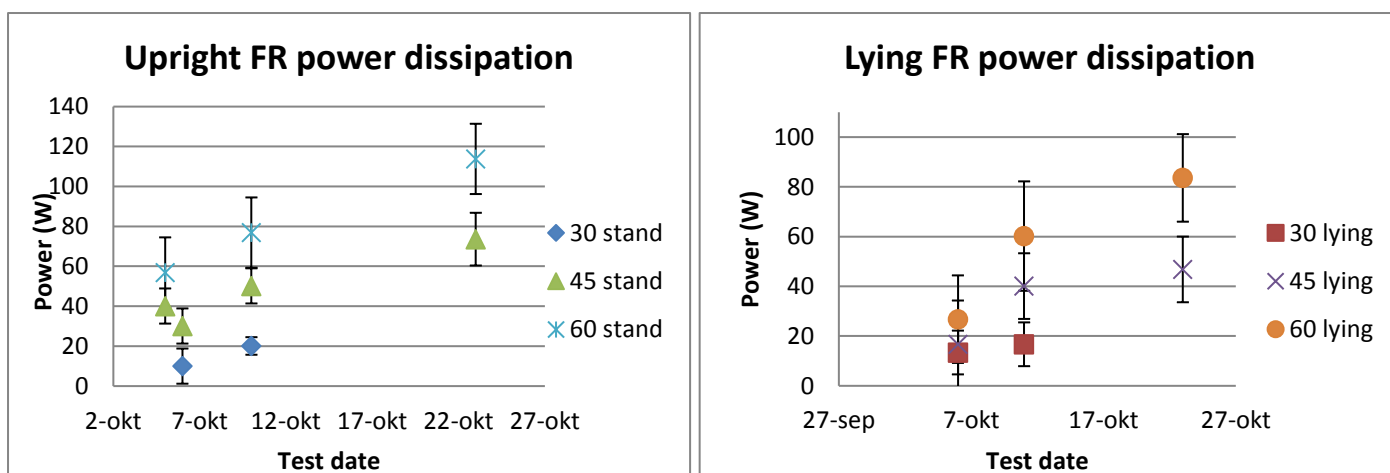


Figure 85: Heat output FR in upright (left) and lying position (right), determined from eq. (2.33)

The performance seems to vary per test date; this may be related to the environmental temperature variations. Since the environmental temperatures were not measured during the FR tests, this cannot be completely verified, however the temperatures which are shown in Table 36 are obtained as zero readings of the FRF and FRRS thermocouples and thus indicate the steady state of the nodes before some of the tests. The temperatures of the other tests are only

available from the time that the FR is already heating up and therefore do not indicate the initial and thus the room temperature.

Table 36: Steady state temperatures measured in the FRF and FRRS thermocouples before the test

Date (time)	Test	$T_{stst} \approx T_{env} (^{\circ}C)$
10-10-2017 (15:22)	Test 2 Stand 30	$22,7 \pm 0,1$
11-10-2017 (12:04)	Test 2 Lying 30	$22,1 \pm 0,1$
23-10-2017 (10:34)	Test 3 Stand 45	$21,2 \pm 0,2$

The difference between the initial and the final temperature of the FRF and FRRS node at the dates of which the temperatures are known is shown in Table 37. After observing the thermostat, it is noted as well that the temperature variation within the test facility on a single day can be $1^{\circ}C$. The lowest temperature is usually experienced in the morning, which slowly increases over the day.

Table 37: Initial and final temperatures of the FRF and FRRS thermocouples during tests with identified environmental temperatures

Date (time)	Test	$T_{startFRF} (^{\circ}C)$	$T_{endFRF} (^{\circ}C)$	$\Delta T (^{\circ}C)$	$T_{startFRRS} (^{\circ}C)$	$T_{endFRRS} (^{\circ}C)$	$\Delta T (^{\circ}C)$
10-10-2017 (15:22-16:32)	Test 2 Stand 30	$22,7 \pm 0,1$	$23,3 \pm 0,1$	$0,6 \pm 0,2$	$22,7 \pm 0,1$	$23,9 \pm 0,1$	$1,2 \pm 0,2$
11-10-2017 (12:04-13:13)	Test 2 Lying 30	$22 \pm 0,1$	$23,2 \pm 0,1$	$1,2 \pm 0,2$	$22,2 \pm 0,1$	$24,2 \pm 0,1$	$2 \pm 0,2$
23-10-2017 (10:34-11:51)	Test 3 Stand 45	$21 \pm 0,1$	$23,7 \pm 0,1$	$2,7 \pm 0,2$	$21,3 \pm 0,1$	$25,5 \pm 0,1$	$4,2 \pm 0,2$

If these temperature differences are held against the final temperatures of the remaining tests, the initial steady state, or room temperatures can be roughly estimated for the other test dates. This is shown in Figure 86.

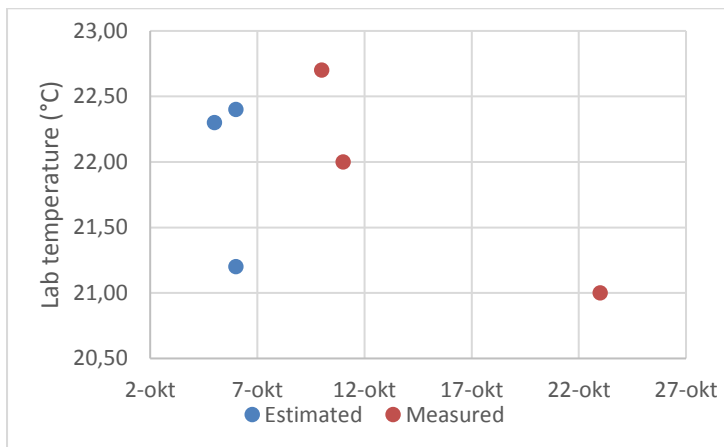


Figure 86: Estimated and measured environmental temperatures during the FR tests

It can be seen that the temperatures which are estimated and measured are much higher on the first 2 test dates than the temperature during the last test date. This could explain why the output of the FR is significantly lower during these days. It is estimated with eq. (4.1) & (4.2) from a temperature difference in the environment of $\Delta T_{env} = 1 K$ centered at room temperature, that this could already lead to a power output variation of $\Delta Q \approx 8 W$. Since the observed power variations are larger than this number, additional uncertainties may be affecting, such as natural convection and the laminate material response to elevated temperatures. The adhesive which is used to connect the tube is known to increase its adhesive grip after being heated. This may also lead to a slight thickness reduction or conductivity improvement, which however has little impact on the performance. Natural convection is expected to vary; however, it is not exactly known by how much therefore a conservative value of $H_{c_{nat}} = 5 \pm 2,5 W/m^2 K^{-1}$ is considered which affects the output for a $T_{FR} = 30^{\circ}C$ with $\pm 20 W$.

Since the environmental temperature is one of the main factor which could explain the heat dissipation variations, the environmental temperature is measured during the RS test and the natural convections shall be taken into account by correlation with the thermal model. There is one other factor which could be influential as well, that is the shape of the tube. After each deployment test the shape of the tube becomes more ovular as it is pressed beyond elastic stresses in

the tube wall. Furthermore, during the FR tests no additional static pressure is exerted and thus no compensation for this effect is in play. This may cause that the thermal heat transfer improves as the tube becomes more ovular shaped after each deployment test, which is performed in turns with the thermal tests. However, since the RS is pressurized, the effect of the flattened tube is not further investigated. It may however be interesting to do so in case of a tube design upgrade.

5.3.2.1. Correlation of natural convection heat transfer coefficient with FR test data

The FR is build out of two similar fins, each containing one part of the tube. The fins are connected to each other only by means of a thin Kapton layer, which provides thermal isolation between the two fins. Therefore, the individual fins are expected to demonstrate symmetrical temperatures over the width of the fin. Over the length of the fin, in accordance with the fluid flow, the temperature is also expected to reduce as can be seen in Figure 87. In the upper tube at the FRF the fluid is entering and it is exiting on the same side through the lower tube. It can be seen that the temperature (brightness) is gradually reducing over this path which is expected. However, if one compares the brightness directly above the tube and directly below in both fins, it can be noted that the lower halves are more purple (colder) and the upper halves are redder (warmer) this corresponds to a temperature difference of $\Delta T \approx 0,5 \text{ }^\circ\text{C}$ in this image, which uses a root temperature of 45 degrees. This effect becomes more prominently visible if the root temperature is increased which causes a higher gradient over the cross section.

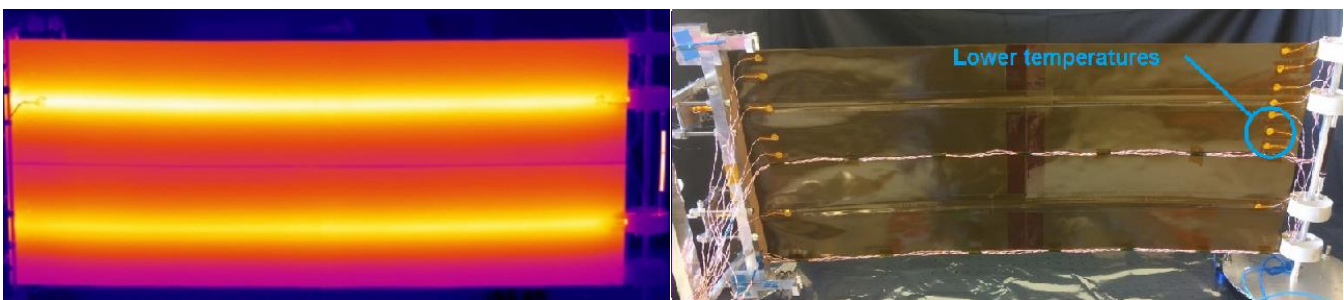


Figure 87: FR IR image during thermal test (left) thermocouple locations (right)

This effect is partially caused by the manual placement and attachment pressure exerted during the manufacturing of the FR. This namely causes asymmetrical contact surface on each side of the tube with the laminate and shows to be repairable by compressing and releasing parts which appear to have a low thermal contact with the tube. However, since the temperatures always appear to be slightly lower on the part below the tube than above, and since the variation is not observed when the FR is placed while lying flat on the table, it is expected to be the result of the thermocouple wire bundles which may disturb the upwards flow of heated air which as a result may cause variations in natural convection over the vertical FR. The parts directly above the bundles would then experience a higher heat transfer coefficient at this location where the laminar flow is disturbed. To model the total heat transfer which occurs per node, the thermal model is correlated with the measured temperatures. This is done by setting the thermal coupling between the tube and the central laminate node as well as the tube to fluid center to infinite. The specific heat is also set very high of the water, such that the temperature of the fluid is the same everywhere in the FR. The inflow temperature can now be adapted to the temperature which is measured at the center node in the test, to exclude the tubing from the correlation. This can be visualized in Figure 88 by connecting T_{fluid} to N_3 directly.

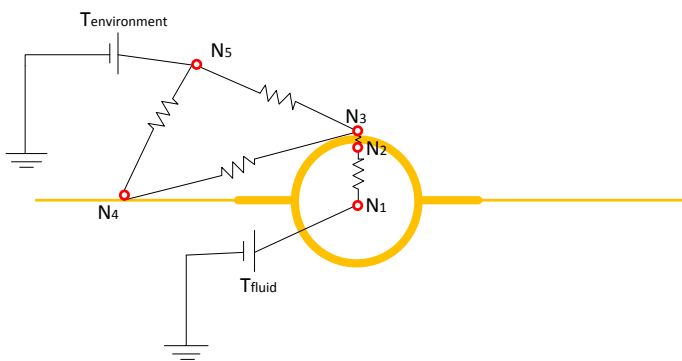


Figure 88: Simplified thermal network of a single FR fin cross section

By setting T_{fluid} to the temperature which is measured at N_3 , the laminate also excludes any uncertainties which are present in the couplings between N_1 and N_3 .

Since there are equivalent nodes in the model as there are thermocouples in the test for this specific cross section, it is easily obtained what the heat flow leaving the surface of the FR is after correlation of the model with the results. The locations of the thermocouples are found earlier in Figure 84. The results of the convection correlation are found in Table 38. It is found from correlation with the FR tests that the overall natural convective heat transfer coefficient can be found between 3,56 and 5,39 W/m^2K . It also appears that node N_{14} & N_{15} have a higher heat transfer coefficient and that the added heat transfer coefficient $h_{c_{added}} \approx 0,4h_c$. Which corresponds to the asymmetry which was observed in Figure 87.

Table 38: Natural convection distribution over measured cross section

	N8	N9	N10	N12	N13	N14	N15
Local function of h_c	h_c	h_c	h_c	h_c	h_c	$h_c + 2 * h_{c_{added}}$	$h_c + 0,5 * h_{c_{added}}$

As discussed before, besides natural convection, another parameter is also directly causing an asymmetry in the temperatures, which is the contact of the tube with the laminate on each side of the tube. Since the model defines the thermal coupling between the N_3 and N_4 (in Figure 88) to be partially based on the contact area with the tube, a tube contact factor is therefore introduced which can be tweaked to match the temperature curve of the cross section. A low contact factor results in a very steep descent of temperature from the center of the tube along the fin, while a high contact factor results in a flatter temperature curve. By tweaking these two parameters the temperature curves can be obtained in the model which demonstrate an overlap of 99% with the tested temperatures. Furthermore, the emissivity of the surface as well as the in-plane conductivity are the only factors which may play role in the correlation with the test data. However, since these are known with the lowest amount of uncertainty (Appendix I: Sensitivity analysis), these are kept as constants while correlating the model. These correction factors and the other factors are shown in Table 47.

Table 39: Nominal settings which are unaltered during the correlation however which impact the cross-section temperatures

Parameter	$K_{pgsip} (W/mK)$	$\epsilon_{FR} (-)$	Interface contact factor left	Interface contact factor right
Value	1400	0,922	1,05	0,8

Lastly, it is found that h_c appears to be higher at the base of the FR. This may be caused by a disturbance of the convective flow by the thermocouples and the FRF. It seems rather illogical that the temperature reduction is caused by the thermal path to the FRF only, since the FRF isolates the FR and thus the FR temperature profile in between the FRF is warmer than the other FR cross sections, which is also verified by the model. This could cause a different heat flow. Another option is that the FRF generates a higher heat leak than expected as a result of its suspension in the metal deployment structure, this is however not included in the model as the effect is expected to be of low influence. These parameters could however at a later stage be implemented in the model to improve the accuracy. The correlated heat transfer coefficients are shown in Table 40. The correlation is performed with the data sets which included an environmental temperature to reduce the uncertainty of the correlation. The correlation shows variations in the h_c at the base of the FR (near the FRF). At the end of the FR (near the FRRS) approximately the same h_c is found for each test. Furthermore, the FR end values are used for the rest of the FR nodes except for the nodes at the FR base since it is assumed that the h_c does not vary between the FR base and FR end due to the absence of additional flow disturbing sources.

Table 40: Natural convection heat transfer coefficient correlated with test data

Date	Location	$T_{env} (^\circ C)$	$h_c \left(\frac{W}{m^2K} \right)$	$h_{c_{added}} \left(\frac{W}{m^2K} \right)$
6-okt	FR base	23,1	6	2,8
6-okt	FR end	23,1	3,9	3
10-okt	FR base	22,7	6,2	2,8
10-okt	FR end	22,7	3,9	3
23-okt	FR base	21,3	4,2	2,8
23-okt	FR end	21,3	3,8	3

5.3.3. Test results RS

The RS thermal tests are performed on two separate days. The temperatures during the tests are measured by a thermocouple which is connected to a cube of aluminum on top of a wooden table next to the experiment to filter small fluctuations. The measured temperatures are shown in Table 41.

Table 41: Environmental temperatures during tests

Date	17-11-17	20-11-17	20-11-17	20-11-17	20-11-17
Time	17:07	12:14	14:33	15:30	16:53
T_{env} (°C)	22	20,7	21	21,1	21,2

Note that on Friday the temperature is one degree higher than on Monday. Variations between the first and the last test on Monday are 0,5 K. The change in temperature over the day is however rather small and can be disregarded during the correlation.

Based on the first order estimation eq. (2.33) and a measurement of the mass flow and temperature difference between the tube in and outlets the heat output of the FR which is obtained during the RS test can be found in Table 42. It is observed that the mean of Q_{out} is reducing with increasing mass flow however that the uncertainty of the estimation is increasing. This result is unexpected since the heat transfer from the fluid should be increasing and thus is the FR expected to dissipate more heat. However, there is a significant amount of uncertainty. The uncertainty of Q_{out} affected by an unexpected measurement error. Since the tubes now have an interface with the PA, the temperatures which are measured at the outside of the tubes are expected to vary with $\Delta T = \pm 0,5 K$. Which results in the observable high uncertainty of the approximation.

Table 42: RS test measured parameters and FR heat dissipation

Thermal Test #	\dot{m} (kg/s)	ΔT_{in-out} (°C)	$c_{p_{T_{av}}}$ ($\frac{J}{kgK}$)	Q_{out} (W)
RS test 1	$0,014 \pm 0,001$	$3,9 \pm 0,9$	$1124,9 \pm 1,5$	$58,8 \pm 14,2$
RS test 2	$0,022 \pm 0,001$	$2,4 \pm 1,0$	$1126,0 \pm 1,6$	$59,4 \pm 24,5$
RS test 3	$0,028 \pm 0,001$	$1,8 \pm 1,1$	$1126,9 \pm 1,7$	$57,3 \pm 32,9$
RS test 4	$0,033 \pm 0,001$	$1,5 \pm 1,1$	$1127,5 \pm 1,7$	$55,8 \pm 39,5$
RS test 5	$0,036 \pm 0,001$	$1,3 \pm 1,0$	$1127,8 \pm 1,6$	$52,8 \pm 40,2$

A different type of hose is used to connect the PA with the FR. This hose is made from stainless steel and is connected to the FR in- and outlet connectors by means of metal Swagelok's. These braided hoses are due to their large surface areas expected to draw a significant amount of power away from the fluid. Furthermore, these are expected to provide a less stable steady state temperature for the FR in- and outlet connectors.

If we combine the temperatures which are found throughout the system we can obtain from eq. (2.33) the heat which is generated by the PA and the heat which is dissipated at the FR. The heat which is generated at the PA is prominently produced by the payload, which utilizes electricity to generate heat. It is found however that the payload generates more heat than which is found to enter the fluid by eq. (2.33). Furthermore, it is found that the payload is generating less heat during the higher mass flows, which is contradicted by the definition of eq. (2.33). Therefore, the pump temperatures are analyzed as well with eq. (2.33), and Figure 89 shows that the pumps are contributing some of the heat which is thus no longer required from the payload to heat of the fluid traveling through the PA. This is especially visible for the higher mass flows, which requires two operational pumps.

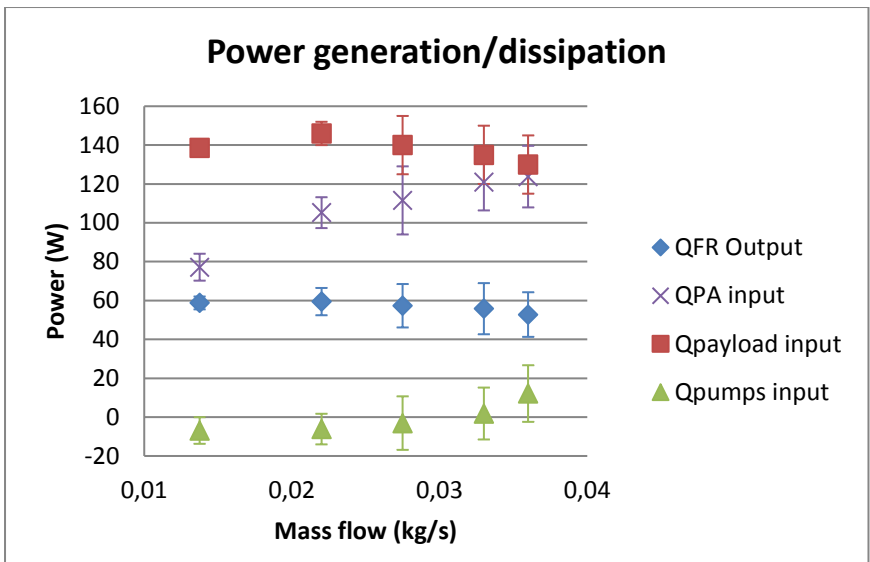


Figure 89: FR heat dissipation during RS test for various mass flows

The temperatures which are measured at the FR in- and outlet, can be seen in Figure 90. It is noticed though that the average temperature of the FR is increasing, which should also result in a higher power output of the FR.

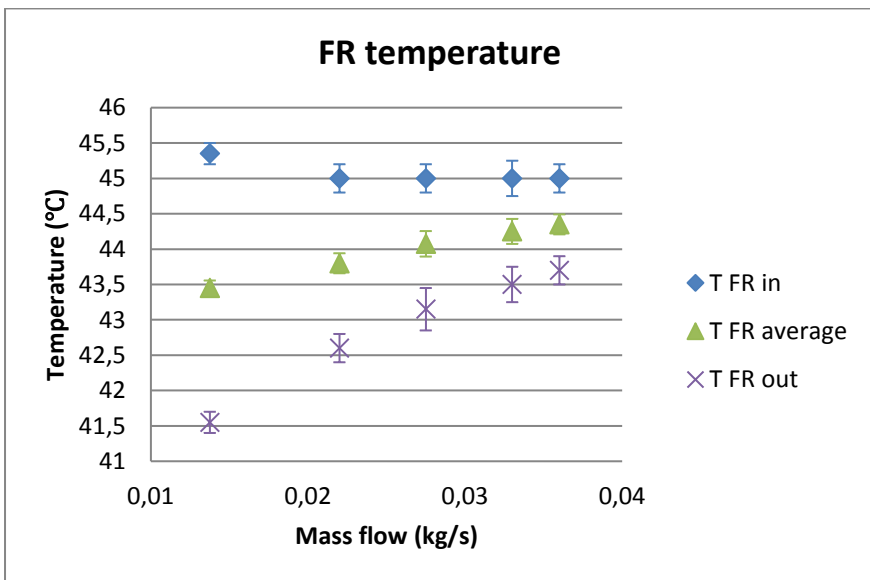


Figure 90: FR measured in- and outlet temperatures

The values which are found in the correlation for natural convective heat transfer coefficient $h_{c_{nat}} = 5 \pm 1 \left(\frac{W}{M^2K} \right)$ plus a radiator efficiency is considered of $50 \pm 10\%$, the emissivity of the FR is set at $\epsilon_{FR} = 0,93$ and the environmental temperatures which are measured during the test, are used to find the first order IR radiative and natural convective heat output of the FR by means of eq.(4.1) & (4.2) to compare the heat which is leaving the fluid eq. (2.33). This is shown in Figure 91.

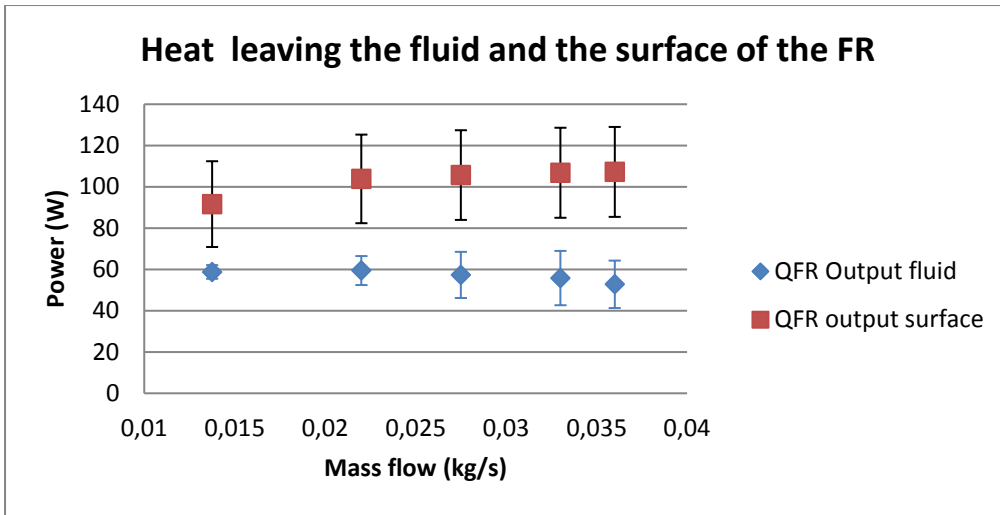


Figure 91: Expected FR surface heat dissipation vs. measured fluid heat dissipation

This also verifies that the heat output of the fluid should be higher than it is measured. Furthermore, it may be the case that the values for \dot{m} , ΔT or $C_{p\text{Galden}}$ are incorrect, however the \dot{m} is measured with high accuracy by a calibrated mass flow meter, and $C_{p\text{Galden}}$ is originally obtained from manufacturer sheet and later confirmed and refined by tests which have been performed by the NLR, hence this is also not expected to have a large offset. To obtain new insights, the thermal model is first correlated with the test data.

5.3.3.1. Correlation of Thermal model with RS test

The correlation of the thermal model with the RS tests focusses on the heat transfer from the fluid to the laminate since the temperatures in the laminate are correlated with the convective and radiative heat transfer to the environment. The thermal couplings which are related to this can be found in Figure 92.

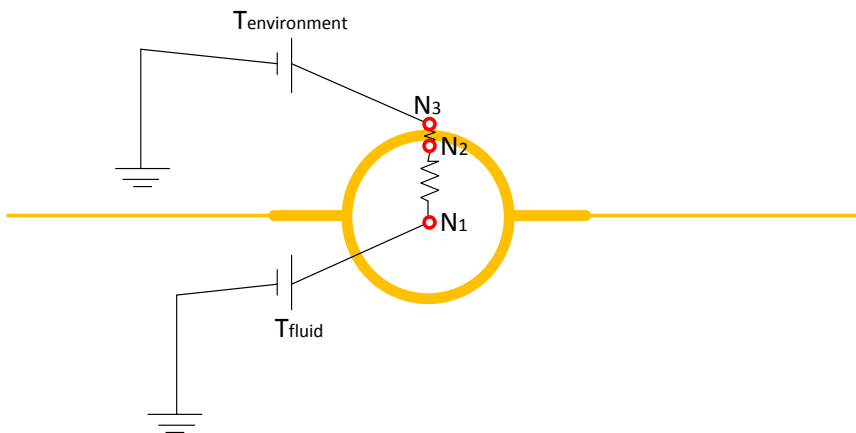


Figure 92: Isolated node 1, 2, 3

The figure also demonstrates that these thermal couplings are being isolated. By setting $h_{c_{nat-conv}}$ to a very high value, the laminate and thus N3 completely becomes the same temperature as the environment. And by setting the environment temperature to the value which is measured at N3 in the test, the thermal couplings can be correlated. The central fluid temperature is linearly interpolated between the in- and the outflow temperature which is measured in the test, taking into account a temperature difference to compensate for the difference between the measured temperature on the outside of the connector and the central flow temperature.

The conductive coupling between N2 and N3 in Figure 92 is assumed to be constant throughout the tests as well as throughout the tube and is estimated based on all layer thicknesses and conductivities plus uncertainties to be

$$Gl_{N2-N3} = \frac{1}{\frac{1}{Gl_{Kapton}} + \frac{1}{Gl_{PGS}} + \frac{1}{Gl_{Adh}} + \frac{1}{Gl_{tube}}} = 1,64 \pm 0,44 \left[\frac{W}{K} \right]$$

If this value is multiplied with the tube nodes, a total value is found of $Gl_{N3-N4FR} = 32,9 \pm 8 W/K$. It is found that based on the heat outputs as obtained from the test, the temperature drops over this thermal path should be $0,55 < \Delta T_{2-3} < 0,62 \pm 0,17^\circ C$ relative to the measured heat outputs.

The other thermal coupling is based on $h_{c_{forcedfluid}}$, which is described in section 2.4.5 and shall also be found by using the temperature differences which are expected between N1 and N3. Since Gl_{N2-N3} is estimated above and the heat output is also known we can find Gl_{N1-N2} from

$$Q_{out} = Gl_{N1-N3} \Delta T_{1-3}$$

$$Gl_{N1-N3} = \frac{1}{\frac{1}{Gl_{N1-N2}} + \frac{1}{Gl_{N2-N3}}} \left[\frac{W}{K} \right]$$

$$Gl_{N1-N2} = h_{c_{forcedfluid}} A_{N2} \left[\frac{W}{K} \right]$$

Based on this approach the heat transfer coefficients $h_{c_{fluid_{est}}}$ which are shown in Table 43 are required to obtain the measured heat output, or in case the expected $h_{c_{fluid_{exp}}}$ are considered, a temperature difference over the fluid of $\Delta T_{1-3_{exp}}$ is expected.

Table 43: Heat transfer related to temperature difference in the interface

Test #	$T_1(^{\circ}C)$	$T_3(^{\circ}C)$	$\Delta T_{1-3}(^{\circ}C)$	$h_{c_{fluid_{est}}} \left(\frac{W}{m^2K} \right)$	$h_{c_{fluid_{exp}}} \left(\frac{W}{m^2K} \right)$	$\Delta T_{1-3_{exp}}(^{\circ}C)$
1	43,52	36,25	7,27	268,63	430	1,80
2	43,84	37,10	6,74	302,10	630	1,81
3	44,15	37,70	6,45	305,24	750	1,75
4	44,19	38,10	6,09	318,37	867	1,70
5	44,47	38,25	6,22	286,61	930	1,61

It can be noticed that either the temperature difference between N1 and N3 and/or the $h_{c_{fluid_{est}}}$ is incorrect. However, since the $h_{c_{fluid_{est}}}$ is much lower than expected and not varying as much as expected as a result of the increasing mass flow, the $h_{c_{fluid_{exp}}}$ is used as a fixed parameter and the model is correlated by varying the temperature at the center of the fluid. To obtain a correlation with the test temperatures, the following results are found. Table 44 demonstrates the required fluid temperature to obtain the observed temperatures.

Table 44: Correlated temperature difference between N1 and N3

Test #	$h_{c_{nat}} \left(\frac{W}{m^2K} \right)$	$h_{c_{nat_{added}}} \left(\frac{W}{m^2K} \right)$	$T_{fluid_{interp}}(^{\circ}C)$	$T_{fluid_{setting}}(^{\circ}C)$	$\Delta T(^{\circ}C)$	$h_{c_{fluid}} \left(\frac{W}{m^2K} \right)$	$Q_{N1-N2} (W)$	$Q_{outFR} (W)$
1	5	2	43,52	46,52	3	430	2,6	52
2	5	2	43,84	46,84	3	630	3,8	76
3	5	2	44,15	47,15	3	750	4,5	90
4	5	2	44,19	46,70	2,5	867	5,2	104
5	5	2	44,47	46,97	2,5	930	5,6	112

The model correlation shows that to obtain the temperatures which are observed in the test, the fluid temperature must be raised approximately $3^\circ C$ above the currently interpolated temperature. It may be the case that the difference between the measured location on the inlet connector is indeed $3^\circ C$ colder than the temperature at the fluid center. Therefore, the model is correlated to an inflow temperature of $\approx 48 (^{\circ}C)$ and the $h_{c_{fluid}}$ is tweaked to obtain the lowest temperature error at the base and at the end of the FR laminate.

In Table 45, the results of the methods are compared.

Table 45: Predicted performance thermal model

Test #	$h_{c_{fluid}}$ ($\frac{W}{m^2K}$)	T_{env} ($^{\circ}C$)	T_{space} ($^{\circ}C$)	T_{av-rad} ($^{\circ}C$)	T_{inflow} ($^{\circ}C$)	$T_{outflow}$ ($^{\circ}C$)	Q_{model} (W)	R_{MS} (K)	R_{SS} (K)	Q_{space} (W)
1	515,5	22	-270,45	32,68	48	42,81	89,8	0,37	1,34	237,8
2	746,6	20,7	-270,45	32,84	47,5	43,82	101,8	0,4	1,38	250,9
3	889,9	21	-270,45	33,33	47,3	44,31	103,7	0,42	1,47	255,86
4	1026,3	21,1	-270,45	33,55	47	44,48	104,7	0,45	1,6	259,1
5	1098,1	21,2	-270,45	33,69	46,9	44,58	105	0,41	1,4	260,4

If we compare the results with the earlier proposed heat output in Figure 91, it can be noted that the results of the model are very similar to the values which are found for $Q_{FR\ output\ surface}$ however it is also much larger than the measured heat leaving the fluid $Q_{FR\ output\ fluid}$. Since it is still strange that the measured heat output is much lower, the test setup is therefore investigated and it appears that the optical table is not considered in the analysis or thermal model. However, it seems likely that there exists radiation exchange between the two surfaces which causes the FR to dissipate less heat. The view factor estimation of the FR to the table is based on Figure 93.

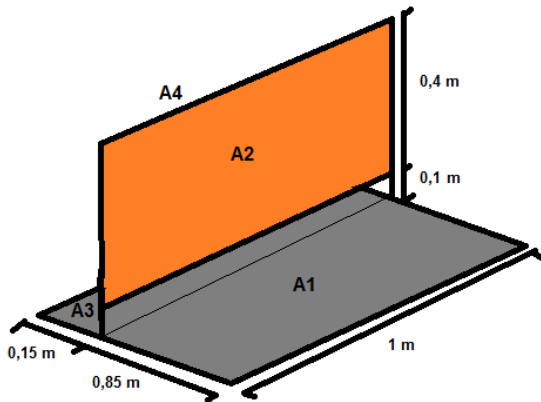


Figure 93: FR area, above optical table area

The radiator surface is slightly lifted from the optical table; however, the table still occupies a significant part of the total view. It is found that the front side and the rear side of the FR have a view factor of $F_{2 \rightarrow 1} = 0,25$, $F_{4 \rightarrow 3} = 0,05$ and the total view factor from the FR to the table is $F_{FR \rightarrow table} = \frac{0,25A_2 + 0,05A_4}{A_2 + A_4} = 0,15$. The emissivity of the table is unknown, however if an emissivity of one is assumed, it can be found that with a Gebhart factor of $B_{FR-table} = 0,11$, a radiative coupling can be formed of $R_{FR-table} = 0,93 * 0,8 * 0,11 = 0,08$, which leads to a heat transfer during the tests of $Q_{FR-table} = 0,08\sigma(T_{av\ FR}^4 - T_{table}^4) < 7W$. Since the table has a surface area of $A_{table} > 2\ m^2$ and in terms of convection will be cooled with $Q_{conv} = h_{c_{nat}}A_{table} > 10\ W$ (not even considering radiation). It seems unlikely that the table will warm up and thus reduce the heat output of the FR over time. The foil which is partially placed onto the table may however have a very low emissivity. This could also cause based on the view factor a reduced heat dissipation by the radiator of maximally 14%.

In the end it seems unlikely that the FR actually dissipated the heat which is measured from the temperatures in the fluid, as the first order approximations and the model demonstrate higher heat dissipation. There are however a number of options which can be causing the discrepancy.

- The heat transfer by natural convection may actually be lower than expected, it requires a natural convective heat transfer coefficient of nearly zero to obtain the same temperatures in all scenarios, which seems unlikely since the test is performed in an airconditioned lab
- The conductive coupling may actually be lower than expected in the tube to laminate interface, however to obtain the estimated heat transfer per node, combined with the estimated temperature difference between the fluid and the laminate, the convective couplings of the liquid to the tube must be between $500 < h_{c_{forced}} < 700\ W$, which could be possible
- The optical table is heating up due to the radiation and therefore the radiator dissipates less heat with increasing mass flows, which seems unlikely since the table has a relatively large surface and is cooled faster by the environment. The table foil may have a very low emissivity, causing the radiator to dissipate less heat.

- The connectors which are coupled to metal hoses by means of Swagelok's may influence the measurement of the temperatures at the FR in- and outlet. As a result, the fluid in the tube is warmer than anticipated and the estimation from (2.33) is highly uncertain. However, to know the exact influence of the hoses more detailed analysis must be conducted, especially since the estimation is very sensitive to small changes in ΔT . It is however estimated with (2.33) and the FR in/out and the PA in/out temperatures that the FR inlet i/f (+ hose) draws 20-30 W and the FR outlet i/f draws 50-70 W from the fluid. This is also strange since the hoses are exactly the same, only the inlet temperatures slightly vary. This indicates that the PA may also influence the PA-inlet temperature by conduction and that as a result the outer tube wall may have a larger temperature difference than expected with the flow, which may be different for the inlet and the outlet hose.

5.3.4. Sensitivity analysis thermal model

A sensitivity analysis is performed on the thermal model by varying the individual parameters by an uncertainty which is reasonable. The factors which provide uncertainty to the model are found in Appendix I: Sensitivity analysis. The results show an absolute worst-case scenario uncertainty of $Q_{FR} \pm 50\%$. However, based on the main uncertainties in the correlated model, the root means square of the surface temperature differences is expected to generate 20 % of uncertainty in the heat output of the radiator in the lab, and even lower in space.

5.4. Research question elaboration and conclusion

The research questions related to this chapter are based on the verification of specific requirements by means of testing.

RQ 5.1: "How to verify the deployment requirements by testing and do the tests verify the deployment requirements?"

A: The deployment requirements are tested and verified by means of 'zero G' deployments, which is recorded by a camera which provides a top view of the situation. This allows measuring of the angles and shows problems during the deployment. This test is successfully conducted providing footage of at least one complete test. Obstructions during the test however were observed many times and for future 'zero G' tests, it is therefore recommended to remove the thermocouples from the FR. A larger optical table is also preferred to guarantee a complete unobstructed deployment.

RQ 5.2: "How to verify the bending requirements by testing and does the test verify the bending requirements?"

A: The bending test is performed in the same position, however with a load connected to the FRRS which simulates a bend maneuver in Space due to propulsive action. Since the hover disk moves almost frictionless, a static load can be produced on the tip of the FR, which causes a bending moment on the root over its lowest second moment of area axis. The obtained stiffness demonstrates the FR's resistance to bending. This is shown to verify the requirement and even provide a margin which can be used to scale the length of the FR.

RQ 5.3: "How to verify the thermal performance requirements by testing and does the test verify the thermal performance requirements?"

A: The thermal test and model correlation are performed on the FR first in combination with a dummy PA and later in combination with the actual PA. This provided the opportunity to observe the FR performance by means of water and also identify any difficulties which could prevent the successful verification of the requirements during the second test. The temperatures which are measured in the laminate indicate an average performance of between $Q_{FR} = 97,5 \pm 7,5W$ for the various tests. The thermal model predicts a maximum space output of $Q_{FR} = 250 \pm 10W$ based on correlations with the lab test. This corresponds to a mass performance of $6 kg/kW$, which easily verifies the requirements. The measured performance is much lower. Considering the worst-case scenario of this being the actual performance of the FR, this would correspond to a mass performance of approximately $12 kg/kW$, which does not directly fulfill the requirements, however by scaling the length of the FRA this number is quickly reduced below the required mass performance. Furthermore, it is expected that the liquid temperature measurement holds a great amount of uncertainty, since the interface to the PA may be lowering the measured temperature, causing an offset in the temperatures which are actually present in the fluid. Based on the model a temperature offset of $\Delta T = 3^{\circ}C$ is expected. However, the model predicts relatively high values for the heat transfer coefficient of the fluid, which may in reality be somewhat lower. Therefore, the actual performance is to be found between the modelled predictions and the measured values. A recommendation for a following test would be to measure the temperatures of the FR surface, but also to measure the temperature of the liquid flow instead of the tube, unless the tube is isolated such that the temperature difference between the tube outer wall and the flow can be predicted more accurately.

6 Verification and Validation

To identify if the project requirements are verified and if the wishes of the customer are validated a summary of all the requirements and the means of complying with these requirements are provided in this chapter. The success of this project is also best explained in the verification and validation (V&V) chapter.

The INFRA projects main goal is to deliver a proof of concept based on the original proposal which was set-up by Airbus and the NLR. To deliver the proof of concept, several aspects or characteristics of the system are discussed with the clients such as size, performance, mass, and operating environment. From this point forward, a system requirements document is provided in which the system specifications are provided in an implementation free analogy. If these guidelines are met, the system is verified, which according to “V-model” terminology should occur continuously during the development of the product from high level to sublevel components. By continuous communication with the stakeholders, their requirements can also be monitored and validated during this process.

In the end a design is produced which is named the Foil Radiator Assembly which is a combination of sub systems which is part of the Radiator System and which is tested in a lab environment and which could operate in Space. Tooling is also developed for the purpose of providing ‘zero G’ deployment and thermal test support. Since these are not operated in space, the requirements for the tooling are more limited and also not discussed in this report. The subsystems which are considered for Space are verified by means of analysis, reviewing, inspecting and/or testing the performance.

In this section, first the system requirements verification is provided and afterwards the validation is elaborated.

6.1. Requirements verification

All the requirements relating to the FRA are verified in the following sections of the report.

Table 46: Verification overview of the FRA

Subsystem	General/materials	Structural	Performance
FRA	Section 4.1/5.1		Section 5.3:
	INFRA-prop-0002 INFRA-prop-0003		INFRA-prop-0006
FR	Section 4.1.1:	Section 0:	Sections 5.1/5.2/5.3:
	INFRA-prop-0018 INFRA-BB-SR-5.2.1.4 INFRA-BB-SR-5.2.2.2 INFRA-BB-SR-5.2.2.3 INFRA-BB-SR-5.2.5.4 INFRA-BB-SR-5.2.7.6	INFRA-BB-SR-5.2.7.4 INFRA-BB-SR-5.2.7.7	INFRA-BB-SR-5.2.1.10 INFRA-BB-SR-5.2.2.1 INFRA-BB-SR-5.2.3.1 INFRA-BB-SR-5.2.3.4 INFRA-BB-SR-5.2.6.2 INFRA-BB-SR-5.2.7.1 INFRA-BB-SR-5.2.7.2 INFRA-BB-SR-5.2.7.5
HDRM	Section 4.1.4:	Section 4.3.50:	Sections 5.2:
	INFRA-BB-SR-5.2.9.2	INFRA-BB-SR-5.2.7.7 INFRA-BB-SR-5.2.7.10	INFRA-BB-SR-5.2.9.3
FRF		Section 4.3.34.3.50:	
		INFRA-BB-SR-5.2.7.7	
FRRS		Section 4.3.40:	
		INFRA-BB-SR-5.2.7.7	

6.2. Requirements validation

The validation of the stakeholder requirements is performed by reviewing the customer requirements and by reflecting on the customer requirements relating to the product characteristics.

The customer requirements are for a large part technically defined in the system requirements. The main wishes of the customer can also be found in the requirements originating from the original proposal. Summarized, the customer

requirements are based on the wish of developing a radiator system which can be inflated and which can transport heat away from a payload to the radiator, such that it may be transferred into space. This radiator system should be based on HiPeR and μ MPL technology. The system is also divided in a PA which is developed by the NLR and a FR, which is developed by Airbus. Additional subsystems may be required to support the functionality of the RS. That means on the lab or in Space. It is expected that the deployment initiation and the heat transfer by the system is controllable and that the system is capable of maintaining its the deployed position. Relating to the latter characteristics, several performance requirements are defined and these are shown to be complied in Table 46. These requirements relate to the deployment initiation by means of a thermal knife, the expected radiative heat output and the critical bending moment which may occur during operation in Space. Parameters which are set for these requirements have been discussed with the customers for acceptability or are demonstrated in section 3.2.1. To meet with the deployment and thermal requirements, a working point is discussed between the project parties, which is based on mass flow and system pressure. Based on this mass flow a pump is selected and also a minimal tube diameter is determined. From these details a rough estimation of the system performance is made and an acceptable mass and size target is set. These factors form the basis of a design which can be operated in a lab environment. However, since the model is intended for use in Space, and the materials which are being used have very specific structural and thermal properties, the best solution to demonstrate the systems operability is to build the breadboard and test it using the actual materials which are in also in the flight model. This also provides an opportunity to perform an announced demonstration which may provide commercial benefits. Based on this project development, the customer requirements are directly addressed and also mostly validated. Based on the customer requirements, system characteristics are defined and weighted in coordination with Airbus. The provided weights are shown in Table 7. The most important characteristics of the breadboard design are defined as Competitiveness, Lifetime, Manufacturability/Handling, Scalability and technology demonstration. Based on these aspects, a small validation analysis is performed.

Competitiveness

The competitiveness of the design is defined in its capability to be stored in a small volume during launch and deploy into a large surface area from which it can effectively dissipate heat. By comparing this functionality with a conventional deployable radiator, it is shown that in terms of storage and comparable performance the design is highly competitive. The performance in space however is estimated based on a single heat source. To demonstrate its actual performance a transient analysis making use of dedicated optical surface properties and additional radiation sources is required.

Lifetime

By making use of materials which can sustain many years in a radiative environment a long-life time is expected. However, based on MMOD analysis it is also discovered that the thin walled low mass design also has a downside, which is its high risk of being punctured by MMOD. It is estimated that the FR will be punctured within the first year of operation. There is even a considerable chance of occurrence during the first month. Risk mitigation techniques such as double loops will however not increase the expected lifespan to the required 15-20 years. Therefore, a design alteration may be required.

Manufacturability/handling

The FR is produced almost completely in-house and all the parts except for the HiPeR laminate are COTS. The same applies for the PA. The handling of the final product can also be performed in most environments such as a workshop or a low caliber cleanroom. While assembling the FR, cleanliness should be taken into account such that the adhesive can be firmly attached to the laminate.

Scalability

The design is perfectly scalable in length and in width within the limits which are provided by the width of the S/C and the stiffness of the FR. By making the tube spacing lower, the stiffness is increased, which allows for a longer FR. Longer fluid lines however also require higher mass flow rates to uphold the average radiator temperature. The laminate can be manufactured in small tiles which can be connected, the tubing however can currently only be procured with a maximum length, this should be taken into account when scaling the FR. Furthermore, reducing the tube spacing also increases the heat output and thus the efficiency. The efficiency which is demonstrated is the baseline model is $\eta = 50 \pm 10\%$

Technology demonstration

It is demonstrated in this project that the technology of an inflatable radiator such as it is described in this report, which is based on HiPeR and μ MPL technologies demonstrates the required characteristics for a competitive and feasible product, however with respect to lifetime it still requires a design upgrade.

All the customer requirements except for the lifetime of the product are met. Furthermore, a proof of concept is delivered by means of a functioning RS and Airbus is patenting parts of the design. Therefore, the conclusion can be drawn that the results are very satisfactory.

6.3. Research questions elaborated

RQ 6.1: "Are the system requirements verified? What are the consequences of any failure to comply with the requirements?"

A: The system requirements which are presented in this thesis are all verified. Requirements which are not verified are requirements related to the IR imaging of the thermal test and logging of the room temperature during the tests. Information regarding the performance of the FR using water is rather uncertain and more detailed future analysis using the IR images of the FR cannot be conducted. The IR images neither the room temperatures during the FR test were required to determine the RS performance. Therefore, the consequences are insignificant.

RQ 6.2: "Are the customer requirements validated? What are the consequences of any failure to comply with the requirements?"

A: The customer requirements are defined by the most important system/project characteristics, which are competitiveness, lifetime, manufacturability/ handling, scalability and technology demonstration. All these characteristics are applicable to the design except for lifetime. The estimated lifetime of the product as a result of MMOD is much too low and requires a more detailed analysis to determine how the design can be changed to manage this risk. As a consequence, the competitiveness is also affected since the feasibility of the product is less pronounced even though the product presents a competitive product in terms of mass performance. However, an indication is present of the steps which must be taken to also satisfy the lifetime requirement.

7 Conclusion

The FRA which is developed as part of the INFRA project is described in this thesis. The central research question which is posed relating to this development is:

“How to develop a state of the art radiator breadboard, which fulfills the customer requirements?”

The answer to this question is provided in this report by taking the following steps:

- Identify customer requirements
- Develop system requirements
- Propose and build a design
- Provide design verification by means of analysis, testing, review of design and inspection
- Validation of the customer requirements

The customer requirements are based on a couple of main system characteristics, which are: *Competitiveness, Lifetime, Manufacturability/handling, Scalability and Technology demonstration*. Included are the wishes of the customer which can be described in one sentence as an Inflatable radiator system breadboard model, which is composed of HiPeR and μ -MPL subsystems, which can be used to deliver a proof of concept, which can be scaled for different heat outputs, which is a competitive product for the current deployable radiators in terms of mass performance and which can survive 15-20 years in Space.

The system requirements which are established take these wishes into account and provide technical specifications for the performance and functionalities of the system. Requirements such as heat output, deployment time, radiator surface area, but also specifications to protect the system against radiation or to make the system capable of sustaining launch and handling loads. These requirements are explained and analysis is provided to support the requirements.

From these system specifications a FRA design is produced. A concept is chosen of a radiator which is deployed by means of unrolling action. This concept requires several subsystems to function well however scores best on *stowed volume, degradation, complexity, mass and reliable deployment* criteria. The systems which are required to support the FR are: a FRF to hold the base of the FR firmly in place, a FRRS to roll-up the FR and to stow it during launch by placing the FRRS ends in the HDRM. Furthermore, custom made tubing connectors are developed to connect thin walled Kapton tubes and which are also used to interface with the PA. Parts are all completely manufactured and the breadboard model is assembled for testing in a lab environment. For the verification of the test requirements, a thermal model is written and correlated to predict the thermal performance in Space. The model includes the FR, the FRRS and the FRF of which the latter are regarded as losses. An initial simulation predicts a performance of $P_{lab} = 104 W$ in the lab environment and $P_{space} = 255 W$ in Space, which corresponds to a radiator efficiency of 50-70%, which theoretically verifies the performance requirements. Furthermore, an estimation of the lifetime in a MMOD environment is provided. For the estimation a minimum required mass is identified which may penetrate the FR tube and after that a collision probability is generated to identify the lifetime of the FR. The required mass is estimated by an energy equation but also by means of the ballistic limit equation. By comparing various settings, the ESA settings are chosen to be most representative and conservative in determining the lowest capable mass of puncturing the laminate and tube. Taking into account a conservative maximum velocity ($30 km/s$), the lowest particle mass that may penetrate the FR at that relative velocity is found to be of density $\sim 3 g/cm^3$ and mass $m_{min} = 3 * 10^{-11} g$. Based on a first order approximation relating to spatial density of MMOD of the considered mass and higher, it is estimated that the probability of a collision with this fatal particle is $P_{col} = 0,68$ within the first month of operation. It is estimated by means of simulating DRAMA software, that a randomly tumbling plate with cross section area $A_{cross} = 0,05m^2$ or a sphere with the same cross section have a probability of $P_{col_{pl}} = 0,6$ and $P_{col_{sp}} = 1$ of colliding with the critical mass within the first week. However, this is related to the smallest surface area which can be used by the software, and this is two to four times larger than the actual exposed tube area. In the end it may be beneficial to perform a more detailed analysis since the assumptions are conservative and this may lead to more favorable life expectancies. A tube material change is also suggested as it is estimated that a tube with a steel wall of thickness $t_{w_{steel_{min}}} = 0,81mm$ can provide the FR with a probability of no critical collisions during 15 years in Space $P(nocoll_{15years}) = 0,8$, this would stop all masses $m_{mmod} \leq 10^{-5}g$ following to the ballistic limit equation.

The FR is also tested for deployment, bending and thermal performance. The deployment tests occur within the prescribed conditions relating to deployment cone and final deflection and pressure. However, ten attempts are performed and only one satisfied all the requirements. The main reason for all the failures are different kinds of obstructions, it is recommended to remove the thermocouples and or remove the bolts on the hover disk which provides the friction less deployment. Furthermore, the edge of the table is limiting the deployment since the optical table is too small. It is also recommended to use a larger table to witness a full unobstructed deployment. The requirements however are verified and the deployment is considered successful also by the clients.

The bending test is performed successfully and the stiffness which is demonstrated is between $0,25 \leq k \leq 0,32 \text{ N/m}$ for pressures of $0 \leq P_{gauge} \leq 2 \text{ bar}$. This corresponds to deflections which are within the requirements due to the maneuvering load and there is even a margin that would allow almost a doubling of the load. Furthermore, it is demonstrated that the FR does not collapse or buckle while performing the maximum deflection. Therefore, it is considered verified in terms of bending/maneuvering requirements

The thermal tests are used to verify the thermal requirements and to correlate the model with the test setup. It is noticed during the FR test which is conducted with water, that the heat outputs greatly vary for different test dates $\Delta P \pm 20 - 30 \text{ W}$. This may be caused by room temperature variations; however, it is estimated that this would result in variations of only $\Delta Q \pm 8 \text{ W}$. If considering uncertainty relating to natural convection the difference can also be quite significant $\Delta Q \pm 20 \text{ W}$. Furthermore, it is also possible that the tube shape becomes more oval like after each deployment since it is being crushed and not being pressurized from the inside of the tube during the test. This may also increase the heat transfer of the flow. To determine the corresponding natural convection heat transfer coefficient of the lab, the model is correlated with the test data by setting the temperature of the laminate on top of the tube to a constantly measured value and by trying to level the measured temperatures with the model temperatures by changing only the natural convective heat transfer coefficient. The average of the correlated values is $h_c = 3,9 \text{ W/m}^2 \cdot \text{K}$, which corresponds with the expectations. Furthermore, an adaptation factor is introduced to deal with the lower temperatures close to the thermocouple wires. These appear to disturb the natural flow and thus create a larger convective heat transfer locally. The FR in combination with the PA is also tested by means of Galden and it is shown that the increasing mass flows do not per definition generate higher heat outputs as would be expected. The heat which is being added to the system at the payload however is increasing and it is shown that heat is also being partially added by the pumps. The reason for the decreased performance may be related to increasing room temperature, however it seems more likely that the means of measuring the heat transport by means of in and outlet temperatures is not as accurate as expected. The measured heat outputs and expected heat output are $Q_{meas} \approx 60 \text{ W}$ and $Q_{exp} \approx 100 \text{ W}$ and are trailing further apart with increasing mass flow rates. The conclusion is drawn that the low output is probably the result of incorrect measurements. This is possible since the interfaces are coupled with metal tubes which also dissipate a large amount of heat and therefore influence the measured temperature. In the end also, a sensitivity analysis is performed to identify how uncertain the model is. A worst-case uncertainty of 50% is identified, however it is considered more realistic to have an uncertainty of 20%. The expected heat output is found to vary between $Q_{FR} = 97,5 \pm 7,5 \text{ W}$. The thermal model predicts a maximum space output of $Q_{FR} = 250 \pm 10 \text{ W}$ based on correlations with the lab test. This corresponds to a mass performance of 6 kg/kW , which easily verifies the requirements. The measured heat outputs however, are expected to have large temperature variations between the tube wall and the flow. Therefore, it is recommended to measure the temperature within the flow.

The verification is completely performed in the report and a few non-significant non-verified requirements are elaborated in the report. Validation is performed based on the characteristics which are important for the customers. All these are mentioned before in this chapter and are validated except for the life expectancy.

In the end the system is complying with almost each customer requirements and a model is build and demonstrated according to the system specifications. Therefore, the main research question is answered by means of the preceding elaborations however advised is to perform an additional research project into the issues and solutions concerning MMOD.

8 Recommendations

As discussed before in the conclusion, the MMOD issue should be resolved as the life expectancy of the FR is not sufficient for a complete mission in GEO. A metal or another material that would make the tube more MMOD resistant should provide better lifetimes. An additional trade off may be required between thickness, material and mitigation techniques such as redundant fluid loops to maintain the flexibility of the design.

It can be seen in the thermal model that the Kapton tube and foil, but also the adhesive has a large influence on the thermal coupling, relative to the PGS. Thickness or conductivity improvements of these layers would benefit the thermal performance since all the heat enters the FR through the tube interface. The table on which the FR is mounted during the thermal tests may influence the thermal performance. For follow up tests, it is recommended to use a surface cover with high IR emissivity to maximize the heat dissipation of the FR. A vacuum environment however is preferred to reduce uncertainties related to natural convection.

The unpressurized FR seems to improve its performance after a few deployments. This could be related to an oval shaped tube which becomes flatter each time the radiator is rolled up. However, this may also be related to the heating up of the adhesive which is used to hold the individual layers of the *i/f* together. This should however be investigated to be able to properly determine the thermal performance of the radiator. Furthermore, the *i/f* to the PA should be improved from a thermal perspective. The long hoses dissipate too much heat from the fluid and influence the temperature measurements at the entrance.

The permeability of the tubes relating to the operating fluids, leakage of the connectors and outgassing of the tubes are areas which are recommended to be investigated for the follow up design, as these factors will influence the long-term life expectancy of the system depending on the type of tube and fluid which is used.

A dynamic model e.g. using ADAMS is required to model the deployment of the FR and also determine the dynamic response to maneuvers or vibrations in space, where scaling of the FR and tube spacing may offer a solution for the low stiffness.

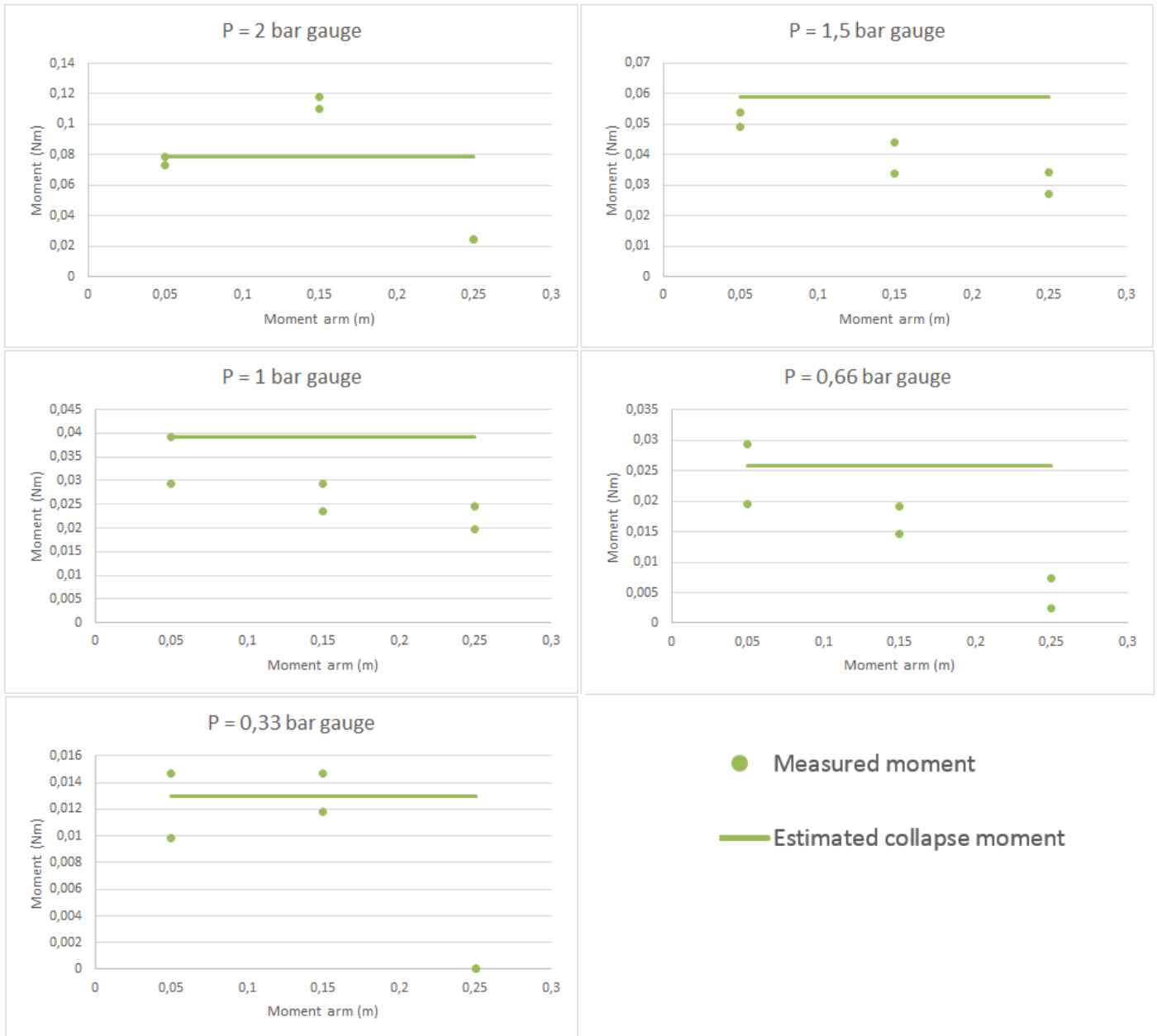
Bibliography

- [1] B. Benthem, "ADSN Internal document: H2020 Space - INFRA part A," Leiden, 2015.
- [2] L. Jacques, "Spacecraft Thermal Control." University of Liège, Liège, 2013.
- [3] P. Poinas, "Satellite Thermal Control Engineering, prepared for SME 2004." ESA, Noordwijk, 2004.
- [4] D. G. Gilmore, *Spacecraft Thermal Control Handbook - Volume I: Fundamental Technologies*, vol. I. 2002.
- [5] D. D. Nguyen, "Analysis and Testing of Heat Transfer through Honeycomb Panels," California Polytechnic State University, San Luis Obispo, 2012.
- [6] S. A. Zirbel, R. J. Lang, M. W. Thomson, D. A. Sigel, P. E. Walkemeyer, B. P. Trease, S. P. Magleby, and L. L. Howell, "Accommodating thickness in origami-based deployable arrays," *J. Mech. Des.*, vol. 135, no. 11, p. 111005, 2013.
- [7] S. A. Zirbel, B. P. Trease, S. P. Magleby, and L. L. Howell, "Deployment Methods for an Origami-Inspired Rigid-Foldable Array," in *The 42nd Aerospace Mechanism Symposium*, 2014, pp. 189–194.
- [8] S. Loff, "Solar Arrays on the International Space Station," NASA, 2015. [Online]. Available: <https://www.nasa.gov/content/solar-arrays-on-the-international-space-station>. [Accessed: 12-Feb-2017].
- [9] C. H. Jenkins, "Overview Of Gossamer Structures," in *Gossamer Spacecraft: Membrane And Inflatable Structures Technology For Space Applications*, Reston, VA: American Institute of Aeronautics and Astronautics, 2001, pp. 1–33.
- [10] Unknown, "NASA - Roll-Out Solar Array," NASA, 2017. [Online]. Available: https://www.nasa.gov/mission_pages/station/research/experiments/2139.html. [Accessed: 09-Feb-2018].
- [11] S. Loff, "Deployment of the Space Station's Roll Out Solar Array Experiment," NASA, 2017. [Online]. Available: <https://www.nasa.gov/image-feature/deployment-of-the-space-stations-roll-out-solar-array-experiment>. [Accessed: 09-Feb-2018].
- [12] Leach and J. W., "Development of an inflatable radiator system. [for space shuttles]," May 1976.
- [13] Unknown, "HiPeR | ESA's ARTES Programmes," ESA, 2017. [Online]. Available: <https://artes.esa.int/projects/hiper>. [Accessed: 09-Feb-2018].
- [14] B. Benthem, "ADSN Internal document: HiPeR EM-1 Test report," 2015.
- [15] J. A. Stevenson and C. Grafton, "RADIATION HEAT TRANSFER ANALYSIS FOR SPACE VEHICLES," 1961.
- [16] G. Fortescue, Peter, Stark, John, Swinerd, *Spacecraft Systems Engineering, Third Edition*. 2004.
- [17] C. Long and N. Sayma, *Heat transfer*. heat transfer, chris long, naser sayma., 2009.
- [18] X. He, Y. Li, L. Wang, Y. Sun, and S. Zhang, "High emissivity coatings for high temperature application: Progress and prospect," *Thin Solid Films*, vol. 517, no. 17, pp. 5120–5129, 2009.
- [19] A. Smets, K. Jäger, O. Isabella, R. van Swaaij, and M. Zeman, *Solar energy: The physics and engineering of photovoltaic conversion, technologies and systems*. 2016.
- [20] B. Benthem, "Satellite Thermal Control Lecture 1: Thermal Environment Optical Properties." TU Delft, Leiden, 2016.
- [21] S. Verlag, "Algebraic Methods for the Calculation of Radiation Exchange in an Enclosure," *Heat mass Transf.*, vol. 7, pp. 31–44, 1974.
- [22] B. Gebhart, "Surface temperature calculations in radiant surroundings of arbitrary complexity—for gray, diffuse radiation," *Int. J. Heat Mass Transf.*, vol. 3, no. 4, pp. 341–346, 1961.
- [23] P. Lindhout, *ADSN Internal document: Thermal control data handbook*. 1986.

- [24] Z. S. Spakovszky, "Unified: Thermodynamics and Propulsion," *MIT OpenCourseware*, 2012. [Online]. Available: <http://web.mit.edu/16.unified/www/FALL/thermodynamics/notes/node117.html>. [Accessed: 07-Feb-2017].
- [25] J. H. Lienhard IV, John H. , Lienhard V, *A Heat Transfer Textbook*, 4th ed. 2017.
- [26] R. Shankar Subramanian, "Heat transfer in Flow Through Conduits," *Dep. Chem. Biomol. Eng. Clarkson Univ.*, vol. 1, pp. 1–9, 2006.
- [27] Unknown, "Galden ® HT PFPE Heat transfer fluids." Solvay, 2014.
- [28] W. H. McAdams, *Heat transmission*, vol. 3, no. 7. McGraw-Hill, 1954.
- [29] R. E. Simons, "Simplified Formula for Estimating Natural Convection Heat Transfer Coefficient on a Flat Plate," *Electronics cooling*, 2001. [Online]. Available: <https://www.electronics-cooling.com/2001/08/simplified-formula-for-estimating-natural-convection-heat-transfer-coefficient-on-a-flat-plate/>. [Accessed: 12-Feb-2018].
- [30] H. CHANG, "Optimization of a heat pipe radiator design," in *19th Thermophysics Conference*, 1984.
- [31] Unknown, "Technical brochure: Dyneema ® in marine and industrial applications." DSM, 2017.
- [32] A. R. Bunsell, *Handbook of Tensile Properties of Textile and Technical Fibres*. Woodhead, 2009.
- [33] J. P. Fay and C. R. Steele, "Bending and symmetric pinching of pressurized tubes," *Int. J. Solids Struct.*, vol. 37, no. 46, pp. 6917–6931, 2000.
- [34] V. I. Weingarten, P. Seide, and J. P. Peterson, "Buckling of Thin-walled Circular Cylinders," no. NASA Space Vehicle Design Criteria NASA SP-8007. 1968.
- [35] S. W. Attaway and D. Ph, "The Mechanics of Friction in Rope Rescue," *Int. Tech. Rescue Symp.*, no. Itrs 99, pp. 1–16, 1999.
- [36] Unknown, "DuPont, Kapton: Summary of properties." DuPont, p. 19, 2017.
- [37] K. B. H. Klinkrad, P. Wegener, J. Bendisch, "Modeling of Collision Flux for the Current Space Debris Environment," in *Space debris: Models and Risk Analysis*, 2006, pp. 115–142.
- [38] C. Jenkins, *Gossamer spacecraft: membrane and inflatable structures technology for space applications*. Reston, VA: American Institute of Aeronautics and Astronautics, 2001.
- [39] H. Klinkrad, *Space Debris : Models and Risk Analysis*. 2006.
- [40] P. Anz-Meador and D. Shoots, "Monthly Number of Cataloged Objects in Earth Orbit by Object Type," *Orbital Debris Q. News*, vol. 21, no. 1, p. 12, 2016.
- [41] Unknown, "Home - Space Debris User Portal," *ESA - ESOC*. [Online]. Available: <https://sdup.esoc.esa.int/web/csdtf/home>. [Accessed: 13-Feb-2017].
- [42] M. Moser, C. Ranzenberger, and S. Duzellier, "Space Environmental Testing of Novel Candidate Materials for Multilayer Insulation," *J. Spacecr. Rockets*, vol. 53, no. 6, pp. 1134–1140, 2016.
- [43] Gunter Dirk Krebs, "EADS Astrium → Airbus Defence and Space: Eurostar-3000 - Gunter's Space Page," 2017. [Online]. Available: http://space.skyrocket.de/doc_sat/astrium_eurostar-3000.htm. [Accessed: 24-Jan-2018].
- [44] T. Konink and G. Kester, "SP-670 13th European Space Mechanisms & Tribology Symposium," 2009.
- [45] J. Bouwmeester, G. T. Aalbers, and W. J. Ubbels, "Preliminary mission results and project evaluation of the Delfi-C 3 nano-satellite," *Eur. Sp. Agency, (Special Publ. ESA SP*, no. 660 SP, 2008.
- [46] Unknown, "40mm Flat Round Air Bearing - New Way Air Bearings." [Online]. Available: <https://www.newwayairbearings.com/catalog/product/40mm-flat-round-air-bearings/>. [Accessed: 26-Jan-2018].
- [47] R. Verker, E. Grossman, N. Eliaz, I. Gouzman, S. Eliezer, M. Fraenkel, and S. Maman, *Ground simulation of hypervelocity space debris impacts 161*, vol. 6, no. c. 2006.
- [48] ASM, "ASM Material Data Sheet," *Matweb.com*. 2012.
- [49] "Dyneema® high-strength, high-modulus polyethylene fiber Fact sheet." pelicanrope, 2008.

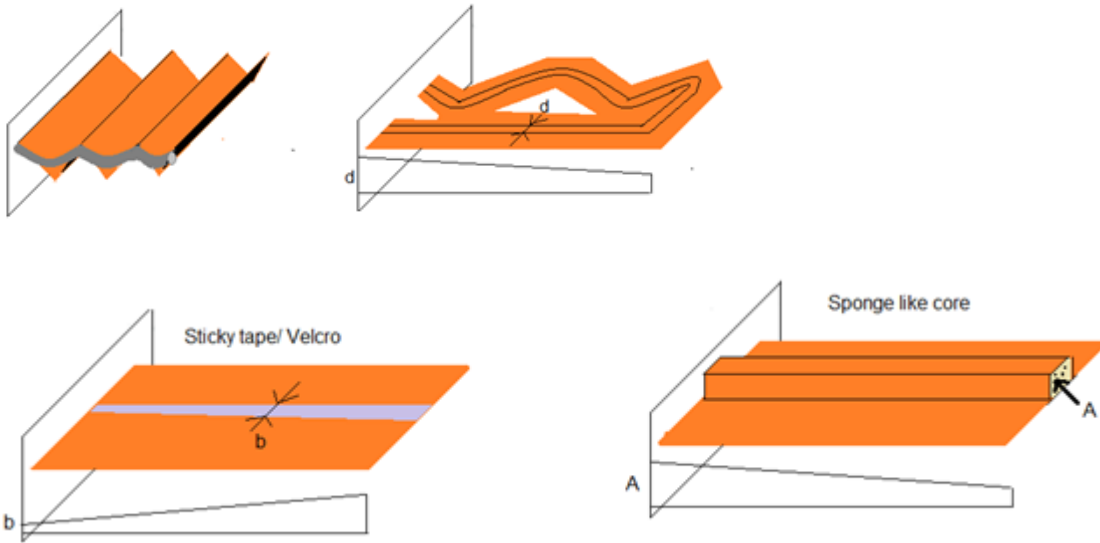
- [50] P. Mohazzabi and S. P. Shankar, "Damping of a Simple Pendulum Due to Drag on Its String," *J. Appl. Math. Phys.*, vol. 5, pp. 122–130, 2017.
- [51] P. A. A. Laura, J. L. Pombo, and E. A. Susemihl, "A note on the vibrations of a clamped-free beam with a mass at the free end," *J. Sound Vib.*, vol. 37, no. 2, pp. 161–168, 1974.

Appendix A: Inflated tube bending test results

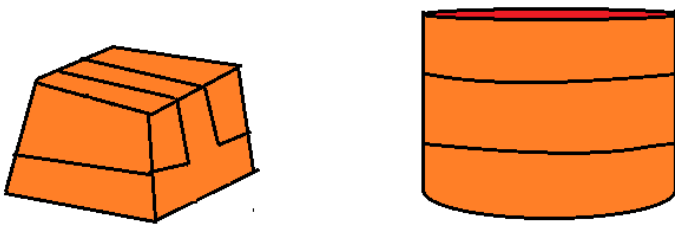


Appendix B: Strawman concepts

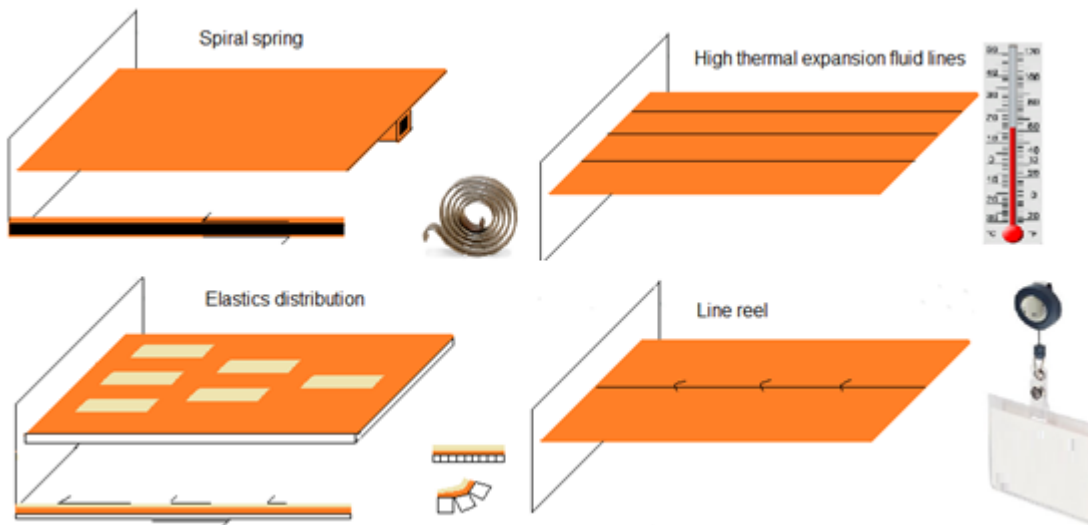
Single deployment concepts



Inflatable structures



Retractable concepts



Appendix C: Deployment concepts

The strawman concepts to provide support are shown in Figure 94. The concepts provide various degrees of freedom (DOF). The first mechanical deployment support however provides only a limited amount of freedom since the entanglement of the lines may influence the motion of the deployment. Furthermore, it is assumed that the stiffness of the FR is sufficient to perform the first deployment method.

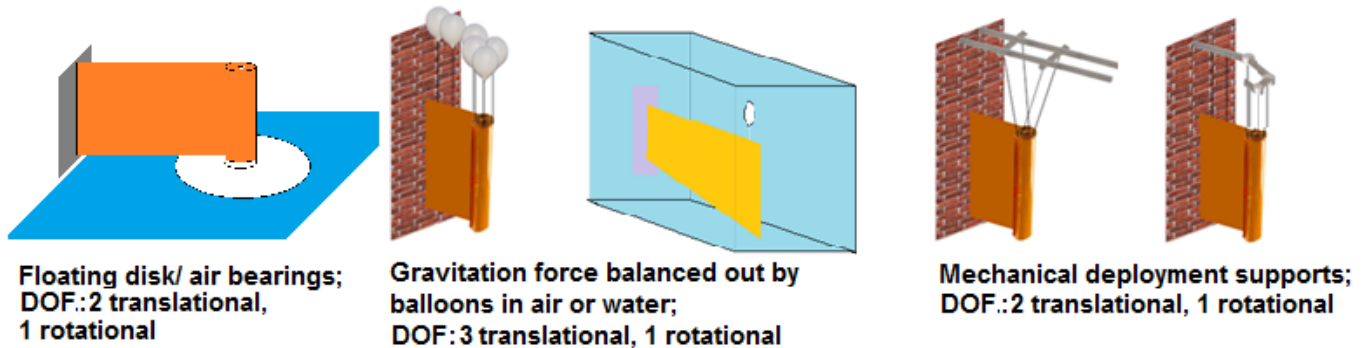
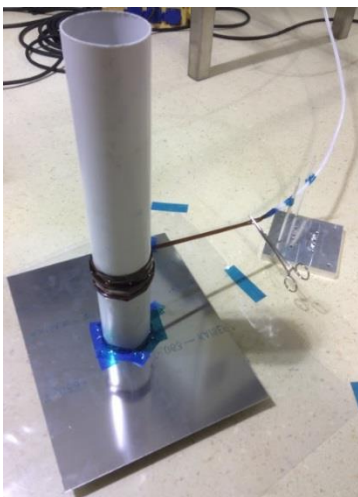


Figure 94: Deployment support options

Out of the deployment support options the first one is eventually chosen. The helium balloons would give the FR three degrees of freedom however the volume required at room temperature to lift a 1kg radiator would be:

$$V_{helium} = \frac{1}{\rho_{air} - \rho_{helium}} \frac{kg}{\frac{kg}{m^3}} = \frac{1}{(1,2 - 0,17)} = 0,97m^3$$

This would require a considerable number of balloons and the balloons may be difficult to balance the FR. Furthermore, the third degree of translational freedom (in z-direction) is not necessarily required. The water floatation concept is left out since it requires a large see-through reservoir and the water may damage the HiPeR laminate. The mechanical supports can be designed to support the deployment with one, two or three degrees of translational freedom. However, this would require a sophisticated design which does not fit within the scope of this project and the entanglement of the wires in the conventional deployment rig may influence the deployment. The floating disk provides two degrees of translational freedom and is relatively easy to manufacture, however the possibility of damaging the FR with water is reason to identify other options within this type of deployment. The options are considered to be either ball bearings that can be placed underneath the rotating disk, or air bearings. Breadboard tests show that the pressurized tubing is not capable of overcoming the friction of the ball bearings. Note that the platform is powered only by a single pressurized tube, this is however representative, as the total mass of the platform is half of the expected FR mass. The tube which is used in this situation is also the tube that is used in the actual FR. The acting deployment force shows to be lower than the friction of the bearings. The exact friction of the ball bearings was not the scientific objective of this test and is therefore not further investigated.



The alternative is to design a disk which experiences almost zero friction due to a layer of pressurized air between the platform and the floor. This is performed by air bearings, which is discussed further in the chapter tooling.

Appendix D: Design options

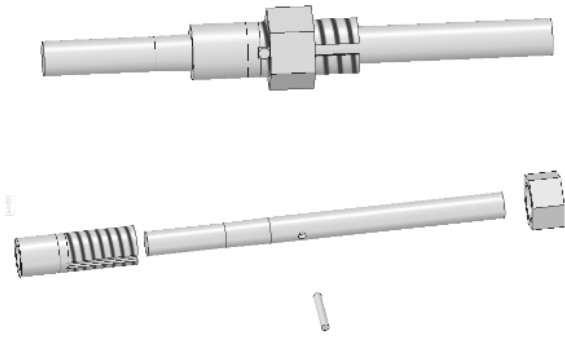


Figure 95: Connector design update: assembled (top) and parts (bottom)

The corner interface connects two straight connectors to make the flow bend around the 90 deg corner. The corner interface is made from a piece of aluminum and is used to provide structural support to the connectors but also allow fluid to flow through. The pipe which is part of the connector, can be screwed, glued or compressed into the corner interface. Tests are performed and the most appropriate fitting is found to be the H7 fitting with adhesive to seal the parts and to close openings. Another identified fitting is the compression fitting, however this fitting type damages the material and makes eventual repairs very difficult. The last option which is not tested however which seems possible, is to make the entire part including straight connectors from one piece of aluminum. However, this must be tested in a later stage. The corner connector design can be seen in Figure 49.

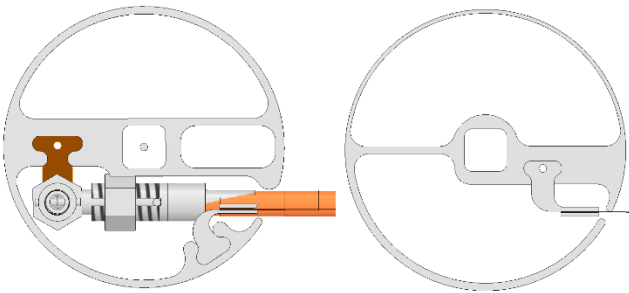


Figure 96: Roll support types: Tube roller (left) and foil roller (right)

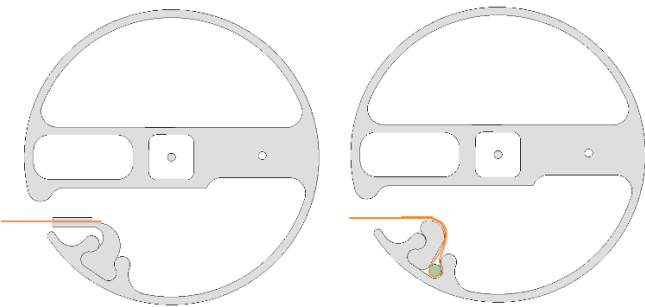


Figure 97: Foil attachment concepts

Appendix E: Thermal model nodes

FR tubing and FRRS nodes

1	5		
801	802	1004	
511	512	14	
521	522	34	
531	532	54	
541	542	74	
551	552	94	
561	562	114	
571	572	134	
581	582	154	
591	592	174	
601	602	194	8003
609	610	6100	8001
611	612		
621	622		
631	632		
641	642		
651	652		
661	662		
663	664	6640	8002
671	672	201	8004
681	682	181	
691	692	161	
701	702	141	
711	712	121	
721	722	101	
731	732	81	
741	742	61	
751	752	41	
761	762	21	
901	902	1011	
3	6		

Legend:

fluid
tube
connector
FRRS

Figure 98: Additional nodes

The FRRS conductive couplings are:

$$\frac{1}{GL_{610-6100}} = \frac{1}{\frac{k_{AL}A_{conn}}{0,005}} + \frac{1}{\frac{k_{Ves}A_{conn}}{0,011}} \Rightarrow GL_{610-6100} = 0,0036 \frac{W}{K}$$

$$\frac{1}{GL_{611-8001}} = \frac{1}{\frac{k_{AL}A_{cross}}{0,0165}} + \frac{1}{\frac{k_{Ves}A_{cross}}{0,0065}} \Rightarrow GL_{6100-8001} = 0,0088 \frac{W}{K}$$

The nodes which are selected for the center of the rollers are 8001 and 8002. These are connected to each other by means of the FRRS-bar which is made from Aluminum. The coupling between these nodes is straightforward and based on the distance between the two central rollers:

$$GL_{8001-8002} = \frac{k_{AL}A_{cross-bar}}{Dis_{rollers}} = 0,077 \frac{W}{K}$$

Node 8001 and 8002 are also considered for the average temperatures of the rollers. These nodes are hence also used for radiative and convective output of the FRRS. Node 8003 and 8004 are generated to simulate the outer rollers which are not directly connected to the tubing. Since the distance between the rollers on the outside is only half of the distance between 8001 and 8002, the coupling doubles.

$$GL_{8001-8003} = \frac{k_{AL}A_{cross-bar}}{\frac{Dis_{rollers}}{2}} = 0,15 \frac{W}{K}$$

Radiative couplings

The nodes are exposed to the environment which results in radiative couplings. The areas which are considered per node are found by using SpaceClaim. Only the areas which have a relevant view factor with Space are considered. The areas which are on the inside of the rollers are therefore not considered as well as the surfaces of the rollers which are close-by and facing each other. The areas which are considered are a combination of the roller and a part of the bar:

$$A_{exposed} = A_{roll-external} + A_{surf-bar}$$

For the central rollers (8001, 8002) the exposed area is:

$$A_{exposed-8001} = 0,014 m^2$$

For the outer rollers (8003, 8004):

$$A_{exposed-8003} = 0,0012m^2$$

The radiative couplings (taking into account an emissivity of untreated Aluminum of $\epsilon_{Alu} = 0,3$) are:

$$GR_{8001-9000} = 0,0043 \frac{W}{K}$$

$$GR_{8003-9000} = 0,0037 m^2$$

Convective couplings

The exposed areas also result in convective couplings with space during the tests. Since the air can easily flow through the rollers, this area is also considered for the convective couplings. For the analysis, the heat transfer is assumed to be $h_c = 5 \frac{W}{m^2K}$. The added areas sum up to:

$$A_{exposed-8001} = 0,025m^2$$

$$A_{exposed-8003} = 0,023m^2$$

The resulting convective couplings are:

$$GL_{8001-9000} = 0,13 \frac{W}{K}$$

$$GL_{8003-9000} = 0,12 \frac{W}{K}$$

The heat balance that occurs for different simulations within the FRRS nodes can be seen in the next table.

Table 47: Heat balance in the FRRS

Environment	Conductive (W)	(IN)	Radiative (W)	(OUT)	Convective (OUT) (W)	Balance (W)
Lab	0,07		0,01		0,06	0,0
Lab(+fans)	0,07		0,00		0,06	0,0
Vacuum	0,33		0,33		0,0	0,0
Space	0,48		0,48		0,0	0,0

The environment definitions were found earlier in Table 14.

First order verification

To make sure that the values which are found by the model are correct, a first order approximation is made with respect to the radiative and convective outputs. If we consider the full area of the FRRS, which adds up to $A_{FRRS-rad} = 0,053 m^2$ and for convective area we find $A_{FRRS-rad} = 0,096 m^2$. Then we should obtain the values which are found in with the following equations.

$$Q_{rad} = \varepsilon \sigma A_{tot} (T_{av-rollers}^4 - T_{env}^4)$$

$$Q_{conv} = h_{c-natural} A_{tot} (T_{av-rollers} - T_{env})$$

Table 48: First order estimated heat output FRRS

Environment	$T_{av-rollers}$ (°C)	Radiative heat total out (W)	Convective heat total out (W)
Lab	20,10	0,01	0,06
Lab(+fans)	20,03	0,0029	0,06
Vacuum	-68,46	0,33	0
Space	-121	0,48	0

Comparing the first order values with the values which were obtained from the model, the differences are very little (in the order of 10^{-3}) which verifies the outcome of the model.

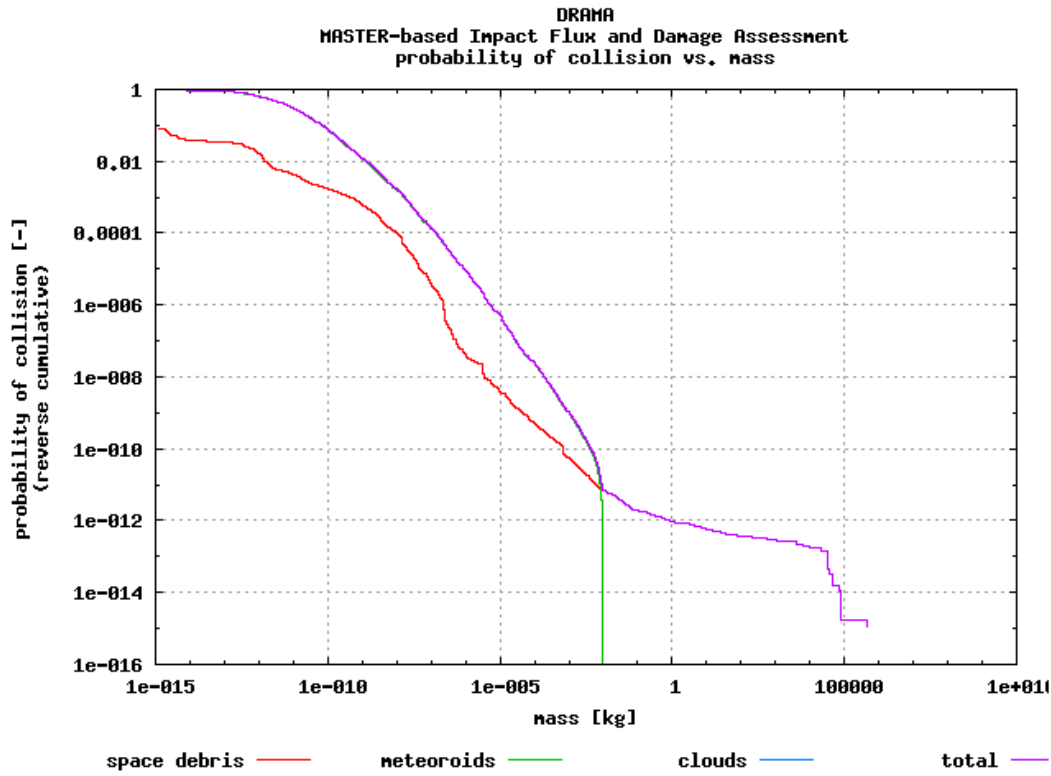
Table 49: Steady state temperatures in FRRS nodes

Environment	8003 (°C)	8001 (°C)	6100 (°C)	610 (°C)	664 (°C)	6640 (°C)	8002 (°C)	8004 (°C)
Lab	20,08	20,15	24,04	33,5	36,48	24,03	20,15	20,08
Lab(+fans)	20,01	20,05	23,77	32,83	32,78	23,75	20,05	20,01
Vacuum	-68,7	-67,22	-49,67	-4,46	-4,49	-49,68	-68,22	-68,70
Space	-121,3	-120,6	-93,3	-26,6	-26,6	-93,3	-120,6	-121,3

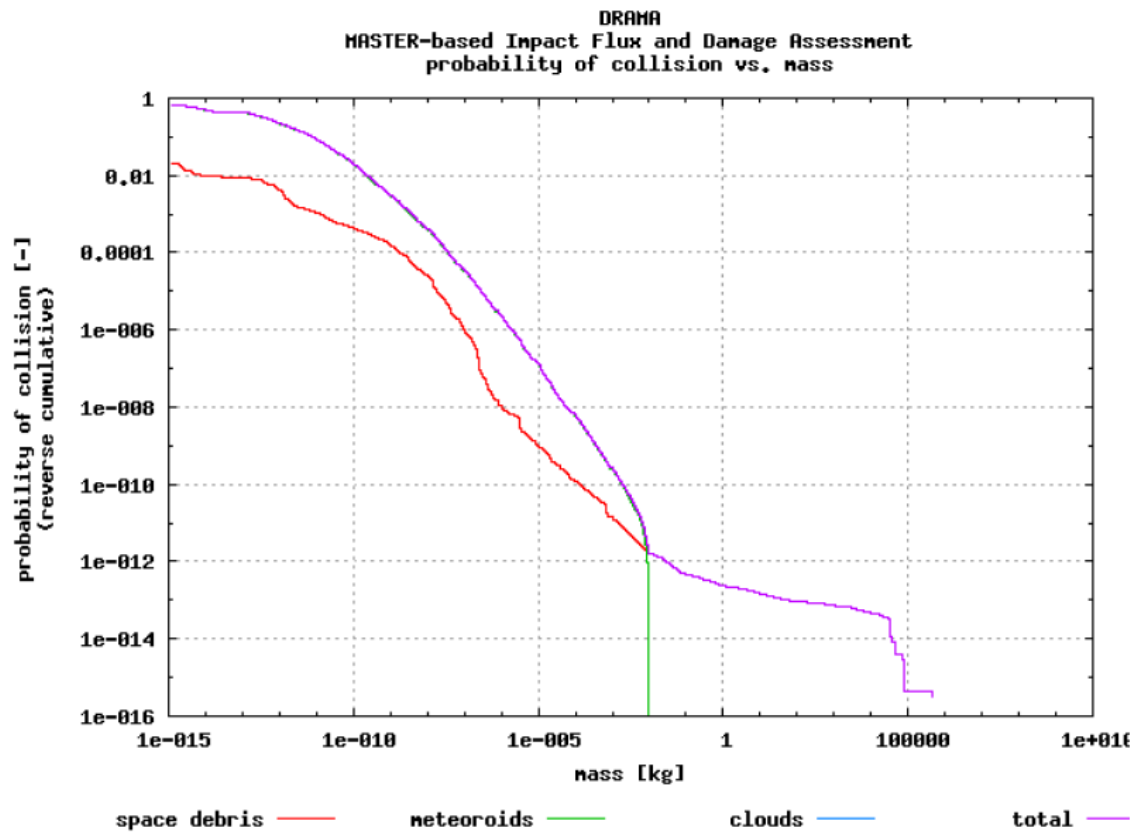
The results are that the FRRS does not dissipate much heat in any of the simulations as a result of the isolative parts. If we would compare the conductive heat that flows in, with the amount of radiated heat that the FR-foil dissipates (100-200W) it is only a small amount (>1%). Therefore, we can say that the FR-foil is well isolated from the FRRS.

Appendix F: DRAMA results

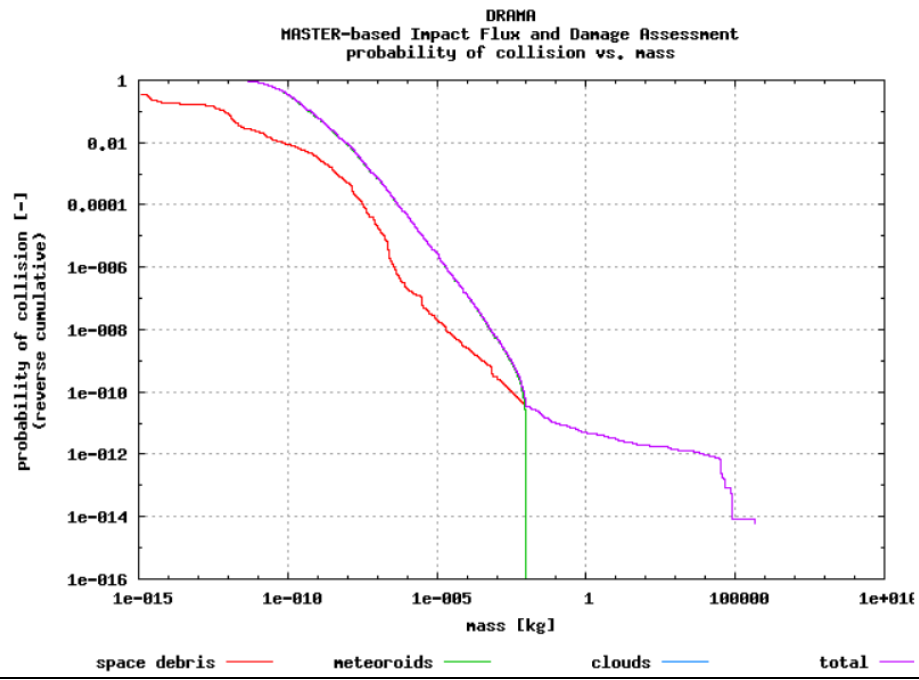
Spherical object, $A_{cross} = 0,05 \text{ m}^2$, 1 week in GEO:



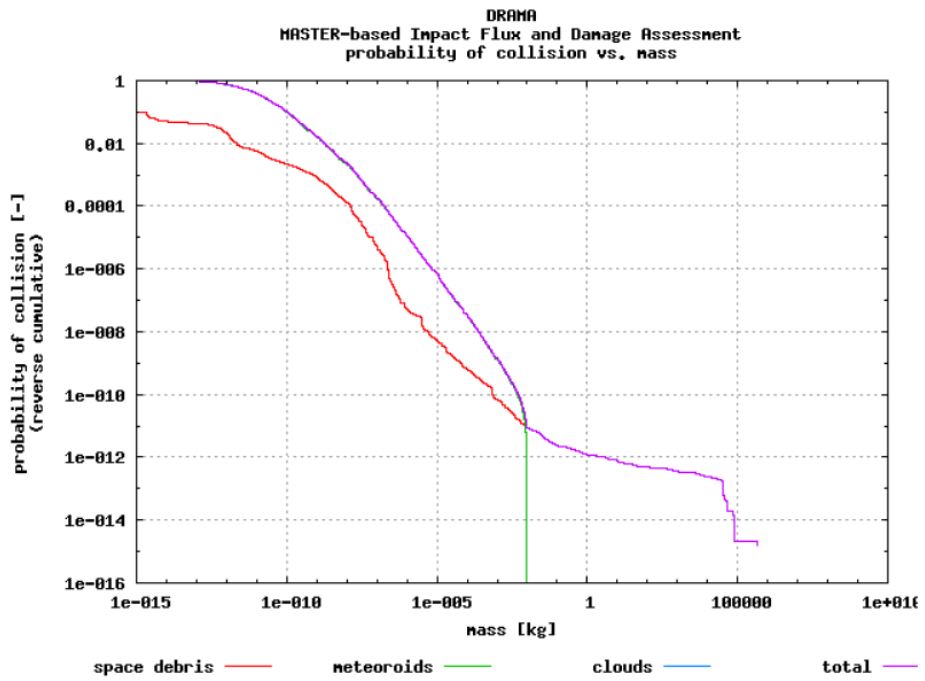
Randomly tumbling rectangular plat, $A_{cross} = 0,05 \text{ m}^2$, 1 week in GEO:



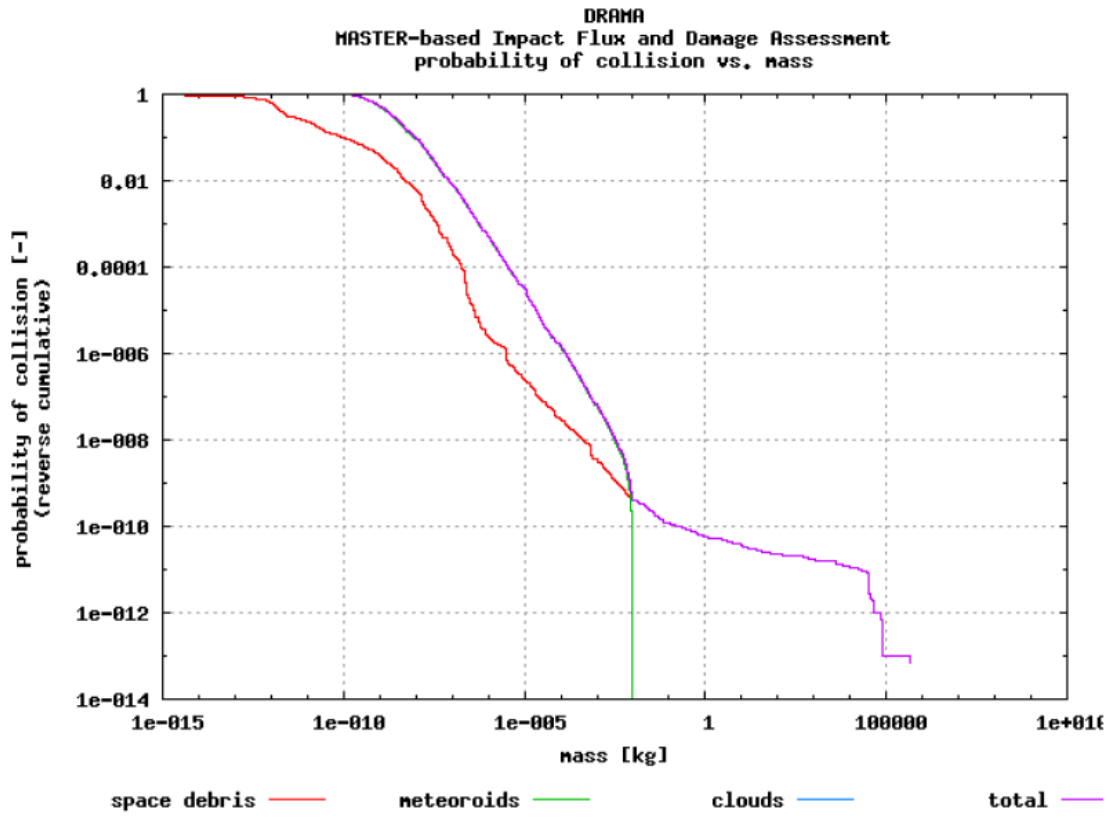
Spherical object, $A_{cross} = 0,05 \text{ m}^2$, 1 month in GEO:



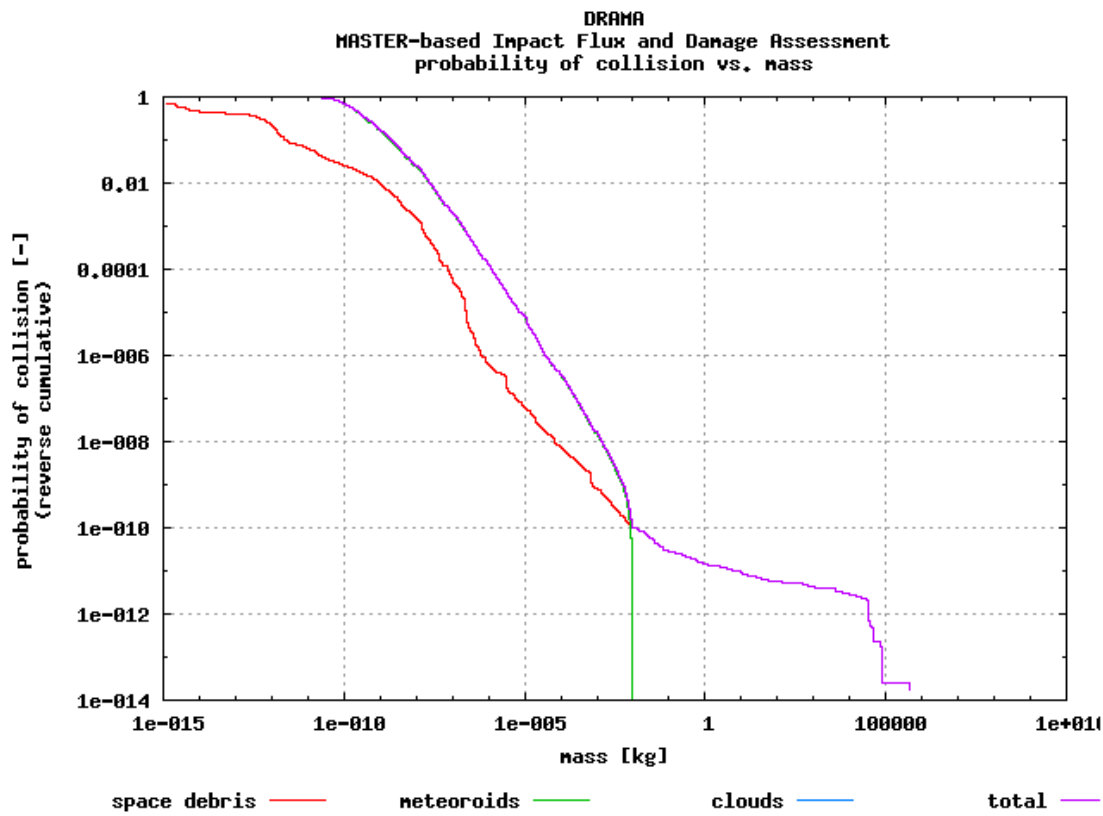
Randomly tumbling rectangular plate, $A_{cross} = 0,05 \text{ m}^2$, 1 month in GEO:



Sphere, $A_{cross} = 0,05 \text{ m}^2$, 1 year in GEO:

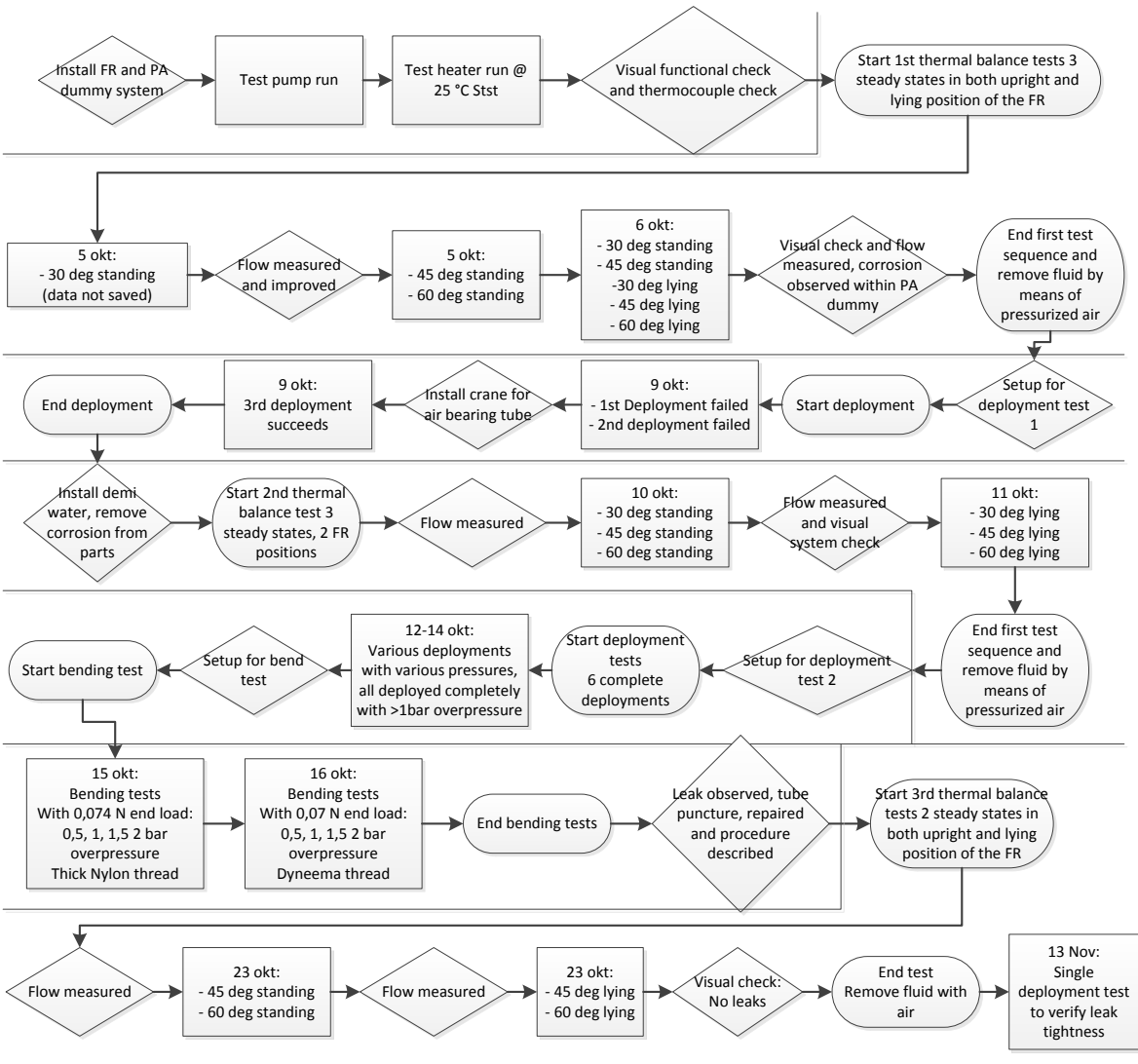


Randomly tumbling rectangular plate, $A_{cross} = 0,05 \text{ m}^2$, 1 year in GEO:

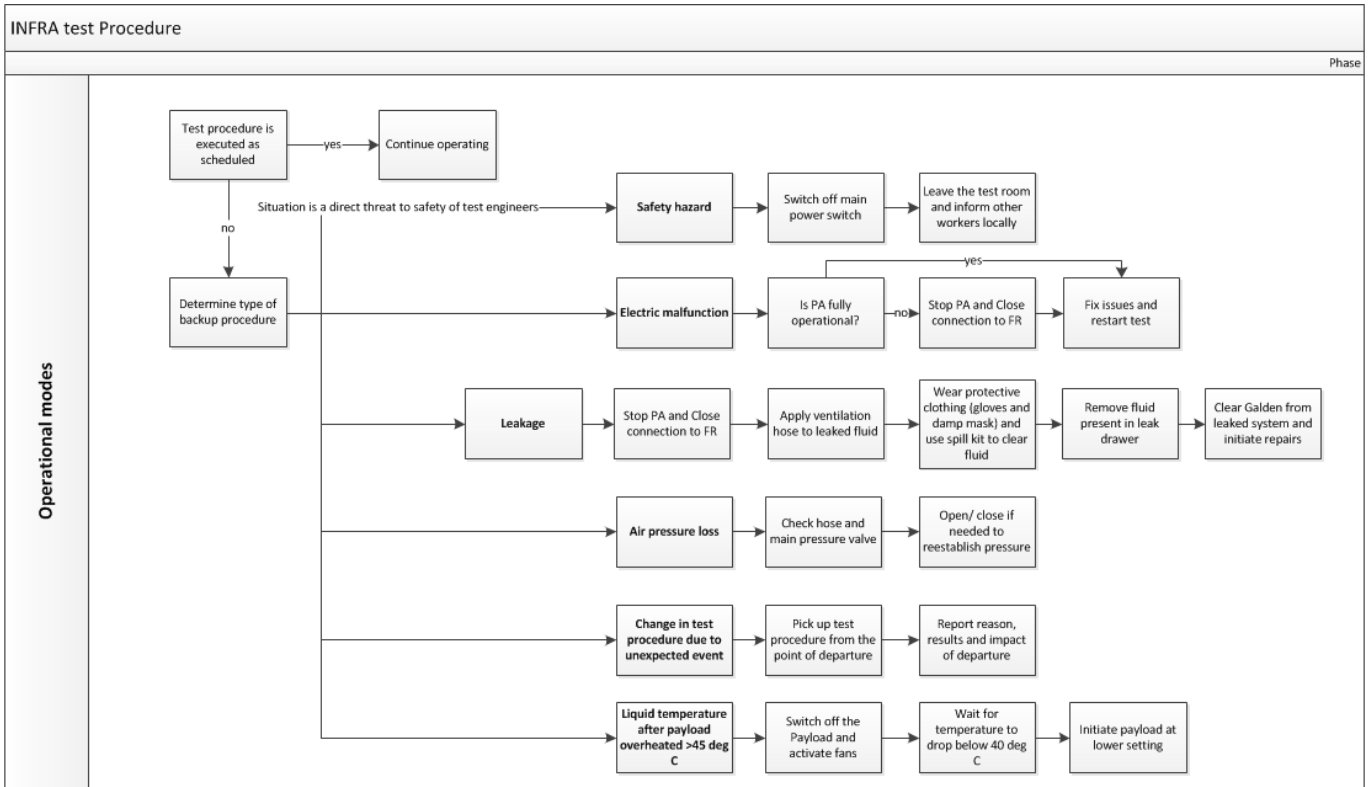
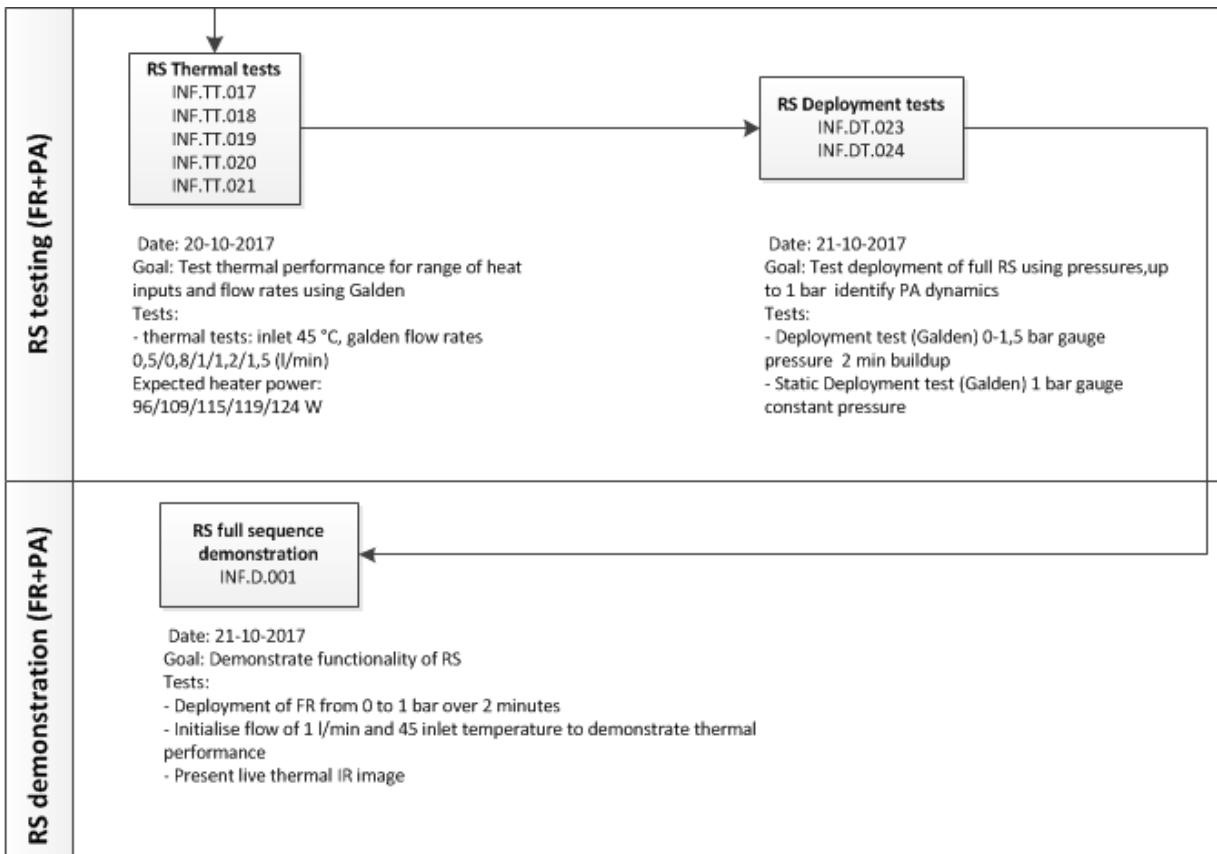


Appendix G: Test planning

FR test sequence



RS test sequence



Appendix H: FR thermal test data

FR thermal test data

Test # and position	Date (d,m)	Root (°C)	Tin (°C)	Tout (°C)	Mass flow (kg/s)	dT in-out (K)	Power diss (W)	dT (K)	Time (s)
Test 1 Stand	6-10	30	30,3	30	0,008 ± 0,001	0,3	10,0 ± 8,8	0,2	2000
Test 1 Lying	6-10	30	29,6	29,2	0,008 ± 0,001	0,4	13,4 ± 8,8	0,2	3000
Test 2 Stand	10-10	30	30,1	29,5	0,008 ± 0,001	0,6	20,1 ± 4,4	0,1	1000
Test 2 Lying	11-10	30	30,1	29,6	0,008 ± 0,001	0,5	16,7 ± 8,8	0,2	3000
Test 1a Stand	5-10	45	44,8	43,6	0,008 ± 0,001	1,2	40,1 ± 8,8	0,2	600
Test 1b Stand	6-10	45	44,4	43,5	0,008 ± 0,001	0,9	30,1 ± 8,8	0,2	200
Test 1 Lying	6-10	45	44,9	44,4	0,008 ± 0,001	0,5	16,7 ± 17,6	0,4	1000
Test 2 Stand	10-10	45	44,2	42,7	0,008 ± 0,001	1,5	50,2 ± 8,8	0,2	1500
Test 2 Lying	11-10	45	44,9	43,7	0,008 ± 0,001	1,2	40,1 ± 13,2	0,3	2000
Test 3 Stand	23-10	45	44,9	42,7	0,008 ± 0,001	2,2	73,6 ± 13,2	0,3	1500
Test 3 Lying	23-10	45	45,1	43,7	0,008 ± 0,001	1,4	46,8 ± 13,2	0,3	2000
Test 1 Stand	5-10	60	59,8	58,1	0,008 ± 0,001	1,7	56,9 ± 17,6	0,4	2000
Test 1 Lying	6-10	60	60,2	59,4	0,008 ± 0,001	0,8	26,8 ± 17,6	0,4	500
Test 2 Stand	10-10	60	60,1	57,8	0,008 ± 0,001	2,3	76,9 ± 17,6	0,4	1500
Test 2 Lying	11-10	60	60,3	58,6	0,008 ± 0,001	1,8	60,2 ± 22	0,5	2000
Test 3 Stand	23-10	60	59,8	56,4	0,008 ± 0,001	3,4	113,8 ± 17,6	0,4	2000
Test 3 Lying	23-10	60	59,8	57,3	0,008 ± 0,001	2,5	83,6 ± 17,6	0,4	2000

Appendix I: Sensitivity analysis, uncertainty parameters

Uncertainty parameters

Parameter	Uncertainty
Dimensions (m)	
- Thickness PGS	$\leq 10\%$
- Thickness Kapton	$\leq 10\%$
- Thickness adhesive	$\leq 10\%$
- Thickness tube (measured)	$\leq 10\%$
- Radius tube (measured)	$\leq 5\%$
- Tube interface contact coefficient	$\leq 12,5\%$
Temperatures ($^{\circ}C$)	
- Root (measured)	$\leq 2,5\%$
- Environment	$\leq 2,5\%$
Flow (water)	
- Volume flow (l/min) (measured)	$\leq 10\%$
- Conductivity (W/mK)	$\leq 5\%$
- Specific heat ($J/kg K$)	$\leq 1\%$
- Density (kg/m^3)	$\leq 1\%$
- Kinematic viscosity	$\leq 4\%$
- Tube length (m)	$\leq 67\%$
Optical	
- Emissivity FR (measured)	$\leq 2,5\%$
- Emissivity environment	$\leq 6\%$
Conductivity (W/mK)	
- PGS – in plane (from measurement data)	$\leq 3,6\%$
- PGS - out of plane	$\leq 15\%$
- Kapton	$\leq 50\%$
- Tube	$\leq 50\%$
- Adhesive	$\leq 56\%$
Natural convection	
- Heat transfer coefficient (W/m^2K)	$\leq 20\%$